Two spin liquid phases in the spatially anisotropic triangular Heisenberg model

Seiji Yunoki and Sandro Sorella

Istituto Nazionale di Fisica della Materia (INFM)-Democritos, National Simulation Centre, and Scuola Internazionale Superiore di Studi Avanzati (SISSA), I-34014 Trieste, Italy

The quantum spin-1/2 antiferromagnetic Heisenberg model on a two dimensional triangular lattice geometry with spatial anisotropy is relevant to describe materials such as Cs_2CuCl_4 and organic compounds such as κ-$(ET)_2Cu_2(CN)_3$. The strength of the spatial anisotropy can increase quantum fluctuations and can destabilize the magnetically ordered state leading to nonconventional spin liquid phases. In order to understand these intriguing phenomena, quantum Monte Carlo methods are used to study this model system as a function of the anisotropic strength, represented by the ratio J'/J between the intrachain nearest neighbor coupling J and the interchain one J'. We have found evidence of two spin liquid regions. The first one is stable for small values of the coupling $J'/J \lesssim 0.65$, and appears gapless and fractionalized, whereas the second one is a more conventional spin liquid with a small spin gap and is energetically favored in the region $0.65 \lesssim J'/J \lesssim 0.8$. We have also shown that in both spin liquid phases there is no evidence of broken translation symmetry with dimer or spin-Peirls order or any broken spatial reflection symmetry of the lattice. The various phases are in good agreement with the experimental findings, thus supporting the existence of spin liquid phases in two dimensional quantum spin-1/2 systems.

I. INTRODUCTION

Since the pioneering work by Anderson and Fazekas[1] the spin-1/2 antiferromagnetic Heisenberg model on the triangular lattice has been considered one of the most promising candidates for a spin liquid phase in a frustrated antiferromagnet. However, several numerical studies[2–5] have all consistently confirmed that in the isotropic triangular lattice the classical magnetically ordered state appears stable. Nevertheless the ordered moment is found considerably smaller than the classical value,[4,5] suggesting that the model is very close to a quantum critical point,[6] namely, to a phase where the long range antiferromagnetic order is completely destroyed. This picture is supported by the recently established result that in the quantum dimer model on the triangular lattice geometry[7] a spin liquid phase is stable, a result that is particularly important because for instance the same model on the square lattice displays only non-spin-liquid phases with broken translation symmetry.[8–10]

Recent experiments on two different materials[11,12] have renewed the interest in the spin-1/2 antiferromagnetic Heisenberg model on the triangular lattice described by the following Hamiltonian:[13]

$$\hat{H} = J \sum_{\langle \mathbf{i},\mathbf{j} \rangle} \vec{S}_\mathbf{i} \cdot \vec{S}_\mathbf{j} + J' \sum_{\langle\langle \mathbf{i},\mathbf{j} \rangle\rangle} \vec{S}_\mathbf{i} \cdot \vec{S}_\mathbf{j}, \qquad (1)$$

where $\vec{S}_\mathbf{i}$ is a spin 1/2 located at site $\mathbf{i}$ on the triangular lattice, $\langle \mathbf{i},\mathbf{j} \rangle$ ($\langle\langle \mathbf{i},\mathbf{j} \rangle\rangle$) indicates nearest neighbor sites along the chain (between different chains), and the corresponding antiferromagnetic couplings are denoted by J and J' (see Fig. 1).

Clearly the anisotropy increases the quantum fluctuations in this model as for $J'=0$ the Hamiltonian $\hat{H}$ reduces to a system of uncoupled one dimensional (1D) chains, implying spin fractionalization and no antiferromagnetic order. In this limit the spin one excitations should form a broad two-spinon continuum of states as predicted theoretically,[14] and indeed several experiments by inelastic neutron scattering have revealed this non-trivial-spin dynamics.[15]

In a series of experiments by Coldea *et al.*,[11] the low energy spin dynamics of Cs_2CuCl_4 have been studied systematically and found to be described essentially by the model Hamiltonian (1) with anisotropic exchange interaction $J/J' \simeq 3.0$. In their experiments,[11] there are two facts supporting the existence of a two-dimensional (2D) spin liquid phase in this system: (i) a spin spiral phase appears at temperatures below $T_N \simeq 0.6$ K, which is about the same order of magnitude as the interplane coupling $J''/J \simeq 0.045$ in the third spatial direction, and therefore sizably smaller than the 2D couplings J ($\simeq 0.37$ meV) and J'. In fact, true long range order in 2D is possible only at zero temperature and a finite T_N is due to the inter plane coupling J'' which allows one to cutoff the logarithmically divergent quantum fluctuations in 2D. A finite T_N is therefore expected to be of order $\simeq J'/\ln(J'/J'')$, which appears rather close to the observed $T_N \simeq 0.6$ K. (ii) At temperatures larger than T_N (or by applying an external magnetic field), the inelastic neutron scattering experiments[11] found that the line shape of the spectrum consists of a broad continuum, which is in contrast to the expected behavior of a magnetically ordered state, but is instead similar to the broad two-spinon continuum expected in the 1D systems mentioned above. Therefore these experiments suggest that spin fractionalization can be realized also in this 2D system for temperatures higher than the corresponding three-dimensional (3D) transition temperature T_N.

Another spectacular experiments on spin-1/2 quasi-2D triangular systems have been recently reported by Shimizu *et al.*[12] Here two organic materials κ-$(ET)_2Cu_2(CN)_3$ and κ-$(ET)_2Cu_2[N(CN)_2]Cl$ [where ET denotes bis(ethylenedithio)-tetrathiafulvalene] are synthesized, corresponding essentially to two different values of $J'/J \simeq 0.8$–0.9 and $J'/J \simeq 1.8$, respectively.[12] While the latter
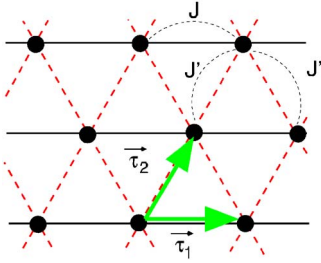
FIG. 1. (Color online) Antiferromagnetic Heisenberg models on the triangular lattice studied. A spin-1/2 is located at each dot. $\vec{\tau}_1$ $=(1,0)$ and $\vec{\tau}_2=\left(\frac{1}{2},\frac{\sqrt{3}}{2}\right)$ denote the primitive translational vectors. A lattice constant is set to be 1.

material shows commensurate spin ordering at $T_N = 27$ K, for the former material no magnetic order is observed even down to the milli-Kelvin region (~ 32 mK) regardless the fact that the estimated value of J is about 250 K. This observation strongly indicates possible realization of a spin liquid state for κ-(ET)$_2$Cu$_2$(CN)$_3$.[12]

Motivated by these experiments, we shall consider here the spin-1/2 antiferromagnetic Heisenberg model on the triangular lattice with spatial anisotropy described by Eq. (1). In particular, we report a detailed and systematic quantum Monte Carlo (QMC) study of the ground state as well as the low-lying excitations of this model system as a function of J'/J. Using both quantum variational Monte Carlo (VMC) method and Green function Monte Carlo method with an improved extension of the fixed node approximation (named effective Hamiltonian approach in this paper), it is found that there exist two spin liquid regions in the phase diagram of this model by varying the ratio J'/J for $J'/J \lesssim 0.8$. The first one is stable for small values of the coupling $J'/J \lesssim 0.65$, and appears to show gapless, fractionalized fermionic excitations. The second one is energetically favored in the region $0.65 \lesssim J'/J \lesssim 0.8$, and is a more conventional spin liquid with a small spin gap in the excitation spectrum, the same type of spin liquid phase realized in the quantum dimer model in the isotropic triangular geometry.[7] It is argued that the two experimental observations of spin-liquid-like behaviors for Cs$_2$CuCl$_4$ and κ-(ET)$_2$Cu$_2$(CN)$_3$ mentioned above should correspond to these two different spin liquid phases of the model, respectively.

The paper is organized as follows. In Sec. II, we first introduce the variational wave functions considered (Sec. II A), and describe our original optimization method to obtain the minimum energy variational wave function containing a large number of variational parameters (Sec. II B). In order to systematically correct this variational ansatz, an effective Hamiltonian approach is introduced in Sec. II C along the line of the well established diffusion Monte Carlo technique,[16] allowing, for continuous systems, to achieve the best variational wave function with the same phases of the chosen variational state. As explained in Sec. II D, within this approach, it is also possible to calculate the low-lying excitation spectrum, which can be compared directly with dynamical experimental measurements. In Sec. III, all our numerical results are reported for the spin-1/2 antiferromagnetic Heisenberg model on the triangular lattice as a function

of J'/J, including the decoupled chains case ($J'=0$). Finally our conclusions and remarks are presented in Sec. IV. The paper is also supplemented by several important appendixes for the detailed explanation of the methods and the wave functions used, which should be very useful for reproducing our results or extending our approach to other model systems. A part of this work have been reported briefly as a short communication.[17]

II. NUMERICAL METHOD

A. Variational wave functions: Projected BCS states

The variational wave function considered in this study is the so-called projected BCS state defined by

$$|p\text{-BCS}\rangle = \mathcal{P}_G \exp\left[\sum_{i<j} f_{i,j}(c^\dagger_{i,\uparrow}c^\dagger_{j,\downarrow} + c^\dagger_{j,\uparrow}c^\dagger_{i,\downarrow})\right]|0\rangle, \quad (2)$$

where $c^\dagger_{i,\sigma}$ ($c_{i,\sigma}$) is an electron creation (annihilation) operator at site i with spin $\sigma(=\uparrow,\downarrow)$, $|0\rangle$ is the vacuum state with no electrons, the function $f_{i,j}$ is the so-called pairing function that contains all variational freedom of the $|p\text{-BCS}\rangle$, and is determined by the minimum energy condition, whereas $\mathcal{P}_G$ is the usual Gutzwiller projection operator onto the subspace of singly occupied sites, implying that the total number of electrons N is equal to the number of sites L. The pairing function $f_{i,j}$ of this projected BCS state can be parametrized using a BCS Hamiltonian

$$\hat{H}_{BCS} = \sum_{i,j}\left[t_{i,j}\left(\sum_\sigma c^\dagger_{i,\sigma}c_{j,\sigma}\right) + (\Delta_{i,j}c^\dagger_{i,\uparrow}c^\dagger_{j,\downarrow} + \text{H.c.})\right]. \quad (3)$$

Here $t_{i,j}$ and $\Delta_{i,j}$ as well as the chemical potential $t_{i,i}=-\mu$ (assumed uniform) can be considered variational parameters, which implicitly determine the pairing function $f_{i,j}$ corresponding to the ground state (GS) of $\hat{H}_{BCS}$. Here i,j ($=1,2,\ldots,L$) label the sites of the lattice (see Fig. 1), i.e., $\vec{r}_i=i_1\vec{\tau}_1+i_2\vec{\tau}_2$, in the lexicographic order, so that the condition $i<j$ in Eq. (2) is meaningful in any spatial dimension.

When $t_{i,j}$ and $\Delta_{i,j}$ depend only on $\vec{l}=\vec{r}_i-\vec{r}_j$, i.e., $t_{i,j}=t_{\vec{l}}$ and $\Delta_{i,j}=\Delta_{\vec{l}}$, respectively, $\hat{H}_{BCS}$ can be described more compactly by

$$\hat{H}_{BCS} = \sum_{\mathbf{k},\sigma}(\varepsilon_\mathbf{k} - \mu)c^\dagger_{\mathbf{k},\sigma}c_{\mathbf{k},\sigma} + \sum_\mathbf{k}(\Delta_\mathbf{k}c^\dagger_{\mathbf{k},\uparrow}c^\dagger_{-\mathbf{k},\downarrow} + \text{H.c}). \quad (4)$$

Here

$$c^\dagger_{\mathbf{k},\sigma} = \frac{1}{\sqrt{L}}\sum_j e^{-i\vec{k}\cdot\vec{r}_j}c^\dagger_{j,\sigma}, \quad (5)$$

$$\varepsilon_\mathbf{k} = \sum_{\vec{l}} e^{-i\vec{k}\cdot\vec{l}}t_{\vec{l}}, \quad (6)$$

and

$$\Delta_\mathbf{k} = \sum_{\vec{l}} e^{-i\vec{k}\cdot\vec{l}}\Delta_{\vec{l}}. \quad (7)$$

For a singlet pairing, $\Delta_{i,j}=\Delta_{j,i}$, and thus $\Delta_\mathbf{k}=\Delta_{-\mathbf{k}}$. In this case the projected BCS wave function defined by Eq. (2) reads

TABLE I. Optimized variational parameters of the wave function $|p\text{-BCS}\rangle$ for the spin-1/2 antiferromagnetic Heisenberg model on the anisotropic triangular lattice [Eq. (1)] with various J'/J and $L = 18 \times 18$. $\Delta_{(n,m)}$ is the gap function $\Delta_{\vec{r}}$ for $\vec{r} = n\vec{\tau}_1 + m\vec{\tau}_2$. All other variational parameters are zero except for the chemical potential μ and the nearest neighbor hopping in the $\vec{\tau}_1$ direction, which is chosen to be 1. The value of K, variational energy $E_{\text{VMC}} = E(p\text{-BCS})$, FN (FNE) ground state energy $E_{\text{FN}} = E_0^{\text{FN}}$ ($E_{\text{FNE}} = E_0^{\text{eff}}$) with $|\psi_G\rangle = |p\text{-BCS}\rangle$ are also presented. The number in parentheses is the statistical error bar of the quantity corresponding to the last digit of the figure.

J'/J	0.1	0.2	0.33	0.4	0.5	0.6	0.7
μ	$-0.066(4)$	$-0.085(5)$	$-0.109(4)$	$-0.147(4)$	$-0.200(4)$	$-0.232(4)$	$-0.253(3)$
$\Delta_{(1,0)}$	2.28(2)	2.02(2)	1.74(2)	1.61(3)	1.48(3)	1.36(2)	1.24(3)
$\Delta_{(0,1)}$	0.545(7)	0.617(6)	0.627(6)	0.644(8)	0.689(8)	0.739(7)	0.787(7)
$\Delta_{(1,1)}$	0.155(4)	0.179(3)	0.192(3)	0.214(4)	0.256(4)	0.293(3)	0.329(4)
$\Delta_{(-1,2)}$	0.007(5)	0.099(6)	0.147(6)	0.160(6)	0.162(8)	0.153(4)	0.143(6)
$\Delta_{(2,0)}$	$-0.010(1)$	$-0.006(2)$	$-0.0012(8)$	0.002(2)	0.013(1)	0.025(2)	0.037(2)
$\Delta_{(0,2)}$	0.195(3)	0.159(5)	0.070(3)	0.058(4)	0.062(4)	0.068(5)	0.066(4)
$\Delta_{(2,1)}$	0.346(4)	0.381(4)	0.370(4)	0.363(5)	0.360(5)	0.361(6)	0.356(6)
$\Delta_{(1,2)}$	0.041(2)	0.085(3)	0.098(3)	0.102(4)	0.102(5)	0.097(6)	0.095(4)
$\Delta_{(-2,3)}$	0.052(1)	0.040(1)	0.006(2)	0.006(2)	0.010(2)	0.013(2)	0.015(1)
$\Delta_{(3,0)}$	0.491(5)	0.434(4)	0.383(4)	0.363(5)	0.345(5)	0.327(6)	0.304(6)
K^{-1}	1.00243(3)	1.01014(7)	1.0286(2)	1.0434(2)	1.0700(3)	1.1030(3)	1.1425(3)
E_{VMC}/JL	$-0.44590(1)$	$-0.44687(1)$	$-0.44929(2)$	$-0.45118(2)$	$-0.45474(2)$	$-0.45932(2)$	$-0.46514(2)$
E_{FN}/JL	$-0.446074(1)$	$-0.44723(1)$	$-0.45005(1)$	$-0.45223(1)$	$-0.45628(1)$	$-0.46156(1)$	$-0.46823(1)$
E_{FNE}/JL	$-0.446075(1)$	$-0.447233(2)$	$-0.45007(1)$	$-0.45229(1)$	$-0.45642(1)$	$-0.46183(1)$	$-0.46875(1)$

$$|p\text{-BCS}\rangle = \mathcal{P}_G|\text{BCS}\rangle, \qquad (8)$$

with $|\text{BCS}\rangle$ being the ground state of $\hat{H}_{\text{BCS}}$ given by Eq. (4):

$$|\text{BCS}\rangle = \exp\left[\sum_{\mathbf{k}} f_{\mathbf{k}} c_{\mathbf{k},\uparrow}^\dagger c_{\mathbf{k},\downarrow}^\dagger\right]|0\rangle, \qquad (9)$$

where $f_{\mathbf{k}} = v_{\mathbf{k}}/u_{\mathbf{k}} = \Delta_{\mathbf{k}}/(\xi_{\mathbf{k}} + E_{\mathbf{k}})$, $u_{\mathbf{k}} = \sqrt{\frac{1}{2}\left[1 + \frac{\xi_{\mathbf{k}}}{E_{\mathbf{k}}}\right]}$, and

$$E_{\mathbf{k}} = \sqrt{\xi_{\mathbf{k}}^2 + \Delta_{\mathbf{k}}^2} \qquad (10)$$

with $\xi_{\mathbf{k}} = \varepsilon_{\mathbf{k}} - \mu$.

At the variational level, both $\xi_{\mathbf{k}}$ and $\Delta_{\mathbf{k}}$ have to be parametrized in order to minimize the variational energy of the $|p\text{-BCS}\rangle$ wave function. The most relevant parameters for lowering the energy are the short range terms, and we have chosen to expand $\varepsilon_{\vec{k}} = \sum_{\nu=1}^3 2t_{\vec{\tau}_\nu} \cos(\vec{k} \cdot \vec{\tau}_\nu)$, where $t_{\vec{\tau}_\nu}$ are variational parameters and $\vec{\tau}_\nu$ are the nearest neighbor vectors ($\vec{\tau}_3 = \vec{\tau}_2 - \vec{\tau}_1$). Analogously, the gap function $\Delta_{\vec{r}}$ is truncated up to the third nearest distance along the chain ($\vec{\tau}_1$) direction. This is also because, as will be discussed in Sec. III B, for the 1D spin-1/2 antiferromagnetic Heisenberg model $\hat{H}_{\text{1D}}$, inclusion of the parameter $\Delta_{3\vec{\tau}_1}$ is known to be crucial for this type of projected BCS states to represent almost exactly the ground state of $\hat{H}_{\text{1D}}$.[18] For the present 2D system described by Eq. (1), which preserve C_{2v} symmetry for $J' \neq J$, the projected BCS state $|p\text{-BCS}\rangle$ thus contains ten independent variational parameters in $\Delta_{\mathbf{k}}$ (see, e.g., Table I) and the chemical potential μ which, as opposed to the 1D case, may differ from zero in the triangular lattice case. As will be

discussed in Sec. III C, we found that the variational parameters $t_{\vec{\tau}_2}$ and $t_{\vec{\tau}_3}$ are irrelevant and the energetically favorable symmetry of $\Delta_{\mathbf{k}}$ is A_1.[17]

As shown in Sec. III, the projected BCS state described above is a very good variational state for $J'/J \lesssim 0.65$–0.7. However, close to the isotropic limit $J'/J \simeq 1.0$, the translation invariant ansatz state, also previously attempted in the presence of hole doping,[19,20] is not very accurate when compared with the exact diagonalization results possible on the 6×6 cluster.[21] In this region of J'/J, as shown in Sec. III D, we have found that it is more convenient to consider a BCS Hamiltonian defined on a (2×1) unit cell [see Eq. (55)] for a much better variational wave function. As shown in Appendix C, by using the projected BCS state thereby constructed, it is then possible to represent the well known short range resonant valence bond (RVB) wave function, with a particular choice of the variational parameters. The RVB state is a good variational ansatz for the isotropic triangular lattice[3] and represents a very convenient initial guess for defining, within the present $|p\text{-BCS}\rangle$ framework, an accurate variational state in the nearly isotropic triangular lattice.

B. Minimization method

In order to evaluate the optimal variational parameters that minimize the energy expectation value

$$E(\Psi) = \frac{\langle\Psi|H|\Psi\rangle}{\langle\Psi|\Psi\rangle}, \qquad (11)$$

we follow the method, recently introduced for calculations of electronic structure,[22] which will be described in some detail

in the following. According to this method, in order to reach the minimum energy $E(\Psi)$ in a stable and efficient way, the logarithmic derivative $O_k(x)$ of the wave function $\Psi_{\{\alpha_k\}}(x)$ $= \langle x | \Psi_{\{\alpha_k\}} \rangle$ with respect to each variational parameter α_k $= t_{i,j}$ and/or $\Delta_{i,j}$ $(k=1,2,\ldots,p)$ has to be evaluated on a given N-electron configuration $x=\{\mathbf{r}_1,\ldots,\mathbf{r}_N\}$, namely,

$$O_k(x) = \frac{\partial}{\partial \alpha_k} \ln \Psi_{\{\alpha_k\}}(x). \tag{12}$$

In fact, for infinitesimal changes of these variational parameters, $\alpha_k \rightarrow \alpha'_k = \alpha_k + \delta\alpha_k$, the corresponding change of the wave function reads

$$\Psi_{\{\alpha'_k\}}(x) = \Psi_{\{\alpha_k\}}(x) \left[1 + \sum_{k=1}^{p} O_k(x) \cdot \delta\alpha_k + O(\delta\alpha_k^2) \right]. \tag{13}$$

In order to simplify the notations, here we introduce the operator $\hat{O}_k$ corresponding to $O_k(x)$ which is defined by

$$\langle x | \hat{O}_k | x' \rangle = O_k(x) \cdot \delta_{xx'}. \tag{14}$$

Using this operator form, the above equation is more compactly written as

$$|\Psi_{\{\alpha'_k\}}\rangle = \left[1 + \sum_{k=1}^{p} \delta\alpha_k \hat{O}_k \right] |\Psi_{\{\alpha_k\}}\rangle \tag{15}$$

valid up to $O(\delta\alpha_k^2)$.

For the minimization method described below, it is important to evaluate numerically the value $O_k(x)$ corresponding to a given real space configuration of electrons x satisfying the constraint of no doubly occupied sites. To this purpose, we have to recall that the variational parameters $\Delta_{i,j}$ and $t_{i,j}$ are explicitly defined in $\hat{H}_{\mathrm{BCS}}$ [Eq. (3)], but only implicitly in the wave function itself, defined as the ground state of this unprojected BCS Hamiltonian $|\mathrm{BCS}\rangle$ [Eq. (2)]. Thus, in order to evaluate the logarithmic derivatives of the wave function $|\Psi_{\{\alpha_k\}}\rangle$ with respect to a variational parameter α_k, we apply simple perturbation theory to $\hat{H}_{\mathrm{BCS}}$ and calculate the perturbed state $|\Psi_{\{\alpha_k+\delta\alpha_k\}}\rangle$, within linear order in $\delta\alpha_k$. It is then possible to compute $\langle x | \Psi_{\{\alpha_k+\delta\alpha_k\}}\rangle$ using simple algebra and within the same accuracy $O(\delta\alpha_k^2)$. After recasting the calculation by using appropriate matrix-matrix operations, the evaluation of $O_k(x)$ is possible in an efficient way, using only $\simeq (2L)^2$ operations for each variational parameter α_k. More details of the method are found in Appendix A.

The minimization method used here is similar to the standard and well known steepest descent method, where the expectation value of the energy $E(\Psi_{\{\alpha_k\}})$ is optimized by iteratively changing the parameters α_k $(k=1,\ldots,p)$ according to the corresponding derivatives of the energy (generalized forces):

$$f_k = -\frac{\partial E(\Psi_{\{\alpha_k\}})}{\partial \alpha_k} = -\frac{\langle \Psi_{\{\alpha_k\}} | [\hat{O}_k \hat{H} + \hat{H} \hat{O}_k] | \Psi_{\{\alpha_k\}} \rangle}{\langle \Psi_{\{\alpha_k\}} | \Psi_{\{\alpha_k\}} \rangle}$$

$$+ 2E(\Psi_{\{\alpha_k\}}) \frac{\langle \Psi_{\{\alpha_k\}} | \hat{O}_k | \Psi_{\{\alpha_k\}} \rangle}{\langle \Psi_{\{\alpha_k\}} | \Psi_{\{\alpha_k\}} \rangle}, \tag{16}$$

namely,

$$\alpha_k \rightarrow \alpha'_k = \alpha_k + f_k \cdot \delta t, \tag{17}$$

where δt in the standard steepest descent method is determined at each iteration by minimizing the energy expectation value.[23] The above expressions for the forces f_k can be computed statistically by appropriately averaging the local energy

$$e_L(x) = \frac{\langle \Psi_{\{\alpha_k\}} | \hat{H} | x \rangle}{\langle \Psi_{\{\alpha_k\}} | x \rangle}$$

and $O_k(x)$ over a set of configurations $\{x_l\}$, $l=1,2,\ldots,M$ distributed according to the square of the wave function $|\langle x | \Psi_{\{\alpha_k\}} \rangle|^2$, generated with a standard variational Monte Carlo (VMC) scheme, namely,

$$f_k = -\frac{2}{M} \sum_{l=1}^{M} O_k(x_l) e_L(x_l) + 2\bar{O}_k \bar{e}_L, \tag{18}$$

$$\bar{O}_k = \frac{1}{M} \sum_{l=1}^{M} O_k(x_l), \tag{19}$$

$$\bar{e}_L = \frac{1}{M} \sum_{l=1}^{M} e_L(x_l) \tag{20}$$

and thus f_k can be computed efficiently once $O_k(x)$ and $e_L(x)$ are evaluated for any sampled configuration. Here we assumed that all quantities are real. However an extension to the complex case is straightforward.

Now, for simplicity, we assume that δt is positive and small enough. Indeed the variation of the total energy

$$\Delta E = E(\Psi_{\{\alpha'_k\}}) - E(\Psi_{\{\alpha_k\}}) = -\sum_{k=1}^{p} f_k \cdot \delta\alpha_k + \mathcal{O}(\delta\alpha_k^2) \tag{21}$$

at each step is easily shown to be negative for small enough δt because in this limit

$$\Delta E = -\delta t \sum_{k=1}^{p} f_k^2 + \mathcal{O}(\delta t^2). \tag{22}$$

Thus the steepest descent method certainly converges to the minimum of the energy when all the forces vanish.

Let us now generalize the steepest descent method by slightly modifying the basic iteration (17) with a suitably chosen positive definite matrix $\bar{s}$:

$$\alpha_k \to \alpha_k' = \alpha_k + \delta t \sum_{l=1}^{p} s_{k,l}^{-1} f_l. \tag{23}$$

Again, using the analogy with the steepest descent method, convergence to the energy minimum is reached when the value of δt is sufficiently small and is kept positive constant for each iteration. In fact, similarly to the steepest descent method, the energy variation corresponding to a small change of the parameters is

$$\Delta E = -\delta t \sum_{k=1}^{p} \sum_{l=1}^{p} s_{k,l}^{-1} f_k f_l + \mathcal{O}(\delta t^2) \tag{24}$$

and is always negative for small enough δt, unless the minimum condition of $f_k = 0$ is reached and the variational parameters no longer change because $\delta\alpha_k = 0$. It should be noted here that the steepest descent method is a special case with the matrix $s = 1$ (unit matrix).

A more convenient choice for the matrix $s_{j,k}$ is given by[22]

$$s_{j,k} = \frac{\langle\Psi_{\{\alpha_k\}}|\hat{O}_j\hat{O}_k|\Psi_{\{\alpha_k\}}\rangle}{\langle\Psi_{\{\alpha_k\}}|\Psi_{\{\alpha_k\}}\rangle} - \frac{\langle\Psi_{\{\alpha_k\}}|\hat{O}_j|\Psi_{\{\alpha_k\}}\rangle}{\langle\Psi_{\{\alpha_k\}}|\Psi_{\{\alpha_k\}}\rangle}\frac{\langle\Psi_{\{\alpha_k\}}|\hat{O}_k|\Psi_{\{\alpha_k\}}\rangle}{\langle\Psi_{\{\alpha_k\}}|\Psi_{\{\alpha_k\}}\rangle}. \tag{25}$$

This matrix can be efficiently evaluated statistically, and similarly to the forces f_k, can be obtained within a VMC scheme once $O_k(x)$ are computed for a set of configurations $\{x_l\}$, $l = 1, 2, \ldots, M$ distributed according to the wave function squared $|\langle x|\Psi_{\{\alpha_k\}}\rangle|^2$, namely,

$$s_{j,k} = \frac{1}{M}\sum_{l=1}^{M} [O_j(x_l) - \bar{O}_j][O_k(x_l) - \bar{O}_k], \tag{26}$$

where $\bar{O}_k$ and $\bar{O}_j$ are defined in Eq. (19). For whatsoever choice of the M configurations $\{x_l\}$, this matrix remains positive definite regardless of the statistical noise (at most it has vanishing eigenvalues), because it is explicitly written in Eq. (26) as an overlap matrix in $\mathcal{R}^M$ between the p vectors $O_k(x_l) - \bar{O}_k$ $(k = 1, \ldots, p)$. In this paper, this generalized method defined by Eq. (23) with the matrix $\bar{s}$ given by Eq. (25) will be called the stochastic reconfiguration (SR) optimization method. It should be noted here that other convenient types of positive definite matrix have been recently proposed.[24,25] However for the present purpose the improvement does not appear important.

Let us next discuss why the choice Eq. (25) for the matrix $\bar{s}$ in the SR scheme [Eq. (23)] is particularly simple and convenient compared to the simplest steepest descent method. For a stable iterative method for the energy optimization, such as the SR method and the steepest descent one, a basic ingredient is that at each iteration the new set of parameters $\{\alpha_k'\}$ are determined close enough to the previous set $\{\alpha_k\}$ in terms of a prescribed distance. The fundamental difference between the SR minimization and the standard steepest descent method is simply related to the definition of this distance Δ_α.

Within the SR scheme, Δ_α is chosen to be the square distance between the two normalized wave functions corre-

sponding to the two different sets of variational parameters $\{\alpha_k'\}$ and $\{\alpha_k\}$, i.e.,

$$\Delta_\alpha^{(SR)} = 2 - 2\frac{\langle\Psi_{\{\alpha_k\}}|\Psi_{\{\alpha_k'\}}\rangle}{\sqrt{\langle\Psi_{\{\alpha_k\}}|\Psi_{\{\alpha_k\}}\rangle\langle\Psi_{\{\alpha_k'\}}|\Psi_{\{\alpha_k'\}}\rangle}}. \tag{27}$$

The reason to normalize the two wave functions before computing their distance is obvious because, within a VMC scheme, the normalization of the wave function is irrelevant for quantum mechanical averages. The basic advantage of the SR method is the possibility to work directly with the wave function distance $\Delta_\alpha^{(SR)}$. In fact, this quantity can be explicitly written in terms of the matrix $\bar{s}$ [Eq. (25)] by substituting Eq. (15) in its definition Eq. (27), yielding

$$\Delta_\alpha^{(SR)} = \sum_{k=1}^{p} \sum_{l=1}^{p} s_{k,l}(\alpha_k' - \alpha_k)(\alpha_l' - \alpha_l) + O(|\alpha_k - \alpha_k'|^3). \tag{28}$$

Therefore the most convenient change of the variational parameters is to minimize the functional

$$\mathcal{F}(\{\alpha_k' - \alpha_k\}) = \Delta E + \bar{\Lambda}\Delta_\alpha^{(SR)}.$$

Here ΔE is the linear change in the energy $\Delta E = -\Sigma_k f_k(\alpha_k' - \alpha_k)$, and for $\Delta_\alpha^{(SR)}$ the leading term of the expansion in small $\alpha_k' - \alpha_k$ given in Eq. (28) can be used. $\bar{\Lambda}$ is a Lagrange multiplier that allows for a stable minimization with small change $\Delta_\alpha^{(SR)}$ of the wave function $|\Psi_{\{\alpha_k\}}\rangle$. Then the stationary condition $\delta\mathcal{F}(\{\alpha_k' - \alpha_k\})/\delta(\alpha_k' - \alpha_k) = 0$ naturally leads to the SR iteration scheme described by Eq. (23) with $\delta t = 1/(2\bar{\Lambda})$.

In a similar manner, it is also possible to obtain the standard steepest descent method. In this case the Cartesian metric defined in the p-dimensional space of the variational parameters is implicitly assumed to distinguish the two sets of variational parameters, i.e., the distance here is defined to be

$$\Delta_\alpha^{(SD)} = \sum_{k=1}^{p} (\alpha_k' - \alpha_k)^2.$$

The same argument used above to minimize $\Delta E + \bar{\Lambda}\Delta_\alpha^{(SD)}$ with respect to the variational parameter change $\alpha_k - \alpha_k'$ will then lead to the standard steepest descent algorithm described by Eq. (17).

The advantage of the SR method compared with the steepest descent one is now transparent. Sometimes a small change of the variational parameters corresponds to a large change of the wave function, and conversely a large change of the variational parameters can imply only a small change of the wave function. The SR method takes into account this effect through a better definition of the distance $\Delta_\alpha^{(SR)}$ [Eq. (27)].

Here a single SR iteration of the SR minimization scheme is summarized as follows: (i) a set of variational parameters $\{\alpha_k\} = \{\alpha_k^{(i)}\}$ is given after the ith iteration, (ii) the generalized force f_k [Eqs. (16) and (18)] and the matrix $\bar{s}$ [Eqs. (25) and (26)] are calculated statistically using a small variational
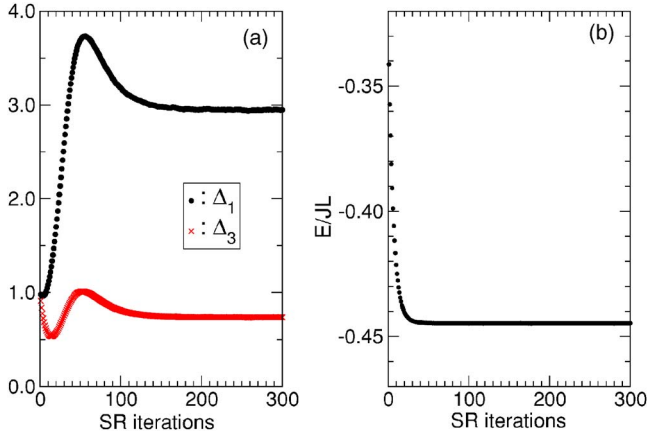
FIG. 2. (Color online) Monte Carlo evolution of (a) variational parameters (Δ_1 and Δ_3) and (b) energy as a function of stochastic reconfiguration (SR) iterations for the 1D spin-1/2 antiferromagnetic Heisenberg model $\hat{H}_{1D}$ on a $L=22$ ring. Here the SR method with $\delta t = 0.2/J$ [Eq. (23)] is used. In (a), Δ_1 and Δ_3 are the two variational parameters of the wave function (for details, see Sec. III B), which are both initialized to the value $\Delta_1 = \Delta_3 = 1$. In (b), at each iteration, the energy is computed by a small VMC simulation for the wave function with the fixed variational parameters given at the corresponding iteration in (a).

Monte Carlo simulation (bin) containing typically a few thousand samples ($M = 1000$–$10\,000$) distributed according to the wave function squared $|\Psi_{\{\alpha_k\}}(x)|^2$, and (iii) a new set of the variational parameters $\{\alpha_k^{(i+1)}\}$ is determined from Eq. (23) with a suitable choice of δt. After a few hundred (or sometimes thousand) SR iterations needed for equilibration, the iteration described above is further repeated to statistically average the optimized variational parameters until the desired statistical accuracy is reached. This method allows for a very accurate determination of the optimized variational parameters with very small statistical uncertainty. In the present study, all the variational parameters are optimized using this SR minimization method.

A sample case study for the SR minimization scheme is presented in Fig. 2 for the 1D antiferromagnetic Heisenberg model on a $L=22$ ring. As seen in Fig. 2, after the first few hundred SR iterations needed for equilibration, the variational parameters fluctuate around the stable mean values. It is interesting to notice in Fig. 2 that the variational parameters may continue to change substantially, even after the energy appears to reach its equilibrium value only after the first $\simeq 50$ SR iterations. The reason is that a very tiny energy gain, not visible in this plot, is implicitly reached at equilibrium, by satisfying very accurately the Euler condition of minimum energy, i.e., $f_k = 0$ for $k = 1, 2, \ldots, p$. A stochastic minimization method such as the steepest descent method or the SR one, which is based not only on the energy but also on its derivatives (f_k), is therefore much more efficient, especially for statistical methods where energy differences for slight changes of the variational parameters are often very noisy.

Having determined the optimized variational parameters $\{\alpha_k^*\}$ as described above, a single standard VMC simulation

is performed to calculate various physical quantities for $|\Psi_{\{\alpha_k^*\}}\rangle$ using a bin length much larger than the one used in the SR minimization procedure. Nevertheless, the mentioned Euler conditions ($f_k = 0$ for all k) are usually satisfied within a few standard deviations simply because the statistically averaged variational parameters are much more accurate than the ones obtained at the final SR iteration.[26]

C. Effective Hamiltonian approach

As is well known, within the variational approach, it is sometimes very difficult to describe long range properties accurately. This is simply because these long range properties are rather insensitive to the energy, which is instead determined mainly by short range correlation functions. A clear example of this limitation is found when this method is applied, for instance, to study the long range antiferromagnetic order for the spin-1/2 antiferromagnetic Heisenberg model on the square lattice. The long range antiferromagnetic order is now considered a well accepted and established property of this model.[27–29] Nevertheless it has been shown in Ref. 30 that two wave functions with completely different long-distance properties, with or without antiferromagnetic long range order, provide similar and very accurate (within 0.1% accuracy) energy per site in the thermodynamic limit.

Here we shall consider a possible way to overcome this limitation of the variational method by introducing what will be named the "effective Hamiltonian approach" in the following. The main idea of this method is to approximate, as accurately as possible, the exact Hamiltonian $\hat{H}$ by an effective Hamiltonian $\hat{H}^{\text{eff}}$, for which the exact ground state can be numerically sampled by Green function quantum Monte Carlo schemes. The important point is that, within this construction, some of the important short range properties of the Hamiltonian $\hat{H}$ are preserved, and therefore a much better control of correlation functions is achieved compared to a mere variational approach.

The short range properties of the Hamiltonian $\hat{H}$ can be conveniently defined in the configuration basis $\{x\}$. Each element of this basis is defined by the positions and spins of the N electrons. In this basis the matrix elements of the Hamiltonian $\hat{H}$ are then indicated by $\langle x | \hat{H} | x' \rangle = H_{x,x'}$. In this paper, we define a short range Hamiltonian as a Hamiltonian $\hat{H}$ for which the *off-diagonal* matrix elements $H_{x,x'}$ are nonzero only for configurations x and x' connected one to the other by local short-range "moves" of electrons (e.g., hoppings or spin-flips). More precisely,

$$\begin{cases} H_{x',x} \neq 0 & \text{for } |x - x'| \leq \text{R}, \\ H_{x',x} = 0 & \text{otherwise}, \end{cases} \quad (29)$$

where R determines the range of the off-diagonal matrix elements. In this definition, not only conventional Hubbard, Heisenberg, and $t-J$ models can be thought of short range Hamiltonians (with R=1), but also models with any interaction $\hat{V}$ which is diagonal in the configuration basis $\{x\}$ ($V_{x,x'} \propto V_x \delta_{x,x'}$), e.g., the long range Coulomb interactions, can be considered short range Hamiltonians. Therefore,

within this definition, most of the physically relevant Hamiltonians are short range, essentially because quantum fluctuations are important only through the short range off-diagonal matrix elements, in the absence of which the Hamiltonian is simply classical.

At present, short-range spin Hamiltonians which can be solved numerically by quantum Monte Carlo methods are the ones for which the quantity

$$s_{x',x} = \psi_G(x') H_{x',x} \psi_G(x) < 0 \qquad (30)$$

is strictly negative for all nonzero matrix elements $H_{x',x}$. Whenever a wave function $\psi_G(x)$ satisfying this condition exists, a unitary transformation $H_{x,x'} \rightarrow \text{sgn}[\psi_G(x)]\text{sgn}[\psi_G(x')]H_{x,x'}$ transforms the Hamiltonian to a standard bosonic one (namely, with all nonpositive off-diagonal matrix elements) that can be solved numerically with quantum Monte Carlo techniques, without facing the so-called "sign problem."[31] For instance, for the antiferromagnetic Heisenberg model in any bipartite lattice, a particularly simple variational wave function $\langle x | \psi_G \rangle = \psi_G(x)$ satisfying the Marshall sign rule $\psi_G(x) \propto (-1)^{N_A}$, allows one to satisfy the condition $s_{x,x'} < 0$, where N_A is the number of electrons with down spin on one of the sublattices for the given configuration $\{x\}$ (see Appendix B). With this wave function $\psi_G(x)$, it is therefore possible to solve numerically the spin-1/2 antiferromagnetic Heisenberg model in 1D, on a two-leg ladder, and on the 2D square lattice. In these cases, it is also clear that with the same Marshall sign of the wave function $\psi_G(x)$, different low energy properties can be obtained, i.e., a gapless spin liquid ground state for the single chain, a gapped spin liquid for the two-leg ladder, and a quantum antiferromagnet for the 2D limit.

However, as is well known, only for very particular models the Marshall sign rule and Eq. (30) are satisfied,[28,29,32] and in general Eq. (30) is violated regardless of the wave function $|\psi_G\rangle$ used. Even when a wave function $|\psi_G\rangle$ with the optimal signs, i.e., the exact GS signs, is used for generic frustrated Hamiltonians, there still exist off-diagonal matrix elements with $s_{x,x'} > 0$ (notorious sign problem). Namely, due to frustration, they do not decrease the energy expectation value.

In order to overcome this difficulty and treat more generic models, we will define below an effective Hamiltonian $\hat{H}^{\text{eff}}$, which is closely related to $\hat{H}$, by using an optimal wave function $\psi_G(x)$, which is named in the following the "guiding function." This guiding wave function is required to be nonzero for all configurations $\{x\}$. Even if this requirement is not satisfied, all the forthcoming analysis remains valid in the subspace of configurations $\{x\}$ for which $\psi_G(x) \neq 0$. Once the guiding wave function is provided and thus $\hat{H}^{\text{eff}}$ is defined, the effective model system $\hat{H}^{\text{eff}}$ is solved exactly using the standard Green function quantum Monte Carlo method.[33] As will be shown later, the low energy properties of $\hat{H}^{\text{eff}}$ are weakly dependent on the low energy properties, i.e., long range behavior, of $\psi_G(x)$.

The GS wave function of $\hat{H}$ is approximated by the GS of an effective Hamiltonian $\hat{H}^{\text{eff}}$. This approximate variational state is very good in energy because most of the matrix elements of $\hat{H}$ are treated exactly in $\hat{H}^{\text{eff}}$, whereas the remaining ones are removed and traced to the diagonal terms of $\hat{H}^{\text{eff}}$. As it will be shown later on, this enforces the constraint that the GS of $\hat{H}^{\text{eff}}$ has the same non trivial signs of $\psi_G(x)$. Therefore, if $\psi_G(x)$ is chosen to have the same signs of the exact ground state of $\hat{H}$ for most configurations, this approach becomes essentially exact.[34]

Within the effective Hamiltonian approach, the problem to construct an accurate approximate wave function for the GS of $\hat{H}$ is therefore related to how to know phases of the GS. This, we believe, is a much simpler task, because a good variational wave function of a short range Hamiltonian should provide also good phases. In fact, the variational energy of the guiding function $|\psi_G\rangle$

$$E(\psi_G) = \frac{\displaystyle\sum_{x,x'} \text{sgn}[s_{x,x'}] |\psi_G(x)\psi_G(x')H_{x,x'}|}{\displaystyle\sum_x |\psi_G(x)|^2},$$

depends strongly on the signs of $\psi_G(x)$ via the short range terms appearing in $s_{x,x'}$. This assumption that a variational wave function with accurate energy should have very good signs can be checked directly on small size clusters. Moreover, for the nearest neighbor antiferromagnetic Heisenberg model on the square lattice, it is known that all good variational wave functions satisfy the Marshall sign rule, although they may display different large distance behaviors.[30] This fact clearly confirms this assumption because all these wave functions differ only in their amplitudes but not in their phases.

From these considerations, in this paper, we will choose as a guiding function the projected BCS wave function $|p\text{-BCS}\rangle$ described in the previous subsection with the variational parameters optimized for each J'/J by a careful energy minimization using the SR scheme (Sec. II B). In most cases, due to the quality of the guiding function used, no relevant corrections are found in the various large distance correlations calculated for $|p\text{-BCS}\rangle$ when these are compared with the ground state correlations of $\hat{H}^{\text{eff}}$. In some special cases, the use of the effective Hamiltonian approach is instead of crucial importance.

1. Definition of the effective Hamiltonian

As mentioned previously, the effective Hamiltonian $\hat{H}^{\text{eff}}$ is defined in terms of the matrix elements of $\hat{H}$, which are chosen to generate a dynamic as close as possible to the exact one. An obvious condition to require is that if $|\psi_G\rangle$ is exact, then the ground state of $\hat{H}^{\text{eff}}$ and its eigenvalue have to coincide with the ones of $\hat{H}$. In order to fulfill this condition, the so-called lattice fixed node (FN) was proposed.[35] In the standard lattice fixed node approach, all the matrix elements which satisfy Eq. (30) are unchanged, whereas the remaining

off-diagonal matrix elements are dealt semiclassically and traced to the diagonal term, defining the standard FN Hamiltonian $\hat{H}^{\mathrm{eff}} = \hat{H}^{\mathrm{FN}}$. The FN Hamiltonian $\hat{H}^{\mathrm{FN}}$ is obtained by modifying its diagonal elements in a way that the local energies corresponding to the FN Hamiltonian $\hat{H}^{\mathrm{FN}}$ and the exact one $\hat{H}$ coincide for all configuration x, namely,

$$\frac{\langle \psi_G | \hat{H} | x \rangle}{\langle \psi_G | x \rangle} = \frac{\langle \psi_G | \hat{H}^{\mathrm{FN}} | x \rangle}{\langle \psi_G | x \rangle}, \tag{31}$$

and therefore the FN Hamiltonian is defined by

$$H_{x',x}^{\mathrm{FN}} = \begin{cases} H_{x',x} & \text{if } x' \neq x \text{ and } s_{x',x} \leqslant 0, \\ 0 & \text{if } x' \neq x \text{ and } s_{x',x} > 0, \\ H_{x,x} + \mathcal{V}^{\mathrm{sf}}(x) & \text{if } x' = x, \end{cases} \tag{32}$$

where

$$\mathcal{V}^{\mathrm{sf}}(x) = \sum_{\{x'(\neq x), s_{x',x} > 0\}} \psi_G(x') H_{x',x} / \psi_G(x).$$

The FN approach was inspired from the similar fixed node method on continuous systems,[16] and indeed is a well established approach[35] which provides also variational upper bounds of the exact ground state energy E_0, i.e., $E_0 \leqslant E_0^{\mathrm{FN}} \leqslant E(\psi_G)$ where E_0^{FN} is the ground state energy of $\hat{H}^{\mathrm{FN}}$.

As we will show below, for lattice systems there is a better way to choose this effective Hamiltonian,[36] which not only provides better variational energies, but also allows for a better accuracy of the low energy long distance properties of the ground state. For this end, it is important to notice the following key difference between a lattice system and a continuous one: in the lattice system the configurations $\{x\}$ which do not satisfy the condition (30) may be a relevant fraction of the total number of configurations, whereas in the continuous case such configurations represent just an irrelevant "nodal surface" of the phase space. Therefore dropping all the off-diagonal matrix elements with $s_{x,x'} > 0$ as in the standard FN method seems to be a too drastic approximation for the lattice case. This approximation can be indeed improved for lattice systems because, contrary to the continuous case, the FN Hamiltonian does not provide the best variational state with the same signs of the chosen guiding function $\psi_G(x)$.

The main consequence of neglecting all the off-diagonal matrix elements with $s_{x,x'} > 0$ is a bias of the dynamic, as electrons cannot move freely in some of the configurations. In order to compensate this bias in the diffusion of the electrons, we introduce a renormalization constant $K \leqslant 1$, which reduces the off-diagonal "hopping" in the allowed configurations with $s_{x,x'} < 0$:

$$H_{x',x}^{\mathrm{eff}} = \begin{cases} K H_{x',x} & \text{if } x' \neq x \text{ and } s_{x',x} \leqslant 0, \\ 0 & \text{if } x' \neq x \text{ and } s_{x',x} > 0, \\ H_{x,x} + \mathcal{V}^{\mathrm{sf}}(x) & \text{if } x' = x, \end{cases} \tag{33}$$

whereas in order to satisfy the condition (31) $\mathcal{V}^{\mathrm{sf}}$ is modified as follows:

$$\mathcal{V}^{\mathrm{sf}}(x) = (1 - K) \sum_{\{x'(\neq x), s_{x',x} < 0\}} \psi_G(x') H_{x',x} / \psi_G(x)$$

$$+ \sum_{\{x'(\neq x), s_{x',x} > 0\}} \psi_G(x') H_{x',x} / \psi_G(x). $$

2. Optimal choice for the constant K

Whenever there is no sign problem and $s_{x,x'} \leqslant 0$, $K = 1$ is obviously the best choice for which $\hat{H} = \hat{H}^{\mathrm{eff}}$. Also this choice $K = 1$ coincides with the standard lattice FN approach [Eq. (32)] (which will be denoted by the acronymous FN). Conversely, when the sign of the off-diagonal term in $\hat{H}$ are frustrated ($s_{x,x'} \geqslant 0$), a better choice of the constant K can be obtained by using a relation which has been well known for continuous systems, and used to correct efficiently the error due to the finite time slice discretization in the diffusion Monte Carlo (DMC) calculations.[37]

Let us first discuss this relation used in DMC before considering the lattice case. In the DMC, the small imaginary time ($\Delta \tau$) evolution of the electron configurations is governed by the exact Hamiltonian propagation $|\psi\rangle \rightarrow \exp(-\hat{H} \Delta \tau) |\psi\rangle$, with a diffusion coefficient D determined only by the free kinetic operator in $\hat{H}$. It is then possible to correct the approximate finite $\Delta \tau$ dynamic corresponding to the fixed node Hamiltonian, by requiring that it satisfies exactly the short time diffusion condition. This condition can be simply written as

$$[\vec{x}, [\hat{H}, \vec{x}]] = D, \tag{34}$$

where $D = 3\hbar^2/m$ is the diffusion coefficient in three dimensions, and $\vec{x}$ is the electron position operator.

For lattice systems with periodic boundary conditions (PBC), the position operator $\vec{x}$ is not well defined, as it cannot be matched with the boundary conditions. This limitation can be easily solved by using periodic spin position operators defined in the exponential form by

$$\hat{X}_\nu = \exp\left[i \sum_{\vec{R}} (\vec{h}_\nu \cdot \vec{R}) \hat{S}_{\vec{R}}^z \right], \tag{35}$$

where $\hat{S}_{\vec{R}}^z$ is the z component of the spin operator at site $\vec{R}$, and ν labels the spatial coordinates, e.g., $\vec{h}_x = (2\pi/l, 0)$ and $\vec{h}_y = (0, 2\pi/l)$ for a $L = l \times l$ square lattice. These operators are diagonal in the basis of configurations $\{x\}$, $\langle x | \hat{X}_\nu | x' \rangle = X_\nu(x) \delta_{x,x'}$, as is the analogous position operator $\vec{x}$ in the continuous case. Remarkably $\hat{X}_\nu$ is exactly equivalent to the well known Lieb-Schultz-Mattis operator, used to show a well known property on the low energy spectrum of spin-1/2 Heisenberg Hamiltonians.[38] After simple inspection, a relation similar to Eq. (34) can be found also for the periodic spin position operators $\hat{X}_\nu$, by simply imposing the following equation:

$$\langle\psi_G|[\hat{X}_\nu^\dagger,[\hat{H},\hat{X}_\nu]]|\psi_G\rangle = \langle\psi_G|[\hat{X}_\nu^\dagger,[\hat{H}^{\mathrm{eff}},\hat{X}_\nu]]|\psi_G\rangle. \quad (36)$$

For the lattice case, both the left hand side and the right hand side of this relation have non trivial expectation values. Both of them can be simply calculated by a standard VMC method without particular difficulty, after recasting them in a more conventional form for VMC calculations

$$\langle\psi_G|[\hat{X}_\nu^\dagger,[\hat{\mathcal{H}},\hat{X}_\nu]]|\psi_G\rangle$$
$$= -\sum_x\sum_{x'}\psi_G(x)\psi_G(x')\mathcal{H}_{x,x'}|X_\nu(x) - X_\nu(x')|^2$$
$$= -\sum_x|\psi_G(x)|^2\left[\sum_{x'}\psi_G(x')\mathcal{H}_{x,x'}|X_\nu(x) - X_\nu(x')|^2/\psi_G(x)\right], \quad (37)$$

a relation that is obviously valid both for $\mathcal{H}=\hat{H}$ and for $\mathcal{H}=\hat{H}^{\mathrm{eff}}$. Here we assumed $\mathcal{H}_{x,x'}=\mathcal{H}_{x',x}$. Therefore, similarly to the continuous scheme,[37] the value of the constant K can be determined from Eq. (36) with high statistical accuracy. Note that if there is no sign problem, i.e., $s_{x,x'}\leq 0$ for all configurations $\{x\}$, the constant K turns out to be exactly one with vanishing statistical error, yielding again $\hat{H}^{\mathrm{eff}}=\hat{H}$.

After determining the constant K, the effective Hamiltonian $\hat{H}^{\mathrm{eff}}$ [Eq. (33)] is defined, and the ground state $|\psi_0^{\mathrm{eff}}\rangle$ with its eigenvalue E_0^{eff} and the corresponding low energy excitations of $\hat{H}^{\mathrm{eff}}$ can be computed using the standard Green function quantum Monte Carlo method[33] without sign problem.

To compute the expectation value of the energy

$$E(\psi_0^{\mathrm{eff}}) = \frac{\langle\psi_0^{\mathrm{eff}}|\hat{H}|\psi_0^{\mathrm{eff}}\rangle}{\langle\psi_0^{\mathrm{eff}}|\psi_0^{\mathrm{eff}}\rangle} \quad (38)$$

using $|\psi_0^{\mathrm{eff}}\rangle$ as an approximate ground state for $\hat{H}$, the method described in Ref. 39 can be applied, which very often improves sizably the upper bound estimate of the energy, i.e., $E_0\leq E(\psi_0^{\mathrm{eff}})\leq E_0^{\mathrm{eff}}\leq E(\psi_G)$, even in the standard FN case with $K=1$.[37] As also remarked in Ref. 39, contrary to the continuous case, for lattice Hamiltonians the lowest variational energy $E(\psi_0^{\mathrm{eff}})$ does not correspond to $K=1$ in general. In the following, we will indicate by FNE the improved FN effective Hamiltonian method [Eq. (33)] with the constant $K\leq 1$ determined by the condition (36), using for $|\psi_G\rangle$ the lowest energy variational wave function of the form described in Sec. II A.

D. Calculation of dynamical correlation functions

The spin-one excitation spectrum of the effective Hamiltonian $\hat{H}^{\mathrm{eff}}$ can be calculated by applying the forward walking technique[33] used to evaluate the imaginary time evolution of the following quantity:
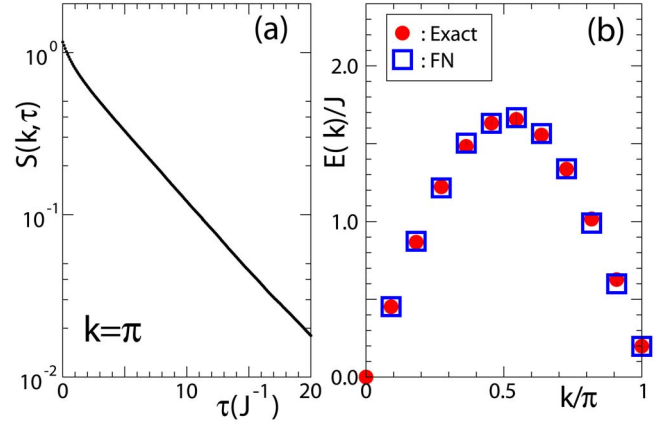

FIG. 3. (Color online) (a) Imaginary time τ evolution of $S(k,\tau)$ at $k=\pi$ for the 1D spin-1/2 antiferromagnetic Heisenberg model $\hat{H}_{\mathrm{1D}}$ on a $L=22$ ring. (b) Excitation energy $E(k)=E_k^{S=1}-E_0^{\mathrm{eff}}$ extracted from $S(k,\tau)$ with large τ shown in (a) (squares). The error bars are smaller than the size of the symbols. For comparison, the exact values are also presented by solid circles.

$$S(\mathbf{k},\tau) = \frac{\langle\psi_G|\hat{S}_\mathbf{k}^z e^{-\tau\hat{H}^{\mathrm{eff}}}\hat{S}_{-\mathbf{k}}^z|\psi_0^{\mathrm{eff}}\rangle}{\langle\psi_G|e^{-\tau\hat{H}^{\mathrm{eff}}}|\psi_0^{\mathrm{eff}}\rangle}, \quad (39)$$

where $\hat{S}_\mathbf{k}^z = \frac{1}{\sqrt{L}}\Sigma_\mathbf{r}e^{i\mathbf{k}\cdot\mathbf{r}}\hat{S}_\mathbf{r}^z$ and $|\psi_0^{\mathrm{eff}}\rangle$ is the ground state of $\hat{H}^{\mathrm{eff}}$. Note that the imaginary time propagation in Eq. (39) can be evaluated without discretization errors in time τ, as is common to many other Quantum Monte Carlo techniques,[40] and also pointed out in Ref. 41 for the present Monte Carlo scheme. By simple inspection, the spin one excitation energy $E_\mathbf{k}^{S=1}$ of $\hat{H}^{\mathrm{eff}}$ for momentum $\mathbf{k}$ can be calculated by fitting the large imaginary time behavior of $S(\mathbf{k},\tau)\propto\exp[-E(\mathbf{k})\tau]$. Here $E(\mathbf{k})=E_\mathbf{k}^{S=1}-E_0^{\mathrm{eff}}$ and E_0^{eff} is the ground state energy of $\hat{H}^{\mathrm{eff}}$. Thus we fit $\ln S(\mathbf{k},\tau)$ with

$$\ln S(\mathbf{k},\tau) = -\tau E(\mathbf{k}) + A + B\ln(\tau) \quad (40)$$

for $\tau\gtrsim\tau_\mathrm{c}$, where A, B, and $E(\mathbf{k})$ are fitting parameters, and τ_c is a suitable cutoff time, large enough so that the fitting form (40) can be used with good accuracy. In fact, the present fit is very stable in τ, and a satisfactory convergence of $E(\mathbf{k})$ is obtained even for relatively small $\tau_c\simeq 2/J$.

As a typical example, Fig. 3(a) shows a semilog plot of $S(k,\tau)$ at $k=\pi$ for the 1D spin-1/2 antiferromagnetic Heisenberg model $\hat{H}_{\mathrm{1D}}$. It is clearly seen that for a wide region of $\tau\gtrsim 2/J$, $\ln S(k,\tau)$ is linear so that we can safely estimate the excitation energy $E(\mathbf{k})$ with Eq. (40). The error bars for $E(\mathbf{k})$ can be efficiently evaluated by using the "bootstrap technique,"[42] because the numerator and the denominator of Eq. (39) are highly correlated. To demonstrate the accuracy and reliability of the method, the calculated $E(\mathbf{k})$ for $\hat{H}_{\mathrm{1D}}$ is shown in Fig. 3(b). As seen in the figure, the agreement between our results and the exact values is excellent.

It is worthwhile to emphasize that, within this method, a single Monte Carlo simulation allows one to calculate all the lowest spin one excitation energies for various momenta with no extra effort. Moreover, the method is not restricted to the

computation of the spin triplet spectrum alone, but can be easily generalized to arbitrary operators $\hat{O}$ as long as they are diagonal in terms of the chosen basis $\{x\}$. Although the high energy excitations are more difficult to calculate because the signal decays much faster in time, the most important low energy spectrum can be accurately determined.

III. NUMERICAL RESULTS

A. Projected BCS wave functions and particle-hole symmetry

Before presenting our numerical results, here we will show an important relation between the projected BCS wave function $|p\text{-BCS}\rangle$ and the particle-hole symmetry,[43] which turns out to be crucial to differentiate spin systems defined on the conventional nonfrustrated square lattice and the ones defined on the triangular lattice geometry. In both cases each site of the lattice is represented by a vector $\mathbf{r}=r_1\vec{\tau}_1+r_2\vec{\tau}_2$ with r_1 and r_2 being integer (see, e.g., Fig. 1). Then a particle-hole transformation is defined with

$$c_{\mathbf{r},\sigma}^\dagger \rightarrow (-1)^{r_1+r_2}c_{\mathbf{r},\sigma}, \qquad (41)$$

or in the reciprocal lattice space with the reciprocal lattice vectors $\vec{g}_1$ and $\vec{g}_2$, this transformation is equivalently defined with

$$c_{\mathbf{k},\sigma}^\dagger \rightarrow c_{-\mathbf{k}+\mathbf{Q},\sigma}, \qquad (42)$$

where $\mathbf{Q}=(\vec{g}_1+\vec{g}_2)/2$. As shown in Appendix B, whenever the BCS Hamiltonian $\hat{H}_{\text{BCS}}$ is invariant under the particle-hole transformation and $\Delta_{\mathbf{k}}$ is real, i.e.,

$$\epsilon_{\mathbf{k}} = -\epsilon_{-\mathbf{k}+\mathbf{Q}},$$

$$\Delta_{\mathbf{k}} = -\Delta_{-\mathbf{k}+\mathbf{Q}},$$

$$\mu = 0, \qquad (43)$$

the corresponding projected BCS wave function $|p\text{-BCS}\rangle$ [Eq. (8)] satisfies the so-called Marshall sign rule.[44] The Marshall sign rule is an exact property for the ground state of the spin-1/2 antiferromagnetic Heisenberg model on nonfrustrated lattices such as the square lattice, and indeed for these models the minimum variational energy is achieved when this rule is satisfied by the projected BCS wave function $|p\text{-BCS}\rangle$.

B. One dimensional limit and spin fractionalization

We shall first show the results for the uncoupled chain limit, i.e., for the 1D spin-1/2 antiferromagentic Heisenberg model with nearest neighbor coupling:

$$\hat{H}_{1D} = J\sum_{\langle i,j\rangle} \vec{S}_i \cdot \vec{S}_j. \qquad (44)$$

Several previous studies[18,45] have found that the ground state of $\hat{H}_{1D}$ can be described very accurately by the projected BCS wave function $|p\text{-BCS}\rangle$ [Eq. (8)] with only the nearest neighbor hopping $t_{i,j}=\delta_{i,j\pm 1}$ and the first three neighbors for the gap function $\Delta_{i,j}=\Delta_l\delta_{i,j\pm l}(l=1,2,3)$. Here the site-$i$ is

represented by the vector $\vec{r}_i=i\vec{\tau}_1$. Notice that the ground state of $\hat{H}_{1D}$ satisfies the Marshall sign rule, and therefore from Eq. (43) with $Q=\pi$, μ and Δ_l with l even have to be identically zero. It was also pointed out[18] that the inclusion of the third neighbor gap function Δ_3 is crucial to improve the accuracy of the $|p\text{-BCS}\rangle$. As shown in Fig. 2(a), the optimized parameters for $L=22$ are $\Delta_1=2.947\pm 0.003$ and $\Delta_3=0.737\pm 0.002$ with the notations of Eq. (7), i.e., $\Delta_k=2\Delta_1\cos k+2\Delta_3\cos 3k$. The corresponding variational estimate of the total energy is $E/J=-9.78411\pm 0.00005$ which is in excellent agreement with the exact value of $E/J=-9.78688$. For larger clusters the variational parameters change slightly and smoothly, and the same kind of accuracy is obtained even in the infinite size limit. By simple quadratic (linear) extrapolation in $1/L$ for the energy (Δ_l) with data up to $L=150$ sites, we found $E/JL=-0.442991(3)$ [$\Delta_1=3.41(3)$, $\Delta_3=0.90(1)$] which compares very well with the well known exact value $E/JL=-(\ln 2-1/4)=-0.443147$. This result suggests that our variational method is particularly accurate in describing this 1D exactly solvable case, which is precisely our starting point for studying weakly coupled chains with $J'\neq 0$.

In the rest of this subsection, we shall show that also the low-energy excited states can be described by projected BCS states. As we mentioned above, to satisfy the Marshall sign rule, the optimized variational parameters in $|p\text{-BCS}\rangle$ meet the constraint relation (43) with $Q=\pi$. Therefore, the spin-1/2 BCS excitation spectrum E_k [Eq. (10)] shows gapless excitations at $k=\pm Q/2$, in perfect agreement with the exact spinon spectrum of the Bethe-ansatz solution.[14] Since the elementary excitations of the BCS Hamiltonian with energy $E_{\mathbf{k}}$ are described by the standard Bogoliubov modes[46]

$$\gamma_{k,\uparrow}^\dagger = u_k c_{k,\uparrow}^\dagger - v_k c_{-k,\downarrow},$$

$$\gamma_{-k,\downarrow} = v_k c_{k,\uparrow}^\dagger + u_k c_{-k,\downarrow}, \qquad (45)$$

the simplest variational state for the spinon at momentum $\mathbf{k}$ is

$$|\mathbf{k}\rangle = \mathcal{P}_G \gamma_{k,\downarrow}^\dagger |\text{BCS}\rangle. \qquad (46)$$

To see whether this state $|\mathbf{k}\rangle$ corresponds to a spinon state, we consider a ring with *odd* number of sites $L=31$ and z component of the total spin $S_z^{\text{tot}}=-1/2$. For this case it is known that a well defined spinon exists only for half of the total Brillouin zone $(\pi/2\leq|\mathbf{k}|\leq\pi)$.[47] For this branch, as shown in Fig. 4, the wave function $|\mathbf{k}\rangle$ represents very well a spinon with momentum $\mathbf{k}$, as can be verified by the good accuracy in the energy and its small variance

$$\sigma^2(|\mathbf{k}\rangle) = \frac{\langle\mathbf{k}|\hat{H}^2|\mathbf{k}\rangle}{\langle\mathbf{k}|\mathbf{k}\rangle} - \left[\frac{\langle\mathbf{k}|\hat{H}|\mathbf{k}\rangle}{\langle\mathbf{k}|\mathbf{k}\rangle}\right]^2. \qquad (47)$$

The variance $\sigma^2(|\mathbf{k}\rangle)$ is zero for an exact eigenstate, and is small for a very accurate variational state. As seen in Fig. 4, this is clearly the case for the momenta $|\mathbf{k}|\gtrsim\pi/2$.

For the remaining branch of momenta $(|\mathbf{k}|\lesssim\pi/2)$, the excitations for $\hat{H}_{1D}$ are no longer elementary.[47] As shown in Fig. 4, although the state $|\mathbf{k}\rangle$ is formally defined even for
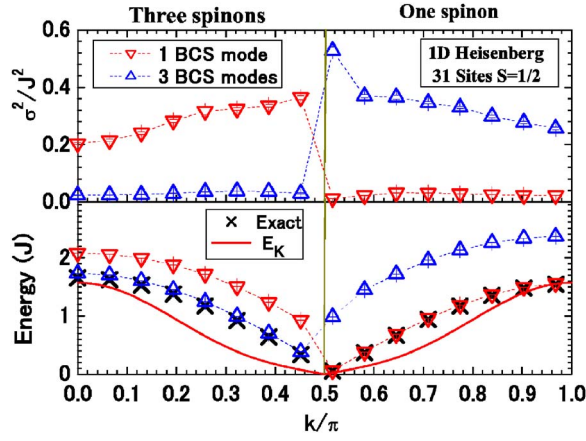
FIG. 4. (Color online) Lowest spin-1/2 excitation energy $E(k)$ and $E(k^{(3)})$ (lower panel) and the variance $\sigma^2(|k\rangle)$ and $\sigma^2(|k^{(3)}\rangle)$ (upper panel) of the projected BCS states with a single BCS mode $|k\rangle$ and three BCS modes $|k^{(3)}\rangle$ (see text) as a function of momentum k. The model studied is the 1D spin-1/2 antiferromagnetic Heisenberg model on a ring with $L=31$. For comparison, in the lower panel, the exact lowest excitation energy is plotted by crosses, and the BCS spectrum E_k denoted by dashed line is scaled by a factor to match the exact bandwidth. The remaining lines are guides to the eye.

those momenta, it represents a poor representation for the exact excited state. In fact $E(\mathbf{k})$ becomes quite off from the exact value, and $\sigma^2(|\mathbf{k}\rangle)$ considerably increases when the momentum crosses the "spinon Fermi surface." Remarkably, by projecting a nonelementary excitation of the BCS Hamiltonian, namely,

$$|\mathbf{k}^{(3)}\rangle = \mathcal{P}_G \gamma^\dagger_{\mathbf{k}_F,\downarrow} \gamma^\dagger_{-\mathbf{k}_F,\downarrow} \gamma^\dagger_{\mathbf{k},\uparrow} |\text{BCS}\rangle \qquad (48)$$

with $\mathbf{k}_F = \pi(L+1)/2L$, which mimics the correct three-spinon eigenstate, we can achieve a good agreement for the spectrum even in the region outside the spinon Fermi surface (see Fig. 4). Note that, although the projection $\mathcal{P}_G$ is crucial to gain a quantitative agreement for the spectrum, the BCS spectrum $E_\mathbf{k}$ already gives a qualitatively correct feature of gapless excitations with finite spinon velocity at the right momentum $\mathbf{k} = \pi/2$ (see Fig. 4).

Since the state $|\mathbf{k}\rangle$ [Eq. (46)] is very accurate only in the momentum region $\pi/2 \leq |\mathbf{k}| \leq \pi$, we conclude that only half of the elementary excitations of the BCS Hamiltonian remain to be well defined excitations for the spin Hamiltonian $\hat{H}_{1D}$ after applying the Gutzwiller projection $\mathcal{P}_G$. This effect is expected to hold also in a 2D fractionalized phase. It turns out that the elementary BCS excitations which describe the correct spinons after applying the projection operator $\mathcal{P}_G$ can be obtained by adiabatically switching off the gap function Δ_k, a process that defines naturally a Fermi surface, so that fermion quasiparticles can be created (destroyed) in unoccupied (occupied) states only.

In 2D it is very difficult to confirm directly the above "selection rules" of the Gutzwiller projection acting on the elementary BCS excitations. For instance, to study single spinon excitations, one might think of a 2D system on (l

$\times l$) lattice with l odd as a natural extention of the 1D system considered above. However this 2D system should contain many elementary excitations of spinons as it is easily understood by considering the $J' \to 0$ limit, and thus it is not an ideal system for studying single spinon excitations. Nevertheless, it is very important to have reached a very accurate 1D limit, with the correct spin fractionalization, within the present variational approach, because this approach can be easily extended to higher dimensions.

Finally, it is worth mentioning that, according to the gauge theory by Wen,[48,49] the low energy excitations of several 2D spin liquids described by this $|p\text{-BCS}\rangle$ variational ansatz, can be understood within the mean field level without taking into account the Gutzwiller projection, simply because this projection becomes irrelevant for large distance correlations. This is the case for a "Z_2 gapless spin liquid." Without entering into too much details of this theory, we only mention here that a Z_2 spin liquid can be described by a $|p\text{-BCS}\rangle$ for which no SU(2) gauge transformation—remaining in the restricted Hilbert space with no doubly occupation—allows one to eliminate the gap function in the corresponding BCS Hamiltonian. In such a case, only the gauge transformation $c_{i,\sigma} \to -c_{i,\sigma}$ leaves the BCS Hamiltonian unchanged, a transformation which defines the Z_2 group toghether with the identity operation. Most of the spin liquids which we will describe in this paper are Z_2 spin liquids in the triangular lattice geometry and should be stable according to the theory mentioned above.[48,49]

C. Weakly coupled chains in the triangular geometry with J'/J small

In this subsection, as a first step towards the 2D limit, we shall consider the spin-1/2 antiferromagnetic Heisenberg model for weakly coupled chains in the triangular lattice geometry with J'/J small (see Fig. 1). Note that this region is appropriate for the material Cs_2CuCl_4, where $J'/J \simeq 1/3$.[11]

1. Variational results

Motivated by the great success of the present variational approach in the 1D system discussed in the preceding subsection, the variational ansatz which we shall consider here for this 2D model in the region J'/J small is a similar projected BCS state $|p\text{-BCS}\rangle$ described by Eqs. (4)–(10). Here both $t_{i,j}$ and $\Delta_{i,j}$ in the BCS Hamiltonian [Eq. (4)] parametrizing $|p\text{-BCS}\rangle$ are assumed translational invariant, and therefore they depend only on the relative vector $\vec{l} = \vec{r}_i - \vec{r}_j = l_1 \vec{\tau}_1 + l_2 \vec{\tau}_2 = (l_1, l_2)$ (l_1 and l_2: integer) between the two sites i and j, i.e., $t_{\vec{l}}$ and $\Delta_{\vec{l}}$. Also the C_{2v} point group symmetry is assumed for the variational parameters, e.g., $\Delta_{\vec{l}} = \Delta_{\mathcal{R}_x \vec{l}} = \Delta_{\mathcal{R}_y \vec{l}} = \Delta_{\mathcal{R}_x \mathcal{R}_y \vec{l}}$ for the A_1 symmetry, where $\mathcal{R}_x$ ($\mathcal{R}_y$) is the reflection operator about the xz (yz) plane

$$\mathcal{R}_x \vec{l} = (l_1 + l_2) \vec{\tau}_1 - l_2 \vec{\tau}_2,$$

$$\mathcal{R}_y \vec{l} = -(l_1 + l_2) \vec{\tau}_1 + l_2 \vec{\tau}_2.$$

To optimize the variational wave function, we use the SR optimization method described in Sec. II B, which enables us

to determine the optimized variational parameters with very high accuracy.

As shown in Table I, the optimized $t_{\vec{l}}$ is found to be nonzero only for the nearest neighbors along the chain direction $\vec{\tau}_1$ (we set $t_{\vec{\tau}_1} = 1$), and negligible otherwise, whereas the optimized $\Delta_{\vec{l}}$ is instead found to be sizable even among different chains (for instance, $\Delta_{(2,1)}$, shown in Table I), displaying a true two dimensional character. It is also found that the symmetry of the gap function $\Delta_{\vec{l}}$ which minimizes the variational energy is the A_1 symmetry under the C_{2v} point group. Finite-size corrections to the variational parameters scale as $1/L$, and the 18×18 cluster is found large enough to be close to the thermodynamic limit, at least, for not too small values of J'/J. All the variational parameters for the 18×18 cluster as a function of $J'/J (\leqslant 0.7)$ are tabulated in Table I, along with the variational energy. It should be noted that since the Marshall sign rule is no longer satisfied for this model, the constraint relation (43) does not have to be met by the variational wave function. For example, as seen in Table I, the optimized chemical potential μ turned out to be different from zero.

To gain better insight on the physical nature and properties of these variational states, let us next evaluate the BCS excitation spectrum $E_{\mathbf{k}}$ given by Eq. (10) in the thermodynamic limit with the optimized variational parameters. In Figs. 5 and 6, the contour lines for $\xi_{\mathbf{k}} = \epsilon_{\mathbf{k}} - \mu = 0$ and $\Delta_{\mathbf{k}} = 0$ are plotted together with the boundary of the first Brillouin zone (BZ) of the triangular lattice for $J'/J = 0.33$ and 0.5, respectively.[50] As can be seen clearly from these figures, $\xi_{\mathbf{k}}$ and $\Delta_{\mathbf{k}}$ vanish at the same momenta with incommensurate "nodal" points, and thus the corresponding BCS excitation spectrum $E_{\mathbf{k}} = \sqrt{\xi_{\mathbf{k}}^2 + \Delta_{\mathbf{k}}^2}$ shows gapless excitations at these momenta. It is also interesting to notice that with increasing J'/J the shape of the contour line of the gap function $\Delta_{\mathbf{k}} = 0$ changes form open lines to a closed one in the BZ, acquiring a clear two dimensional characteristic. On the contrary, the minimum variational energy is always achieved with negligible values of the interchain hopping $t_{\vec{l}}$ even for the largest J'/J considered.

Before considering the 2D limit, it is important to discuss in more details the properties of few coupled chains in the triangular lattice geometry displayed in Fig. 1. If we consider only two chains in the $\vec{\tau}_1$ direction, this system corresponds to the well known zigzag ladder with couplings J and J'. It is now well established that the ground state of the zigzag ladder is spontaneously dimerized with dimers along the rungs ($\vec{\tau}_2$ direction) for $J'/J \lesssim 4$, and that the low-lying spin excitations are gapped.[51] For small values of J'/J, it is impossible at present to detect the dimer order parameter numerically on finite size clusters simply because this quantity vanishes exponentially for $J'/J \to 0$. However, it was also shown previously[52] that, for systems with finite number of chains, projected BCS wave functions can show spontaneous dimerization provided there is a gap in the corresponding BCS excitation spectrum $E_{\mathbf{k}}$. This is manifestly the case for the zigzag ladder system, as well as for any system with finite even number of chains, as the corresponding finite discretization for the momenta in the y direction do not allow us to fulfill simultaneously the two conditions $\Delta_{\mathbf{k}} = 0$ and $\xi_{\mathbf{k}} = 0$
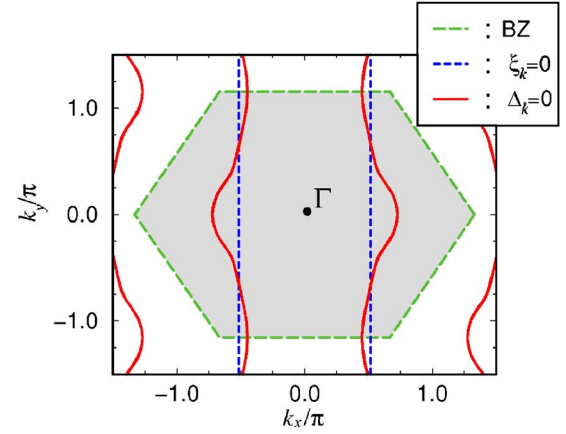

FIG. 5. (Color online) Loci of **k** points where $\xi_{\mathbf{k}} = 0$ (dashed lines) and $\Delta_{\mathbf{k}} = 0$ (solid lines) determined by using the optimized variational parameters for $J'/J = 0.33$. The boundary of the first Brillouin zone (BZ) for the triangular lattice is also denoted by long dashed lines.

and thus the presence of a gap in the BCS excitation spectrum is implied. Therefore, the projected BCS wave functions can naturally describe the crossover from a finite number of coupled chains, dimerized and gapped, to a gapless and fractionalized spin liquid in 2D, implying that the limit of infinite number of chains may be highly non trivial for a spin liquid wave function.

In order to understand the properties of the present projected BCS wave function $|p\text{-BCS}\rangle$, we now report several physical quantities. Figure 7 shows the spin-spin correlation functions

$$C(\vec{l}) = \frac{\langle \psi | \hat{S}_{\vec{r}}^z \hat{S}_{\vec{r}+\vec{l}}^z | \psi \rangle}{\langle \psi | \psi \rangle} \tag{49}$$

with $|\psi\rangle = |p\text{-BCS}\rangle$ calculated in the $\vec{\tau}_1$ and $\vec{\tau}_2$ directions for typical couplings with $J'/J = 0.33$ and $J'/J = 0.5$. As seen in Fig. 7, even though the interchain spin correlations are very small, the intrachain spin correlations are appreciably large, at least, for the clusters studied. In order to examine whether
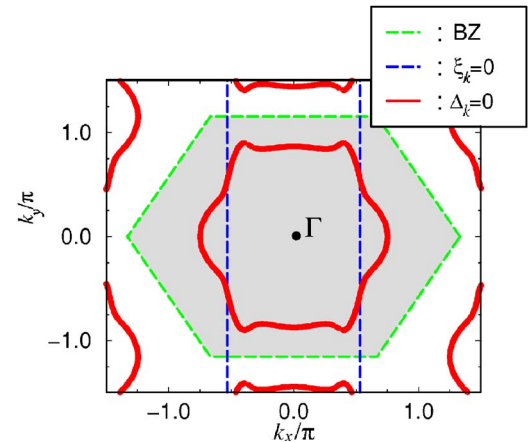

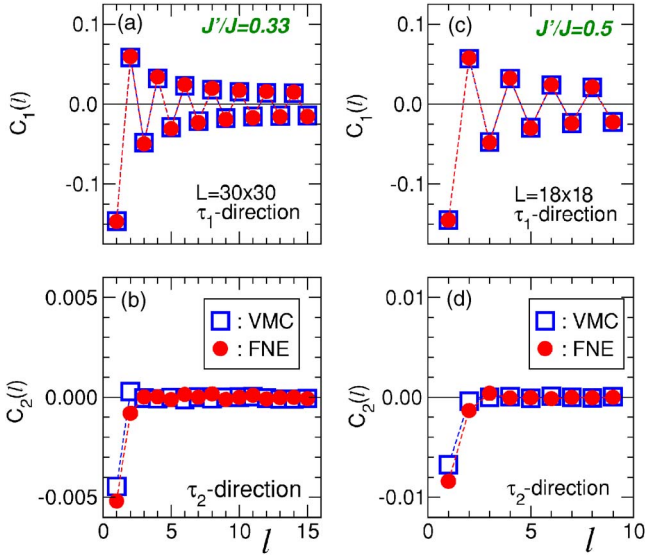FIG. 6. (Color online) The same as in Fig. 5 but for $J'/J = 0.5$.

FIG. 7. (Color online) Spin-spin correlation functions $C(\vec{r})$ with $\vec{r}=l_1\vec{\tau}_1+l_2\vec{\tau}_2$ for $J'/J=0.33$ [(a) and (b)] and $J'/J=0.5$ [(c) and (d)] calculated using both variational Monte Carlo (VMC) and effective Hamiltonian (FNE) methods. The cluster sizes used are 30×30 [(a) and (b)] and 18×18 [(c) and (d)]. $C_1(l)$ and $C_2(l)$ indicate $C(l\vec{\tau}_1)$ and $C(l\vec{\tau}_2)$, respectively.

magnetic long range order occurs, we have studied the system size dependence of $C(l_{max}\vec{\tau}_1)(=P_s)$ at the maximum distance (l_{max}) in the $\vec{\tau}_1$ direction compatible with periodic boundary conditions. There exists long range magnetic order only when P_s is finite in the thermodynamic limit. Our results of P_s are shown in Fig. 8(a) for $J'/J=0.33$ and clusters up to $L=42\times42$. From the finite size scaling presented in Fig. 8(a), it is clearly concluded that the projected BCS state $|p\text{-BCS}\rangle$ is not magnetically ordered. This is apparently expected because the projected BCS wave function $|p\text{-BCS}\rangle$ is a spin liquid state in 2D.

Another important quantity to study is the dimer-dimer correlation functions along the chain direction

$$D(\vec{l}) = \frac{\langle\psi|(\hat{S}_{\vec{r}}^z\hat{S}_{\vec{r}+\vec{\tau}_1}^z)(\hat{S}_{\vec{r}+\vec{l}}^z\hat{S}_{\vec{r}+\vec{l}+\vec{\tau}_1}^z)|\psi\rangle}{\langle\psi|\psi\rangle} - C(\vec{\tau}_1)^2. \quad (50)$$

As is well known, $D(\vec{l})$ shows undamped oscillations at large distance $|\vec{l}|\to\infty$ when there is a spontaneous broken translation symmetry characterized by a dimerized spin-Peierls phase. Since for systems with finite number of chains projected BCS wave functions show dimer order,[52] it is not surprising to see large oscillations in $D(\vec{l})$ as a function of the distance, as shown in Fig. 9 for $J'/J=0.33$. In order to rule out the possibility of a finite dimer order for the present projected BCS state in 2D, the system size dependence of the dimer order parameter P_d is studied in Fig. 8(b) for clusters up to $L=42\times42$. The square of this order parameter (P_d^2) is related to the calculated largest distance dimer correlations through
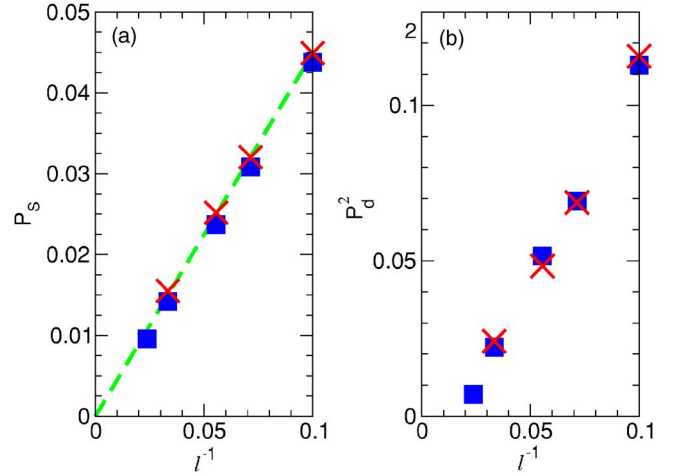

FIG. 8. (Color online) System size dependence of (a) spin-spin correlation functions $C(\vec{l})$ at the largest distance in the $\vec{\tau}_1$ direction (P_s) and (b) the dimer order parameter squared P_d^2 (see the text) for clusters of $L=l\times l$. The coupling studied is $J'/J=0.33$. The variational Monte Carlo and effective Hamiltonian (FNE) results are denoted by squares and crosses, respectively. The straight dashed line in (a) is a guide to the eye.

$$P_d^2 = 18\big|[D(l/2\vec{\tau}_1) - D((l/2-1)\vec{\tau}_1)]\big|$$

for a cluster of $L=l\times l$ sites.[53] As seen in Fig. 8(b), it is clear that $P_d\to0$ as $L\to\infty$. As expected, this projected BCS wave function $|p\text{-BCS}\rangle$ does not show spontaneous dimerization in 2D, and therefore it represents a genuine spin-liquid wave function.

2. Effective Hamiltonian results

One of the main advantage of our approach is that we can study the stability of the variational ansatz wave function using the effective Hamiltonian method described in Sec. II C.[17] Before showing our results, it should be noted first that one of the important quantities which measure the quality of our approximation in the effective Hamiltonian ap-
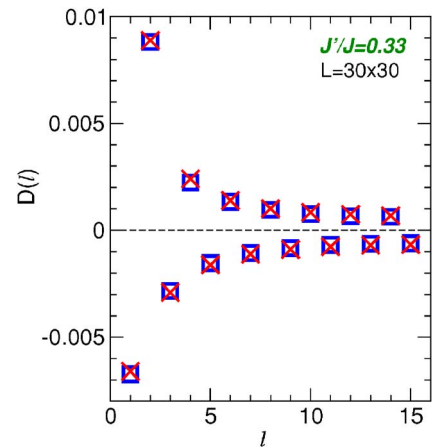

FIG. 9. (Color online) Dimer-dimer correlation functions $D(\vec{r})$ with $\vec{r}=l\vec{\tau}_1$ for $J'/J=0.33$ calculated using both variational Monte Carlo (squares) and effective Hamiltonian (crosses) methods.

proach is the effective constant K [determined as the result of Eq. (36)], $K=1$ meaning that there is no sign problem and the ground state of the effective Hamiltonian represents the exact ground state of $\hat{H}$. As shown in the Table I, we found that the effective constant K is indeed very close to one for all the cases studied. This indicates that the number of off-diagonal matrix elements, which cause the sign problem and are taken into account only approximately in $\hat{H}^{\text{eff}}$, represents only a very tiny fraction of the total number of matrix elements of $\hat{H}$. Therefore, $\hat{H}^{\text{eff}}$ is expected to be rather close to $\hat{H}$, and indeed it coincides with $\hat{H}$ in the large anisotropic limit $J'/J \to 0$, where there is no sign problem.

Encouraged by this observation, we have calculated the spin-spin correlation functions $C(\vec{l})$ and the dimer-dimer correlation functions $D(\vec{l})$ using the FNE method, i.e., $|\psi\rangle = |\psi_0^{\text{eff}}\rangle$ in Eqs. (49) and (50), with the optimized $|p\text{-BCS}\rangle$ for $|\psi_G\rangle$ in $\hat{H}^{\text{eff}}$. Here $|\psi_0^{\text{eff}}\rangle$ is the exact ground state of $\hat{H}^{\text{eff}}$ calculated numerically. The typical results for $C(\vec{l})$ and $D(\vec{l})$ are presented in Figs. 7 and 9, respectively. By comparing the variational results with the FNE ones, it is evident that these correlation functions appear almost unchanged even at large distances, strongly suggesting that the projected BCS state $|p\text{-BCS}\rangle$ is very stable and accurate. This should be contrasted to the isotropic case (see. Fig. 15), which will be discussed in the next subsection.

A systematic finite size scaling analysis of the order parameters $P_s = C(l_{\max}\vec{\tau}_1)$ and P_d^2 calculated using FNE is also reported in Fig. 8 for $J'/J = 0.33$ and L up to 30×30. It is clearly seen in Fig. 8(b) that P_d^2 diminishes to zero in the limit $L \to \infty$. Even though the FNE results for P_s shown in Fig. 8(a) are almost the same as the ones for the variational calculations with $|p\text{-BCS}\rangle$, it is still difficult to rule out completely the possibility of a very small nonzero magnetic order parameter $P_s \lesssim 0.001$ in the thermodynamic limit. Nevertheless, the fact that the spin-spin correlation functions calculated for $L \lesssim 1000$ using the variational wave function $|p\text{-BCS}\rangle$ are almost identical to the ones calculated using the more accurate FNE approach (Fig. 7), strongly suggests that the magnetic long range order is not likely to occur even for the more accurate FNE ground state $|\psi_0^{\text{eff}}\rangle$. From these results, we conclude that the ground state of the spin-1/2 antiferromagnetic Heisenberg model on the triangular lattice with $J'/J \lesssim 0.6$–0.7 (see also Sec. IV) is a spin liquid state with gapless spin excitations at the incommensurate momenta, described at least approximately by the present projected BCS wave function $|p\text{-BCS}\rangle$.

Finally, let us discuss the implication of our numerical study on the experiments for Cs_2CuCl_4 where the estimated coupling is $J'/J \simeq 1/3$.[11] Recent inelastic neutron scattering experiments for this material by Coldea et al.[11] have revealed that the lowest spin excitation appears at an incommensurate momentum (see Fig. 10), and the observed excitation spectrum consists of a broad incoherent continuum, at least, in the intermediate temperature region above the magnetic transition temperature T_N. As we have shown in the case of the 1D system (Sec. III B), the BCS elementary excitations naturally define true spinons in our approach, and according to the gauge theory[48,54] they should behave as free fermions at
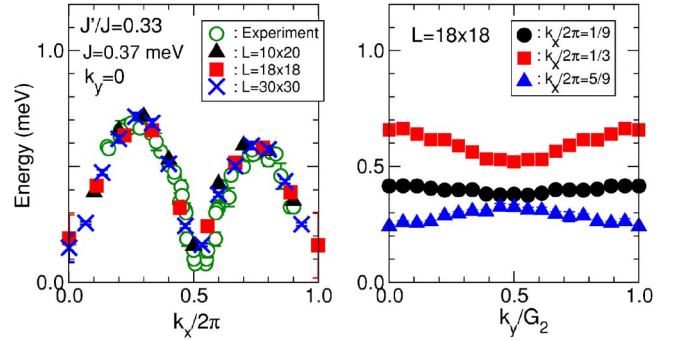

FIG. 10. (Color online) Lowest triplet excitation energy as a function of momentum for $J'/J = 0.33$ and different cluster sizes L (indicated in the figures), calculated using the method introduced in Sec. II D. For comparison, the experimental values (open circles) measured by inelastic neutron scattering on Cs_2CuCl_4 (Ref. 11) are also plotted. Here $G_2 = 4\pi/\sqrt{3}$, and the experimentally estimated value of $J = 0.37$ meV is used (Ref. 11).

low enough energy, namely, close to the nodal points of the incommensurate momenta where $\xi_k = \Delta_k = 0$ (see Fig. 5). Therefore, the low energy spin excitations observed experimentally can be explained by a two-spinon broad continuum. At present, we cannot calculate directly the dynamical spin correlation functions. However, using the technique described in Sec. II D, we can calculate the lowest spin-1 excitation energy at each momentum, and in Fig. 10 our results are compared with the experimental values estimated for Cs_2CuCl_4 by Coldea et al.[11] As seen in Fig. 10, both results are in excellent agreement, considering that our calculated excitation spectra with L up to 30×30 appear rather well converged to the thermodynamic limit. This remarkable agreement strongly supports the presence of a spin liquid state in 2D.

D. Isotropic triangular lattice with $J' = J$

It is well known[3] that for the spin-1/2 antiferromagnet Heisenberg model on the spatially isotropic triangular lattice $(J' = J)$, a faithful variational ansatz is the so-called short range RVB state $|\psi_{\text{RVB}}\rangle$ described by the following wave function:

$$|\psi_{\text{RVB}}\rangle = \sum_{\{C\}} \left[\prod_{\substack{i,j=1 \\ (i<j)}}^{L} |[i,j]\rangle \right], \qquad (51)$$

where the sum $\{C\}$ runs over all possible nearest neighbor dimer covering of the triangular lattice (with equal weights and therefore implying that all the spatial symmetries of the lattice are satisfied), whereas the product is over the corresponding nearest neighbor singlet pairs of spins located on each dimer (defining singlet valence bond configurations for a given dimer covering) between sites i and j,

$$|[i,j]\rangle = \frac{1}{\sqrt{2}}(\uparrow_i \downarrow_j - \downarrow_i \uparrow_j), \qquad (52)$$

sorted according to the lexicographic order $(i < j)$.

Indeed, very recent numerical calculations for the 6×6 isotropic triangular antiferromagnet by the Lanczos method[21] have shown that the overlap between the short range RVB wave function $|\psi_{RVB}\rangle$ and the exact ground state $|\Psi_0\rangle$ is very large $|\langle\psi_{RVB}|\Psi_0\rangle|^2 = 0.891,$[55] and especially the average sign

$$\langle S \rangle = \sum_x |\langle x|\Psi_0\rangle|^2 \, \text{sgn}[\langle x|\Psi_0\rangle\langle x|\psi_{RVB}\rangle], \quad (53)$$

is very close to the maximum value, namely, $\langle S \rangle = 0.971$. These results clearly indicate that the phases of the exact ground state $|\Psi_0\rangle$ are very well described by the short range RVB ansatz state $|\psi_{RVB}\rangle$. The values of the overlap $|\langle\psi_{RVB}|\Psi_0\rangle|^2$ and the average sign $\langle S \rangle$ are even much better than the ones corresponding to classical Néel ordered wave functions considered previously, which also contain additional variational parameters.[4] It should be emphasized that an accurate description of the phases of the exact ground state $|\Psi_0\rangle$ by a simple variational wave function such as $|\psi_{RVB}\rangle$ is the essential ingredient for reliable calculations based on the FN or FNE approach.

Although $|\psi_{RVB}\rangle$ is a very good variational ansatz for the ground state of the isotropic triangular antiferromagnet, the above representation of this state [Eq. (51)] is rather difficult to handle and is not convenient to improve the state $|\psi_{RVB}\rangle$ systematically by including, for instance, long-range valence bonds, because, within this representation, there is a "sign problem" even at the variational level.[3] In order to treat more conveniently the short range RVB wave function $|\psi_{RVB}\rangle$ and its variants, we have derived in Appendix D an exact mapping between the short range RVB wave function $|\psi_{RVB}\rangle$ and the projected BCS state $|p\text{-BCS}\rangle$ on planar graphs,[56] namely, for most interesting lattice geometries including the triangular lattice, the square lattice, and the kagomé lattice.

As shown in Appendixes C and D, the short range RVB state $|\psi_{RVB}\rangle$ is equivalently described by the projected BCS wave function $|p\text{-BCS}\rangle$ with a special choice of the variational parameters: the only nonzero parameters are the chemical potential μ and the nearest neighbor singlet gap functions $\Delta_{i,j}$ with the appropriate relative phases shown in Fig. 11, and the limit of $-\mu \gg |\Delta_{i,j}|$ is assumed so that the gap function $\Delta_{i,j}$ is proportional to the pairing function $f_{i,j}$ [Eqs. (C10)] considered in Appendix D.

It is easily seen from Fig. 11 that the corresponding BCS Hamiltonian $\hat{H}_{BCS}$ is defined on a (2×1) unit cell, and thus $\hat{H}_{BCS}$ is not translation invariant. In fact, $\hat{H}_{BCS}$ is invariant under an elementary translation $\mathcal{T}_2 : \vec{r} \to \vec{r} + \vec{\tau}_2$ in the $\vec{\tau}_2$ direction, whereas it is not under an elementary translation $\mathcal{T}_1 : \vec{r} \to \vec{r} + \vec{\tau}_1$ in the $\vec{\tau}_1$ direction. Let us now show briefly that the translation symmetry is recovered after the projection $\mathcal{P}_G$, i.e., $|p\text{-BCS}\rangle$ is indeed translation invariant. To this end, one can combine the translation operation $\mathcal{T}_1$ with the SU(2) gauge transformation $\mathcal{U}$:

$$c_{\vec{r},\sigma}^\dagger \to -c_{\vec{r},\sigma}^\dagger \quad (54)$$

for $\vec{r} = r_1\vec{\tau}_1 + r_2\vec{\tau}_2$ with r_2 *odd*. Under the composite application of the transformations $\mathcal{T}_1 \otimes \mathcal{U}$, the projected BCS wave function $|p\text{-BCS}\rangle$ remains unchanged. Therefore, the $|p\text{-BCS}\rangle$ is translation invariant because the SU(2) gauge
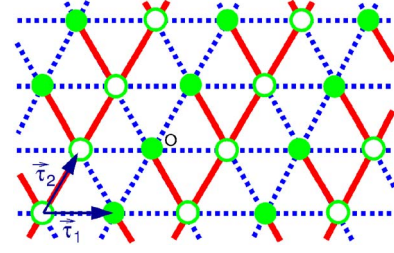

FIG. 11. (Color online) Nearest neighbor gap functions $\Delta(\vec{\tau}_1) = \Delta(\vec{\tau}_2) = \Delta(\vec{\tau}_2 - \vec{\tau}_1) = \Delta$ [Eq. (55)], which are consistent with the sign convention for the short range RVB state explained in Appendix D. The dashed (solid) bonds represent a positive (negative) sign [Eqs. (D8) and (D9)]. Notice that the unit cell is (2×1). The origin of the lattice $(0,0)$ [Eq. (55)] is denoted by O.

transformation $\mathcal{U}$ acts as an identity in the physical Hilbert space with singly occupied sites due to the projection $\mathcal{P}_G$.

Owing to this new, more convenient representation of the short range RVB state $|\psi_{RVB}\rangle$ by the projected BCS wave function $|p\text{-BCS}\rangle$, we can now calculate various physical quantities using the standard variational Monte Carlo method. For example, the variational energy $E(\psi_{RVB})$ of the isotropic triangular antiferromagnet is plotted in Fig. 12 for different system sizes. From the finite size scaling analysis of lattice sizes up to $L = 30 \times 30$, we can easily provide a very accurate estimate of the variational energy in the thermodynamic limit $E(\psi_{RVB})/JL = -0.5123 \pm 0.0001$ for $L \to \infty$ (see also Table II).

Another important advantage of this projected BCS wave function representation is that it is easy to improve the variational ansatz state systematically. For instance, only by changing the chemical potential μ from a large value to zero, the variational energy is significantly improved as is shown in Fig. 12 and in Table II, where the variational state is denoted simply by $|\psi_{RVB}\rangle$ with $\mu = 0$. Note that in this case the $|p\text{-BCS}\rangle$ is equivalent to a Gutzwiller projected free fermion state with nearest neighbor hoppings defined in a (2×1) unit cell.[57,58]

More generally, within the framework of the projected BCS wave function $|p\text{-BCS}\rangle$, we can easily extend the varia-
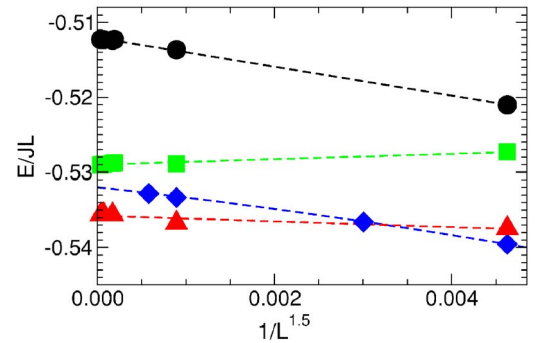

FIG. 12. (Color online) Variational energy for the isotropic triangular lattice with $J'/J = 1.0$ calculated using the short-range RVB state $|\Psi_{RVB}\rangle$ (circles), the short-range RVB state with $\mu = 0$ (squares), the classical Néel state $|\Psi_{Néel}\rangle$ (diamonds) (Ref. 4), and the present projected BCS state $\mathcal{J}_s|p\text{-BCS}\rangle$ with spin Jastrow factor $\mathcal{J}_s$ (triangles).

TABLE II. The energy E and the magnetic moment m (divided by its maximum value $m_0=1/2$) estimated in the thermodynamic limit for the spin-1/2 antiferromagnetic Heisenberg model on the isotropic triangular lattice ($J=J'$). In the first four rows are the variational Monte Carlo (VMC) estimates for different wave functions: (from the top) the short-range RVB state $|\psi_{\text{RVB}}\rangle$, $|\psi_{\text{RVB}}\rangle$ with $\mu=0$ (see the text), the wave function studied recently by Weber *et al.* (Ref. 60) in which a classical Néel order and a singlet pairing (with symmetry different from ours) are included, and the present wave function $\mathcal{J}_s|p\text{-BCS}\rangle$. The fixed node (FN) and effective Hamiltonian (FNE) results are then provided. For comparison, the corresponding values estimated by the linear spin wave (SW) theory and the Green function Monte Carlo method with stochastic reconfiguration (GFMCSR) (Ref. 4) are also presented. Note that the energies computed by the last two methods (denoted by an asterisk) are not a rigorous upper bound of the exact ground state energy.

Method (wave function)	E/JL	m/m_0
VMC (RVB)	-0.5123 ± 0.0001	0.0
VMC (RVB with $\mu=0$)	-0.5291 ± 0.0001	0.0
VMC (BCS+Néel) (Ref. 60)	-0.532 ± 0.001	0.72
VMC (present study)	-0.5357 ± 0.0001	0.0
FN	-0.53989 ± 0.00003	0.325 ± 0.006
FNE	-0.54187 ± 0.00006	0.353 ± 0.007
SW	$-0.538\pm0.002^*$	0.4774
GFMCSR (Ref. 4)	$-0.545\pm0.002^*$	0.41 ± 0.02

tional ansatz state to include long-range singlet valence bonds simply by adding nonzero gap functions $\Delta_{i,j}$'s to the BCS Hamiltonian $\hat{H}_{\text{BCS}}$.[59] In order for $|p\text{-BCS}\rangle$ to preserve translation invariance, the pairing part of the BCS Hamiltonian is generalized in the following form:

$$\hat{H}_{\text{pair}} = \sum_{\vec{r}} \left[\sum_{\vec{t}_m}' (-1)^{r_1 m_2} \Delta(\vec{t}_m)(c_{\vec{r}\uparrow}^\dagger c_{\vec{r}+\vec{t}_m\downarrow}^\dagger - c_{\vec{r}\downarrow}^\dagger c_{\vec{r}+\vec{t}_m\uparrow}^\dagger) + \text{H.c.} \right], \tag{55}$$

where the first sum runs over all lattice vectors $\vec{r}=r_1\vec{\tau}_1+r_2\vec{\tau}_2$ (r_1, r_2: integer), whereas the second sum $\Sigma'_{\vec{t}_m}$ is for $\vec{t}_m = m_1\vec{\tau}_1 + m_2\vec{\tau}_2$ (m_1, m_2: integer) with $m_2>0$ or with $m_1>0$ and $m_2=0$ denoted by solid circles in Fig. 24(a). It is readily shown that $\hat{H}_{\text{pair}}$ is invariant under $\mathcal{T}_1\otimes\mathcal{U}$ and $\mathcal{T}_2$. In order to minimize the number of variational parameters, we have assumed here that $\Delta(\vec{t}_m)=\Delta(\mathcal{R}_y\vec{t}_m)$. Because of the phases of the gap functions in $\hat{H}_{\text{pair}}$ (see Fig. 11 for the nearest neighbor gap functions), this BCS Hamiltonian is not guaranteed to be reflection invariant around the yz plain (R_y). Nevertheless, as will be discussed later, our numerical calculations indicate empirically that the considered projected BCS state $|p\text{-BCS}\rangle$ becomes a fully symmetric spin liquid state only in the thermodynamic limit, a state being not only translation invariant but also reflection invariant. It is interesting to notice that even though this $|p\text{-BCS}\rangle$ is not fully symmetric on small lattice sizes such as a 6×6 cluster, a much better overlap $|\langle p\text{-BCS}|\Psi_0\rangle|^2$ as well as a much better average sign $\langle S\rangle$
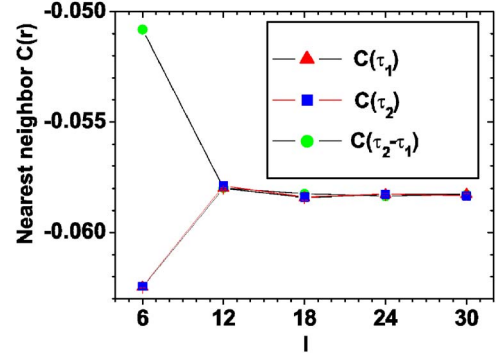

FIG. 13. (Color online) System size dependence of the nearest neighbor spin-spin correlation functions $C(\vec{r})$ [Eq. (49)] for different cluster sizes $L=l\times l$ up to 30×30 sites and for the three different directions of the triangular lattice ($\vec{r}=\vec{\tau}_1$, $\vec{\tau}_2$, and $\vec{\tau}_2-\vec{\tau}_1$). Here $|\psi\rangle=|p\text{-BCS}\rangle$ with $\Delta(\vec{\tau}_1)=\Delta(\vec{\tau}_2)=\Delta(\vec{\tau}_2-\vec{\tau}_1)=1$ [see in Fig. 11 and Eq. (55)], $t_{i,j}=0$, and $\mu=-1$. This state is a good but not optimal variational wave function for the spatially isotropic model ($J=J'$), and it is used only to show that wave functions of this type recover all spatial symmetries of the lattice in the thermodynamic limit.

are obtained for this $|p\text{-BCS}\rangle$ compared to the ones for a translation invariant complex $|p\text{-BCS}\rangle$ ansatz.[19,20] In Appendix C, several peculiar and interesting properties of the corresponding unprojected BCS state $|\text{BCS}\rangle$ are derived analytically. For example, the spectrum of the BCS Hamiltonian $E_{\mathbf{k}}$ has two branches [due to the (2×1) unit cell] and a small excitation gap, which vanishes when the long range gap functions are turned off (provided $\mu=0$).

As mentioned above, it is extremely important to show that the projected BCS state $|p\text{-BCS}\rangle$, constructed from $|\text{BCS}\rangle$ with the pairing interactions $\hat{H}_{\text{pair}}$, preserve all reflection symmetries of the lattice in the thermodynamic limit, because otherwise some symmetry broken with finite order parameter occurs, and this variational state is no longer a spin liquid. This symmetry property is easily proved for the short range RVB case. Within open boundary conditions, the short range RVB state $|\psi_{\text{RVB}}\rangle$ [Eq. (51)] and the projected BCS state $|p\text{-BCS}\rangle$ with the gap functions defined as in Fig. 11, $t_{i,j}=0$, and $\mu\to-\infty$ are exactly the same for any finite size clusters (see Appendix D). Therefore the symmetry of the state $|p\text{-BCS}\rangle$ is implied by the one of the short range RVB state $|\psi_{\text{RVB}}\rangle$. For large clusters the boundary conditions cannot play a role, and hence the symmetry is approximately recovered even when periodic boundary conditions are used. We have checked numerically in Fig. 13 that the reflection symmetry is very well preserved in the thermodynamic limit also for the general case where the pairing function $f_{i,j}$ is not restricted only to nearest neighbor bonds. However, in this case we could not rigorously prove our empirical observation of this symmetry invariance because the equivalence of RVB wave functions and $|p\text{-BCS}\rangle$ no longer holds for long range pairing functions.

In order to further improve our variational ansatz wave function, we also introduce a simple spin Jastrow factor $\mathcal{J}_s$ into the projected BCS wave function described above, i.e., $|p\text{-BCS}\rangle\to\mathcal{J}_S|p\text{-BCS}\rangle$, where

$$\mathcal{J}_S = \exp\left[\sum_{\substack{i,j=1 \\ (i<j)}}^{L} v(\vec{r}_i - \vec{r}_j)\hat{S}_i^z\hat{S}_j^z\right] \tag{56}$$

and $v(\vec{r})$'s are variational parameters which are optimized using the SR method explained in Sec. II B (also see in Appendix A). Since the most important contributions to the variational energy are from the short range $v(\vec{r})$'s, in what follows we consider only terms with $|\vec{r}|<3$ and the $v(\vec{r})$'s for larger distances are set identically to zero. As will be discussed later, the inclusion of the spin Jastrow factor $\mathcal{J}_s$ is also crucial for stable FN and FNE calculations. Similarly, for the gap functions, only $\Delta(\vec{t}_m)$'s with $|\vec{t}_m|<3$ are considered in the present variational wave function. After the SR optimization calculations, it is found that the optimized chemical potential μ is nonzero and only nearest neighbor hopping terms with $t_{i,j}=1$ for all the directions are relevant for the isotropic case $(J=J')$. In Fig. 12 and in Table II, the calculated variational energy is reported and compared with the results for other variational ansatz states. The improvement of the present variational wave function compared with previously studied states is remarkable. Our variational energy is even sizably better than a very recent estimate reported in Ref. 60, in which a variational ansatz state includes both a classical Néel ordered magnetic moment and a singlet pairing with symmetry different from ours. To our knowledge, the present value for the energy per site in the thermodynamic limit $-0.5357J\pm0.0001J$ is the lowest among the variational estimates reported so far. Of course, within the present ansatz, this value can be further improved by considering longer range terms in $v(\vec{r})$'s and $\Delta(\vec{t}_m)$'s.

It is worth mentioning here that in general the BCS excitation spectrum $E_{\mathbf{k}}$ [Eq. (C6)] has a finite gap when the longer range gap functions are included in the BCS Hamiltonian as in the present case, and therefore, as opposed to the spin liquid state discussed in Sec. III C, the spin liquid state described here by $|p\text{-BCS}\rangle$ generally shows a finite gap in spin excitations. It should be also noted that, although the variational ansatz state with the spin Jastrow factor $\mathcal{J}_s$ breaks the SU(2) spin rotation symmetry, a short range $\mathcal{J}_s$ cannot imply long range magnetic order. This is clearly seen in Fig. 14 where the spin structure factor

$$S(\vec{q}) = \sum_{\vec{r}} e^{-i\vec{q}\cdot\vec{r}}C(\vec{r})$$

at $\vec{q}=(4\pi/3,0)$ is calculated for the optimized variational wave function mentioned above.

Although the projected BCS wave function considered here is a spin liquid state with a finite spin gap and without any type of long range magnetic order (Fig. 14), when the FN or FNE method is applied with $|\psi_G\rangle=\mathcal{J}_s|p\text{-BCS}\rangle$, long range magnetic order appears with a finite magnetic moment in the z direction (the effective Hamiltonian approach breaks the spin rotational invariance in this case and no detectable magnetic moment is observed in the other directions). Indeed, as shown in Fig. 15, the spin-spin correlation functions $C(\vec{r})$ along the $\vec{\tau}_1$ direction are drastically increased for the FNE ground state $|\psi_0^{\text{eff}}\rangle$, compared with the ones for the spin
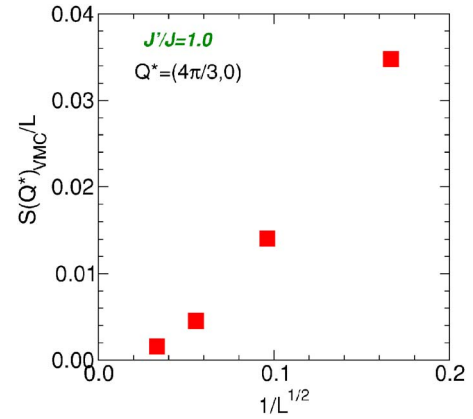

FIG. 14. (Color online) System size dependence of spin structure factor $S(\vec{q})$ at $\vec{q}=\mathbf{Q}^*=(4\pi/3,0)$ for the optimized variational state $\mathcal{J}_s|p\text{-BCS}\rangle$ (see the text) for the spin-1/2 antiferromagnetic Heisenberg model on the isotropic triangular lattice of size L. Note that $\mathbf{Q}^*$ corresponds to the momentum at which $S(\mathbf{Q}^*)/L$ is finite for $L\to\infty$ when the state is classical Néel ordered with relative angle of $120°$ between the nearest neighbor spins on the different sublattices.

liquid state $\mathcal{J}_s|p\text{-BCS}\rangle$. Furthermore, the oscillations observed in $C(\vec{r})$ for the FNE ground state (Fig. 15) are consistent with the classical Néel order. These results strongly indicate that, in spite of its good variational energy, the spin liquid state is not stable against magnetic order for the isotropic case.

The FN and FNE calculations of the spin-spin correlation functions were carried out by applying the "forward walking" technique developed in Ref. 33, which will be described briefly in the following. With this technique, the expectation value of any operator $\hat{O}$ diagonal in configuration space $\{x\}$, can be computed for the ground state of the effective Hamil-
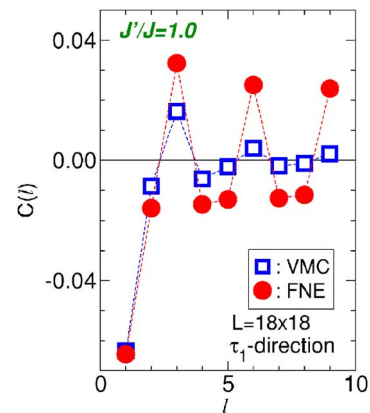

FIG. 15. (Color online) Spin-spin correlation functions $C(l\vec{\tau}_1)$ in the $\vec{\tau}_1$ direction for the spin-1/2 antiferromagnetic Heisenberg model on the isotropic triangular lattice with $L=18\times18$ calculated using both variational Monte Carlo (VMC) and effective Hamiltonian (FNE) methods. The variational wave function considered here is the projected BCS state $\mathcal{J}_s|p\text{-BCS}\rangle$ with spin Jastrow factor $\mathcal{J}_s$ (see the text), and this wave function is used as the guiding function $|\psi_G\rangle$ for the FNE calculation. The spin-spin correlation functions in the $\vec{\tau}_2$ and $\vec{\tau}_2-\vec{\tau}_1$ directions are essentially the same as the ones presented here.
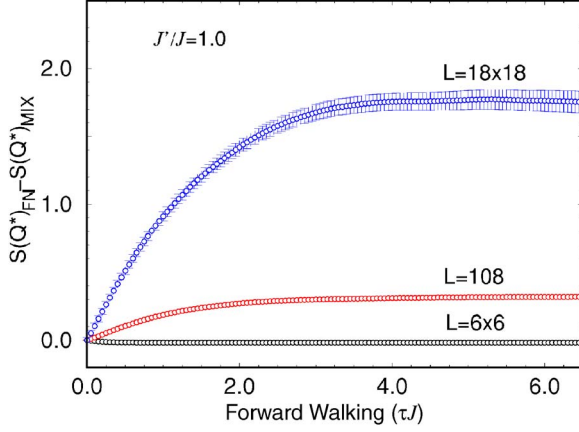
FIG. 16. (Color online) Forward walking time evolution τ (unit J^{-1}) [Eq. (57)] of the spin structure factor $S(\vec{q})$ at $\vec{q}=\mathbf{Q}^* =(4\pi/3,0)$ for $J'/J=1.0$. Here our best variational wave function $|p\text{-BCS}\rangle$ with spin Jastrow factor $\mathcal{J}_s$ (see the text) is used as the guiding function $|\psi_G\rangle$. For clarity, for each cluster, the FN results $S(\mathbf{Q}^*)_{\text{FN}}$ are referenced to the mixed-average estimate $S(\mathbf{Q}^*)_{\text{mix}}$, which is set to zero.

tonian. This scheme removes completely the bias of the so-called mixed average estimate[61]

$$O_{\text{mix}} = \frac{\langle \psi_G|\hat{O}|\psi_0^{\text{eff}}\rangle}{\langle \psi_G|\psi_0^{\text{eff}}\rangle},$$

by a large "forward-walking" time τ projection of the guiding function $|\psi_G\rangle$ in the above expression. More precisely, the expectation value of $\hat{O}$ for the state $|\psi_0^{\text{eff}}\rangle$ is computed through the equation

$$\frac{\langle \psi_0^{\text{eff}}|\hat{O}|\psi_0^{\text{eff}}\rangle}{\langle \psi_0^{\text{eff}}|\psi_0^{\text{eff}}\rangle} = \lim_{\tau\to\infty} \frac{\langle \psi_G|e^{-\tau\hat{H}_{\text{eff}}}\hat{O}|\psi_0^{\text{eff}}\rangle}{\langle \psi_G|e^{-\tau\hat{H}_{\text{eff}}}|\psi_0^{\text{eff}}\rangle}, \quad (57)$$

where the simple relation $\lim_{\tau\to\infty} e^{-\tau\hat{H}_{\text{eff}}}|\psi_G\rangle \propto |\psi_0^{\text{eff}}\rangle$ is used. This scheme provides for a quantitative estimate of the magnetic moment (order parameter), as shown in Fig. 16, where one can clearly see that the values of the spin structure factor $S(\vec{q})$ at the commensurate wave vector $\vec{q}=\mathbf{Q}^*=(4/3\pi,0)$ considerably increase with cluster sizes and with the forward-walking projection time τ, the $\tau=0$ value corresponding to the much less accurate mixed average estimate. In this figure, it is also apparent that a satisfactory convergence in τ [Eq. (57)] is always obtained for the clusters studied. From the technical point of view, this calculation was made possible due to the quality of our variational ansatz. For instance, without the inclusion of the spin Jastrow factor $\mathcal{J}_s$ a much longer forward-walking time τ is necessary to achieve a reasonable convergence, with an almost prohibitive computational effort to reduce the statistical errors to an acceptable value.

Encouraged by these results, let us finally study the system size dependence of the spin structure factor $S(\vec{q})$ at the commensurate wave vector $\vec{q}=\mathbf{Q}^*$. The results calculated using both FN and FNE methods, $S(\mathbf{Q}^*)_{\text{FN}}$ and $S(\mathbf{Q}^*)_{\text{FNE}}$, are presented in Fig. 17. For each cluster, the FN and FNE
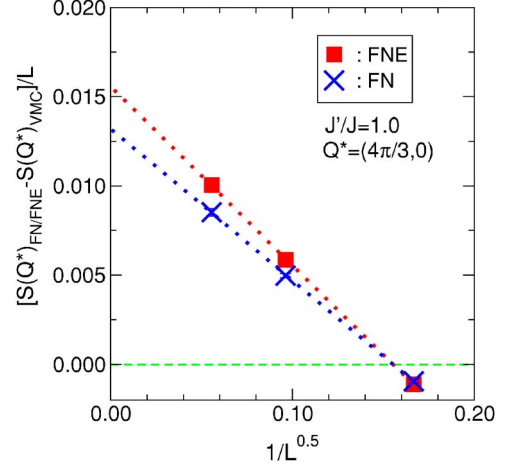

FIG. 17. (Color online) System size dependence of the spin structure factor $S(\vec{q})$ at $\vec{q}=\mathbf{Q}^*=(4\pi/3,0)$ for the spin-1/2 isotropic triangular antiferromagnet with $J'/J=1.0$ calculated using FN and FNE methods. Here our best variational wave function $\mathcal{J}_s|p\text{-BCS}\rangle$ with spin Jastrow factor $\mathcal{J}_s$ (see the text) is used as the guiding function $|\psi_G\rangle$. In order to reduce finite size effects, for each cluster, the variational result $S(\mathbf{Q}^*)_{\text{VMC}}/L$ for the spin liquid state $\mathcal{J}_s|p\text{-BCS}\rangle$ (which is zero for $L\to\infty$) is subtracted from the FN and FNE results $S(\mathbf{Q}^*)_{\text{FN/FNE}}/L$.

Hamiltonians are constructed using the optimized variational state $\mathcal{J}_s|p\text{-BCS}\rangle$ as the guiding function $|\psi_G\rangle$. In this figure, to reduce the finite size effects for estimating the magnetic order parameter, the difference between the FN/FNE results $S(\mathbf{Q}^*)_{\text{FN/FNE}}$ and the corresponding variational estimates $S(\mathbf{Q}^*)_{\text{VMC}}$ are plotted. The difference should be extensive if there exists long range antiferromagnetic order, as the variational results $S(\mathbf{Q}^*)_{\text{VMC}}/L$ for the spin liquid state $\mathcal{J}_s|p\text{-BCS}\rangle$ decreases to zero in the limit $L\to\infty$ (Fig. 14). It is clearly observed in Fig. 17 that the FN and FNE results for $S(\mathbf{Q}^*)/L$ converge to finite values in the thermodynamic limit.

From these calculations we can estimate the magnetic moment quantitatively. To this purpose, it has to be taken into account that the long range magnetic order occurs in the z direction because the FN Hamiltonian $\hat{H}^{\text{FN}}$ and the FNE Hamiltonian $\hat{H}^{\text{eff}}$ do not commute with the total spin operator and display magnetic order only in the z direction.[62] Therefore, the magnetic structure factor is related to the magnetic order parameter (magnetic moment) m up to a simple factor, namely, $S(\mathbf{Q}^*)_{\text{FN/FNE}}/L\to m^2/2$. Our estimates of m are summarized in Table II along with the ones of the energy E_0^{FN} and E_0^{eff} in the thermodynamic limit. For comparison, the estimates calculated by other methods and for different wave functions are also provided in Table II. It is remarkable that even though a spin liquid wave function is used here as a guiding wave function, a finite magnetic moment m is obtained with the FN and FNE approaches. These results clearly indicate that the spin liquid is eventually unstable in the isotropic model. It should be noted here that the magnetic moment estimated with approximate techniques such as the FN and FNE methods should be considered a lower bound because they are biased toward nonmagnetic order by the spin liquid guiding function.

It is also important to notice in Fig. 17 and in Table II that the FNE approach, which is a better variational method than the standard FN method, provides a sizably larger value of m compared with the FN result, much closer to previous estimates based on different guiding functions with explicit magnetic order.[4] In the previous work,[4] though the energy was not rigorously variational unlike in the present case, similar corrections to the guiding function were implemented.[63] It is therefore very interesting that, by using two different variational wave functions with (overestimated) or without (strongly underestimated) magnetic order, both with good variational energy, and by applying very similar techniques, a finite order parameter m for the isotropic triangular lattice is obtained, rather independently of the guiding function used. This is a very important property of methods, such as FN, FNE, and the previously introduced Green function Monte Carlo method with stochastic reconfiguration,[4] which are all based on the numerical solution of an effective Hamiltonian. On the contrary, the simple variational approach does not lead to a reliable prediction for the magnetic moment m simply because very different variational ansatz states with or without a finite magnetic moment may have very similar energy (see, e.g., Fig. 12 and Table II) but opposite long distance behavior. This is an additional confirmation that the present approach, a systematic correction to the variational ansatz, is very useful for understanding quantitative physical properties of strongly frustrated quantum systems, for which either numerically or analytically exact solutions are not known.

E. Nearly isotropic triangular lattice with $J' \lesssim J$: A spin liquid with a small spin gap

In the previous subsection, we have shown a robust numerical evidence that a spin liquid state is not the ground state for the isotropic triangular antiferromagnet. However, it is natural to expect that quantum fluctuations become enhanced by increasing the spatial anisotropy $J/J' > 1$, and that the magnetically ordered state eventually melts and a true spin liquid phase would emerge. In this subsection, we shall extend the spin liquid ansatz wave function discussed above away from the isotropic point, and study the stability of the spin liquid state with the FN or FNE method, as it was done successfully in the isotropic case.[64]

1. Stability against magnetic ordering

As reported in previous studies,[5] a simple semiclassical solution implies that the spin structure factor $S(\vec{q})$ displays Bragg peaks at incommensurate momenta even slightly away from the isotropic case with $J'/J \neq 1$. It is confirmed by our variational approach, which provides a much better variational state compared to the classical solution, that these peaks appear in $S(\vec{q})$ and their locations in the Brillouin zone smoothly evolve from the commensurate momenta $\mathbf{Q}^* = (4\pi/3, 0)$ (and equivalent ones) to the incommensurate ones within our accessible finite size clusters.

At the variational level with the same type of spin liquid wave functions considered for the isotropic case (see also Table III), the spin structure factor is finite for these incom-

TABLE III. The optimized variational parameters of the projected BCS wave function for $J'/J=0.7$ and 0.8 with $L=18 \times 18$. $\Delta(m_1, m_2)$ is the singlet gap function $\Delta(\vec{t}_m)$ for $\vec{t}_m = m_1 \vec{\tau}_1 + m_2 \vec{\tau}_2$ in Eq. (55), and μ is the chemical potential. The remaining variational parameters are zero except for the nearest neighbor hopping in the $\vec{\tau}_1$ direction, which is chosen to be one. The value of K, variational energy $E_{VMC}=E(p\text{-BCS})$, FN (FNE) ground state energy $E_{FN} = E_0^{FN}$ ($E_{FNE}=E_0^{eff}$) with $|\psi_G\rangle = |p\text{-BCS}\rangle$ are also presented. The number in parentheses is the statistical error bar corresponding to the last digit of the figure.

J'/J	0.7	0.8
μ	0.304(3)	0.243(6)
$\Delta(1,0)$	2.01(3)	2.33(4)
$\Delta(0,1)$	1.08(2)	1.42(2)
$\Delta(1,1)$	0.205(3)	0.215(3)
$\Delta(-1,2)$	0.002(3)	0.001(3)
$\Delta(2,0)$	−0.36(1)	−0.32(2)
$\Delta(0,2)$	0.01(1)	−0.02(3)
$\Delta(2,1)$	0.011(2)	0.063(2)
$\Delta(1,2)$	0.002(2)	0.001(2)
$\Delta(-2,3)$	0.001(1)	0.0008(9)
K^{-1}	1.1886(3)	1.2242(3)
E_{VMC}/JL	−0.46467(3)	−0.47840(3)
E_{FN}/JL	−0.47051(2)	−0.48521(2)
E_{FNE}/JL	−0.47171(3)	−0.48691(4)

mensurate peaks, and therefore, as opposed to the classical solution, no long range magnetic order is implied. To study this property within the FN or FNE approach, we have to first note that it is very difficult to perform a finite size scaling analysis when incommensurate correlations are studied, a situation which is further complicated by the proximity to a possible phase transition from a magnetic to a nonmagnetic ground state, because the value of m, as we have shown, is rather small already in the isotropic case. In order to carry out a reliable finite size scaling, in the following, we consider a sizable anisotropy within the hypothesis to be far enough from the critical point (which is unaccessible within the finite size clusters studied, $L \lesssim 1000$). Indeed, for $J'/J = 0.7$, we are able to successfully carry out the analysis of the FNE calculations, and the results are presented in Fig. 18. Here the guiding wave function $|p\text{-BCS}\rangle$ does not require the spin Jastrow factor $\mathcal{J}_s$ to be accurate enough, and it consists of $\Delta(\vec{t}_m)$ with $|\vec{t}_m| < 3$ [Eq. (55)] as well as the hopping integrals and the chemical potential. All these parameters are optimized using the SR minimization method. As shown in Table III, it is found that the optimized chemical potential is nonzero, and only the nearest neighbor hopping in the $\vec{\tau}_1$ direction is relevant and can be set to unity ($t_{\vec{\tau}_1}=1$).

The excitation spectrum $E_\mathbf{k}$ of the corresponding BCS Hamiltonian are analytically calculated in Appendix C, from which several very interesting features are observed. If the gap functions $\Delta(\vec{t}_m)$ are restricted to the nearest neighbors,
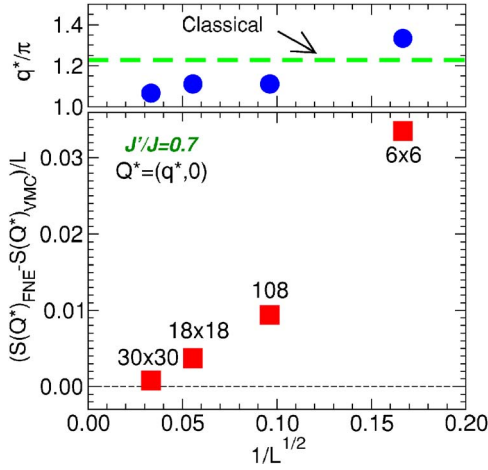
FIG. 18. (Color online) System size dependence of the spin structure factor $S(\vec{q})$ at $\vec{q}=\mathbf{Q}^*=(q^*,0)$ for $J'/J=0.7$ calculated using the FNE method. The incommensurate momenta q^* as well as the corresponding value for the classical limit (Ref. 5) are plotted in the upper panel. For clarity, the variational estimates of the structure factor $S(\mathbf{Q}^*)_{\text{VMC}}$ are subtracted from the FNE results $S(\mathbf{Q}^*)_{\text{FNE}}$. The optimized projected BCS state $|p\text{-BCS}\rangle$ without spin Jastrow factor $\mathcal{J}_s$ (see the text) is used for the variational calculations. The same wave function $|p\text{-BCS}\rangle$ is used as the guiding function $|\psi_G\rangle$ for the FNE calculations. The system sizes used are indicated in the figure.

the spectrum of the BCS Hamiltonian is generically gapless (provided $\mu=0$). Once the gap function is nonzero for longer bonds, a tiny energy gain is obtained, and correspondingly a finite excitation gap in $E_\mathbf{k}$ is opened. However, this gap is very small. In fact, it is found that the low energy BCS spectrum $E_\mathbf{k}$ on finite size is almost indistinguishable from a gapless one, and that the lowest excitation gap in $E_\mathbf{k}$ is estimated as small as $\sim 0.3\%$ of $2W$ for $J'/J=0.7$ where W is the maximum excitation energy of $E_\mathbf{k}$.[65] The reason for the appearance of a finite excitation gap in $E_\mathbf{k}$ is simply understood because the BCS Hamiltonian with broken translation symmetry has two sites per unit cell, and thus the BCS spectrum is in general gapped. It should be emphasized here that, as explained in the previous subsection, after applying the projection $\mathcal{P}_G$ onto the GS $|\text{BCS}\rangle$ of this BCS Hamiltonian, the translation symmetry of the projected BCS state $|p\text{-BCS}\rangle$ is recovered. Therefore, a quite new, remarkable possibility to form a spin liquid state with a finite spin gap[66] and with a single spin per unit cell can be easily established here within the present variational framework *without breaking the translation symmetry*.

Let us now discuss the static magnetic properties for $J'/J=0.7$. As seen in Fig. 18, the finite size scaling analysis of the FNE results for the spin structure factor clearly indicates a vanishing magnetic order parameter. We have also found that the FNE spin structure factors as well as the FNE spin-spin correlation functions do not differ significantly from the ones computed for the variational spin liquid state $|p\text{-BCS}\rangle$ explained above (Table III). This should be contrasted to the isotropic case shown in Sec. III D, where significant differences were observed. These results strongly suggest that the spin liquid ansatz state described here by the projected BCS wave function $|p\text{-BCS}\rangle$ is stable within the

present approach. Therefore, another spin liquid region different from the one discussed in Sec. III C might exist in the anisotropic triangular lattice with J'/J closer to one, the state of which can be described, at least approximately, by this proposed spin liquid wave function.

2. Stability against spontaneous dimerization

Since the BCS Hamiltonian is defined with a (2×1) unit cell [Eq. (55)], it is natural to ask ourselves if a valence bond *solid* (not *liquid*) would be stabilized, which should also exhibit a finite spin excitation gap at the expense of a broken translation symmetry. In order to examine whether the valence bond solid is energetically more favored than the spin liquid state for the present anisotropic antiferromagnetic Heisenberg model, it is sufficient to study the translation symmetry of the optimized projected state because the valence bond solid necessarily breaks this symmetry. This possibility can be easily considered within our approach by using a BCS Hamiltonian that is not invariant under the transformation $\mathcal{T}_1\otimes\mathcal{U}$. In Eq. (55) it is assumed that the gap function $\Delta_{\mathbf{i},\mathbf{j}}$ connecting sites $\mathbf{i}$ and $\mathbf{j}$ depends only on $\mathbf{j}-\mathbf{i}$ up to the sign. To check the possible instability toward the valence bond solid, we have released these constraints for $\Delta_{\mathbf{i},\mathbf{j}}$ but with remaining in the same (2×1) unit cell; for example, $\Delta_{0,\vec{\tau}_1}$ can be different from $\Delta_{\vec{\tau}_1,2\vec{\tau}_1}$, but $\Delta_{0,\vec{\tau}_1}=\Delta_{2\vec{\tau}_1,3\vec{\tau}_1}$. We have then optimized independently the first four $\Delta_{\mathbf{i},\mathbf{j}}$'s at the shortest distances:

$$\Delta_1 = \Delta_{0,\vec{\tau}_1},$$

$$\Delta_2 = \Delta_{\vec{\tau}_1,2\vec{\tau}_1},$$

$$\Delta_3 = \Delta_{0,\vec{\tau}_2},$$

$$\Delta_4 = -\Delta_{\vec{\tau}_1,\vec{\tau}_1+\vec{\tau}_2}, \tag{58}$$

whereas all the other ones are kept fixed at the values obtained assuming the translation invariant ansatz (shown in Table III). Whenever the optimized parameters satisfy $\Delta_1=\Delta_2$ and $\Delta_3=\Delta_4$ within the statistical errors, the projected BCS state is a spin liquid. Otherwise the optimized state is a valence bond solid simply because this state is no longer translation invariant. In order to optimize these variational parameters, we have used the SR minimization method described in Sec. II B. Our results are presented in Fig. 19, where the Monte Carlo evolution of these four parameters are plotted for $J'/J=0.7$ and $L=18\times 18$. It is clearly seen in Fig. 19 that, although the initial values of the parameters are far off form the symmetric condition ($\Delta_1=\Delta_2$ and $\Delta_3=\Delta_4$), after a few hundred SR iterations these parameters converge to the symmetric values (Table III). The inset of Fig. 19 shows the Monte Carlo evolution of the corresponding energy as a function of the SR iterations (each iteration corresponds to a small variational Monte Carlo simulation with fixed variational parameters). After the first few SR iterations the energy appears to be trapped in a metastable state with a broken symmetry solution, but then after one hundred SR iterations the energy eventually converges to a lower value
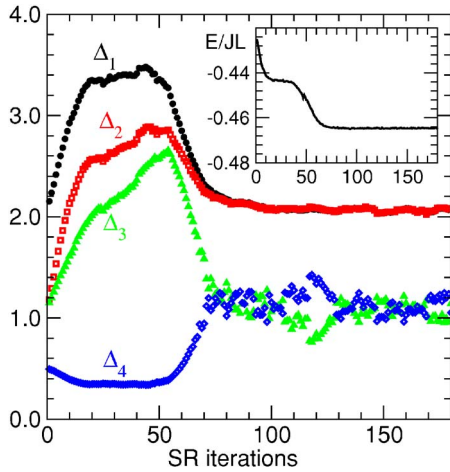
FIG. 19. (Color online) Monte Carlo evolution of the variational parameters defined in Eq. (58) as a function of SR iterations for the spin-1/2 antiferromagnetic Heisenberg model on the anisotropic triangular lattice with $J'/J=0.7$ and $L=18\times18$. Here the SR minimization method explained in Sec. II B is used with $\delta t=0.25/J$ [Eq. (23)]. Inset: the corresponding energy evolution as a function of SR iterations. At each SR iteration, the energy is computed for the wave function with the fixed variational parameters given at the corresponding iteration in the main figure.

corresponding to the spin liquid fully symmetric solution. These results, therefore, strongly indicate that the optimized state is translation invariant, and spontaneous dimerization is very unlikely to occur in this model because it is not stabilized even when the variational ansatz wave function allows to stabilize this kind of order.

In principle, as shown in Ref. 52 for 1D systems, also a translation invariant state can give rise to a spontaneously dimerized order after applying the projection operator $\mathcal{P}_G$ on this state. In order to rule out this possible order, we have also calculated explicitly the dimer-dimer correlation functions $D(\vec{r})$ defined in Eq. (50) for the variational wave function described above (see also Table III). The results are compared with the ones computed using the FNE method. A typical example of the results is presented in Fig. 20 for $J'/J=0.7$ and $L=30\times30$.[67] As seen in Fig. 20, the two results do not show significant differences, confirming that the spin liquid variational ansatz appears very stable in this case. It should be emphasized once again that the situation is very different from the isotropic case where a magnetic instability was clearly detected with the FNE method (Sec. III D).

The numerical calculations presented here strongly suggest that a new type of spin liquid discussed here is an appropriate ground state description of the spin-1/2 antiferromagnetic Heisenberg model on the anisotropic triangular lattice, at least in the region around $J'/J\approx0.7-0.8$ (also see Sec. IV). In the present work, we have not attempted to determine the critical value of J' above which the incommensurate magnetically ordered state is stable, which was previously suggested in, e.g., Ref. 5. Indeed, there exists another more interesting phase boundary between the two possible spin liquid states, the one presented here and the one considered in Sec. III C, which will be discussed in the next section.
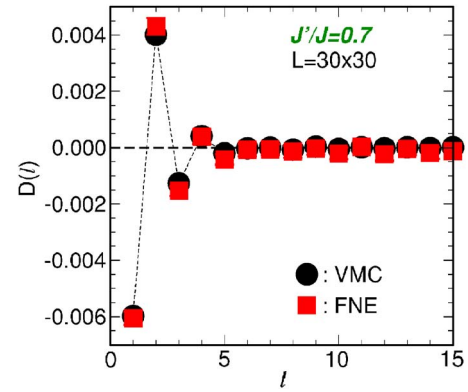

FIG. 20. (Color online) Dimer-dimer correlation functions $D(\vec{r})$ with $\vec{r}=l\vec{\tau}_1$ for the spin-1/2 triangular antiferromagnet with $J'/J=0.7$ and $L=30\times30$ calculated using both variational Monte Carlo (VMC) and FNE methods. The variational ansatz state considered here is the projected BCS state $|p\text{-BCS}\rangle$ (see text), and this state is used as the guiding function $|\psi_G\rangle$ for the FNE calculations.

IV. CONCLUSIONS AND FINAL REMARKS

In this paper, using various quantum Monte Carlo techniques, we have studied the ground state phase diagram as well as the low-lying spin excitations for the spin-1/2 antiferromagnetic Heisenberg model on the triangular lattice as a function of the spatially anisotropic coupling J'/J (Fig. 1). We have found numerical evidence for the presence of two different spin liquid states. The first spin liquid ("algebraic spin liquid") is stable for $J'/J\lesssim0.65$ (see Fig. 21), and is characterized by gapless spin excitations, thus very similar to 1D spin liquids. Conversely, the other spin liquid is rather a new type of spin liquid state, stable for $0.65\lesssim J'/J\lesssim0.8$, and should show a small spin excitation gap. Starting from the isotropic limit $J'=J$ where the ground state is magnetically ordered (classical Néel ordered), quantum fluctuations increase strongly with decreasing the coupling J'/J down to zero. Therefore, the stability of a spin liquid in this region of the phase diagram is quite clear.

The critical coupling J'_C discriminating these two spin liquid phases can be determined in principle by comparing the corresponding energy, and our best estimates of the energy as a function of J'/J are summarized in Fig. 21. From these results, it is concluded that the critical coupling J'_C/J is about 0.65. Because of the limitation of currently available cluster sizes, our approach cannot either determine precisely the critical coupling or describe accurately the nature of the transition. At the variational level, a first order transition occurs at a critical point where the energy curves of the two spin liquid phases (as a function of J'/J), shown in Fig. 21, intersect with different slopes. In the same figure, it is also clear that the two slopes become very close within the FNE calculations, suggesting that the transition would eventually turn to a conventional second order transition, when the quantum fluctuations are more accurately taken into account.

Likewise, we have not tried to determine the critical coupling and to study the nature of the transition between the spin liquid phase and the magnetically ordered phase with incommensurate magnetic order. The latter phase should ap-
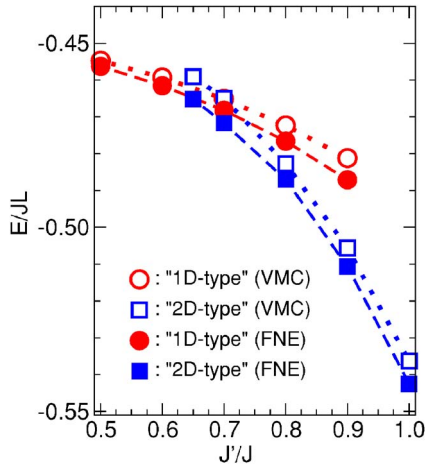
FIG. 21. (Color online) Energy per site for the spin-1/2 antifer-
romagnetic Heisenberg model on the spatially anisotropic triangular
lattice calculated using the variational Monte Carlo (VMC) and the
effective Hamiltonian (FNE) methods. Here two types of spin liquid
wave functions are considered, the one described in Sec. III C (de-
noted by "1D type") and the other described in Secs. III D and III E
(denoted by "2D type"). These wave functions are used as the guid-
ing functions for the FNE calculations.

pear somewhere around $J'/J \gtrsim 0.8$.[5] However, it is very dif-
ficult to perform a finite size scaling analysis to determine
the magnetically ordered incommensurate phase simply be-
cause too large clusters are necessary for an accurate esti-
mate of the magnetic moment.

Our numerical results were obtained using the quantum
variational Monte Carlo method as well as the lattice FN and
FNE methods, which are essentially the Green function
quantum Monte Carlo method with the fixed node approxi-
mation. The FNE ("effective Hamiltonian approach") is a
further improved version of the standard FN method and
developed here in Sec. II C. Although our results might be
affected by this approximation in general, we have shown
that the present methods provide very sensible results for the
isotropic triangular antiferromagnet with $J'=J$ (Sec. III D),
and the numerically exact results for the strongly anisotropic
limit of the 1D uncoupled chains with $J'=0$ (Sec. III B).
Therefore, we have obtained rather reliable results for both
limits of the phase diagram, and the same numerical tools
have been applied also to the still controversial region of the
phase diagram for $0 < J'/J < 1$.

The quality of our approximation in the FN and FNE
methods depends mostly on the choice of the guiding func-
tion $|\psi_G\rangle$, for which we used the best variational ansatz state,
optimized using the SR minimization method (Sec. II B).
The optimization of $|\psi_G\rangle$ is a crucial ingredient of our ap-
proach, because the approximate ground state which we con-
sider, i.e., the numerically exact ground state $|\psi_0^{\rm eff}\rangle$ of the
effective Hamiltonian $\hat{H}^{\rm eff}$, can be computed with the restric-
tion to have the same signs of $|\psi_G\rangle$. Indeed, on small clusters
for which numerically exact diagonalization of the systems
can be done, the variational ansatz state described by a pro-
jected BCS wave function $|p\text{-BCS}\rangle$ provides a very good
average sign $\langle S \rangle$ [Eq. (53)] for both frustrated and non frus-
trated systems as discussed in Sec. III D and also in Refs. 4,
17, and 68

Within this approach, which was shown quite reliable, we
have found a surprisingly stable spin liquid ("algebraic spin
liquid") phase in the regime of large anisotropic couplings
$J'/J \lesssim 0.65$ (Sec. III C). Our numerical calculations also in-
dicate that this spin liquid state shows gapless, fractionalized
spin excitations (Figs. 5 and 6).[48,54] Therefore, we predict
that this 2D algebraic spin liquid state should show peculiar
low energy properties similar to the 1D systems. Although
our conclusion is based on numerical calculations for rather
large clusters (up to 42×42 sites), to be fair, we cannot rule
out a very weak instability toward symmetry-broken ordered
states, as predicted in the $J'/J \to 0$ limit by using the suscep-
tibility criterion based on a random phase approximation
(RPA).[69] Even in that study, the instability occurs in an irrel-
evantly small temperature region, as also pointed out by the
authors.[69] Moreover, it is not clear how reliable the RPA
calculation is for finite values of J'/J.

We have also found another type of spin liquid phase
in the region J'/J close to the isotropic limit, i.e., for
$0.65 \lesssim J'/J \lesssim 0.8$ (Sec. III E). This rather new type of spin
liquid state is characterized by a small spin excitation gap,
and is described by the projected BCS state $|p\text{-BCS}\rangle$ with a
gap function defined by Eq. (55) with a (2×1) unit cell. This
spin liquid state is an extension of the conventional short
range RVB state $|\psi_{\rm RVB}\rangle$ [Eq. (51)], which has been consid-
ered before in the context of the isotropic triangular lattice[3]
and is indeed a very good representation of the exact ground
state of the isotropic triangular antiferromagnet for small
clusters (Sec. III D and Ref. 21).

To extend the short range RVB state, we have constructed
an exact mapping between the short range RVB state and the
projected BCS state $|p\text{-BCS}\rangle$ (Sec. III D and Appendix D). In
doing so, the unit cell of the BCS Hamiltonian, defining the
$|\text{BCS}\rangle$ state, is expanded to a (2×1) unit cell. This mapping
is crucial in the present study because within this approach
the short range RVB state can be easily extended and im-
proved systematically by including hopping integrals, a finite
chemical potential, and most importantly long range gap
functions in the BCS Hamiltonian, with no particular
numerical effort. An additional advantage of using the
$|p\text{-BCS}\rangle$ representation is that it is easy to gain qualitative
insight of the low-lying spin excitations from the corre-
sponding BCS excitation spectrum $E_{\rm k}$.[48,54] For instance, $E_{\rm k}$
of the BCS Hamiltonian, corresponding to the short range
RVB state, shows a finite excitation gap simply because
$-\mu \gg |\Delta_{i,j}|$ (Sec. III D and Appendix C), and therefore a finite
spin gap is expected in the short range RVB state. This is
indeed the correct property of the short range RVB state,
because the presence of a finite spin gap and a very short
correlation length have been established before.[7]

It is worth mentioning a further remarkable property of
this new type of spin liquid state described by this projected
BCS wave function. Without the projection $\mathcal{P}_G$, the BCS
state $|\text{BCS}\rangle$ breaks translation and reflection symmetries be-
cause the BCS Hamiltonian is defined with a (2×1) unit
cell. As a consequence, the BCS excitation spectrum $E_{\rm k}$ has
a finite gap in general. However, as discussed in Sec. III D,
the translation symmetry is recovered after applying the pro-
jection operator onto $|\text{BCS}\rangle$. Therefore, within the projected
BCS wave functions, we have discovered a peculiar way to

open a finite spin gap without breaking the translation symmetry of the state. It is also important to emphasize that the reflection symmetry of the projected state is also restored in the thermodynamic limit, as we have systematically tested numerically (Fig. 13), which, however, cannot be proved rigorously except for the limiting case of the symmetric short range RVB state.

Our finding of stable spin liquid phases in the spin-1/2 anisotropic triangular antiferromagnet is in good agreement with recent studies of the half-filled Hubbard model on the triangular lattice with spatial anisotropic hopping based on the Gutzwiller approximation[70] and the variational Monte Carlo simulations.[71] However, it should be remarked here that the gap function in $|p\text{-BCS}\rangle$ which we found energetically favorable for the nearly isotropic case is rather different from the ones considered in the previous studies.[70,71] Our spin liquid state is defined by a BCS Hamiltonian with a nontranslation invariant gap function, whereas the conventional ansatz state such as the ones considered in Refs. 70 and 71 is defined with a homogeneous gap function, which we found much less accurate close to the isotropic point (see Fig. 21). Although both the Hubbard model in the limit of large on-site repulsion U and the Heisenberg model considered here should be the same, we just note that, with a variational method sensitive only to the energy, it is much easier to find good variational wave functions for a low energy effective Heisenberg model rather than for the corresponding Hubbard model, because the latter contains also the large energy scale U.

In order to have better insight on the low-lying spin excitations of the spin liquid phases, we have directly calculated the spin one excitation dispersion with the method described in Sec. II D. This quantity is particularly important since it can be compared directly with inelastic neutron scattering experiments. The detailed measurements on Cs_2CuCl_4 by Coldea *et al.*[11] are indeed available, for which a spin-liquid-like behavior has been observed.[11] It has been also reported that this material can be described by the model Hamiltonian Eq. (1) with $J'/J \approx 1/3$.[11] As shown in Fig. 10, our calculations were found to be in excellent agreement with the experiments with no fitting parameters. It is also clear from Fig. 10 that the dispersion is 2D characteristic because for uncoupled chains ($J'=0$) the dispersion should be symmetric around the momenta $(\pi/2, 0)$ and $(\pi, 0)$. This excellent agreement strongly supports the existence of this type of 2D spin liquid state. The successful comparison also indicates that our numerical technique can compute accurately the excitation dispersion for the non-trivial strongly anisotropic antiferromagnetic Heisenberg model on the triangular lattice.

Encouraged by these results, we have also calculated the low-lying spin one dispersion for the other spin liquid phase which appears in the region of $0.65 \lesssim J'/J \lesssim 0.8$. A typical results for $J'/J=0.8$ is reported in Fig. 22. This coupling regime is relevant for the organic material $\kappa\text{-}(ET)_2Cu_2(CN)_3$ for which a spin-liquid-like behavior has been also observed.[12,72] Since there is no experimental data available for the spin excitations of this material, our results shown in Fig. 22 provide a theoretical prediction for the spin excitation dispersion, which should be compared with the future neutron scattering experiments. It is interesting to notice that the dispersions for $J'/J=0.8$ and for $J'/J=0.33$ are
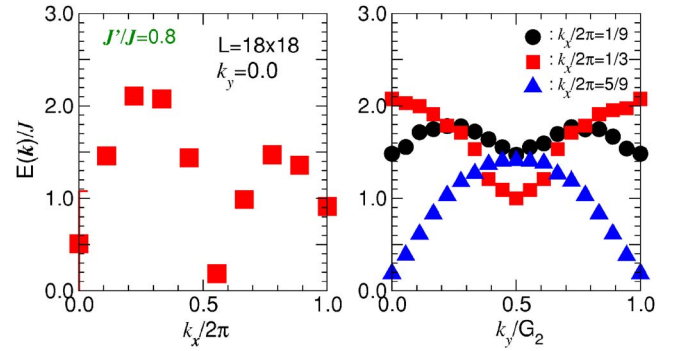

FIG. 22. (Color online) Lowest triplet spin excitations as a function of momentum for the spin-1/2 antiferromagnetic Heisenberg model on the triangular lattice with $J'/J=0.8$ and $L=18\times18$, calculated using the method introduced in Sec. II D. Here $G_2 = 4\pi/\sqrt{3}$.

very similar along the x direction, whereas the difference becomes evident in other momentum regions, for example, along the y-direction. This feature should be also checked experimentally in the feature.

In both spin liquid phases described by our variational ansatz, the spin excitation gap in the thermodynamic limit cannot be resolved by directly computing the excitation dispersions with the method introduced in Sec. II D as the present available system sizes are not large enough. According to the argument presented in the previous section, for $J'/J \simeq 0.8$ a finite spin excitation gap is implied by the corresponding gap in the BCS excitation spectrum $E_{\mathbf{k}}$ of the $|p\text{-BCS}\rangle$ ansatz. However, this gap should be very small because (i) it is close to a transition to an ordered state appearing for larger J'/J and (ii) it is due to the rather small long range part of the gap functions $\Delta_{i,j}$'s. In fact, we have found that the lowest excitation gap in $E_{\mathbf{k}}$ is as small as $\sim$0.2% of $2W$ for $J'/J=0.8$ (where W is the maximum excitation energy in $E_{\mathbf{k}}$).[65] This small gap might also explain an apparent finite spin susceptibility observed on $\kappa\text{-}(ET)_2Cu_2(CN)_3$,[12] which should eventually vanish exponentially at very low temperatures with an activated behavior.

It is also very interesting to note that the organic material $\kappa\text{-}(ET)_2Cu_2(CN)_3$, which shows a spin-liquid-like behavior under ambient pressure,[12] has been very recently found to become a superconductor under small applied pressure (about $4-6\times10^{-1}$ GPa).[73,74] If we assume that the origin of the superconductivity is intimately related to the spin-liquid-like nature of the phase observed next to the superconducting phase, the present study implies a rather unique, unexpected pairing symmetry of the superconductor with a non translation invariant pairing amplitude. This is a measurable effect because the projected BCS state $|p\text{-BCS}\rangle$ discussed in Sec. III E is no longer translation invariant once the projection constraint $\mathcal{P}_G$ is released or mobile carriers are introduced into the homogeneous spin liquid state. Therefore, we expect that this unconventional pairing formation can be probably observed by, e.g., scanning tunneling microscopy experiments.[75]

Based on our numerical calculations and their comparison with experiments, we conclude that the spin liquid is a ge-
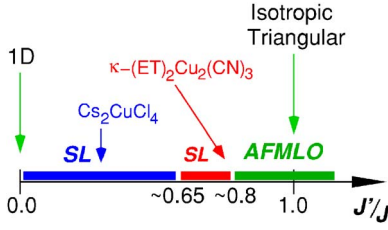
FIG. 23. (Color online) A schematic phase diagram of the spin-1/2 antiferromagnetic Heisenberg model on the triangular lattice. J (J') is the nearest neighbor antiferromagnetic coupling between the spins in the chain (in different chains) (see Fig. 1). SL and AFMLO stand for spin liquid and antiferromagnetic long range order (incommensurate spin order for J'/J away from the isotropic case), respectively. Materials possibly described by this class of models are also indicated.

neric phase of quantum matter, and that, for its stability, it is not important to be very close to a phase transition, unlike the recently proposed scenario in which a spin liquid state appears only at a transition *point* between a magnetically ordered phase and a spontaneously dimerized phase.[76] Within the projected BCS wave function approach, spontaneous dimerization can be correctly described in quasi-1D systems, but not in 2D unless the translation symmetry of the variational state is explicitly broken.[52] Even allowing this possible symmetry breaking, by adding appropriate symmetry breaking terms to the BCS Hamiltonian, we have not found a stable dimerized phase in the present 2D system. Instead, we have found rather stable spin liquid phases. Finally, our phase diagram of the spin-1/2 antiferromagnetic Heisenberg model on the triangular lattice is summarized in Fig. 23, where possibly related materials are also indicated. In particular, it would be very important to distinguish experimentally the two different spin liquid phases predicted here for different values of the coupling J'/J.

APPENDIX A: DETAILS OF THE NUMERICAL CALCULATIONS

In this appendix, we will explain how to define appropriately and calculate efficiently the quantity $O_k(x)$ [Eq. (12)] for each variational parameter α_k of the wave function $|\Psi_{\{\alpha_k\}}\rangle$. Since the derivation is rather general and not restricted to the particular form of the wave function used, we will here indicate the determinantal part of the wave function by $|\Phi_0\rangle$, instead of $|\text{BCS}\rangle$, and thus $|\Psi_{\{\alpha_k\}}\rangle = \mathcal{P}_G|\Phi_0\rangle$. Since it is generally found much more efficient, we will consider a wave function with definite number N of electrons, for which

there are also important simplifications in deriving computationally convenient expressions for the quantities $O_k(x)$.

To this purpose, we will use a particle-hole transformation introduced by Yokoyama and Shiba,[77] which is defined by the following canonical transformation:

$$c_{i\uparrow}^\dagger = \widetilde{C}_i^\dagger,$$

$$c_{i\downarrow}^\dagger = (-1)^{i_1+i_2}\widetilde{C}_{i+L}. \quad (A1)$$

Here $c_{i\sigma}^\dagger$ ($c_{i\sigma}$) is an electron creation (annihilation) operator at site $\vec{r}_i = i_1\vec{\tau}_1 + i_2\vec{\tau}_2$ with spin $\sigma(=\uparrow,\downarrow)$, whereas $\widetilde{C}_i^\dagger$ and $\widetilde{C}_i$ represent the new canonical operators corresponding to the original spin up (spin down) electrons for $i \leq L$ ($L < i \leq 2L$). L is the total number of sites.

After this particle-hole transformation (A1), it is clear that the BCS Hamiltonian [Eq. (3)] can be written as

$$\widetilde{\mathcal{H}}_{\text{BCS}} = \sum_{I,J=1}^{2L} \widetilde{C}_I^\dagger (\bar{H}^{(\text{HF})})_{I,J}\widetilde{C}_J, \quad (A2)$$

where $(\bar{H}^{(\text{HF})})_{I,J}$ are appropriate $2L \times 2L$ matrix elements, which can be straightforwardly computed from Eq. (3). Note that this matrix can be easily evaluated also for rather general Hartree-Fock, BCS Hamiltonians containing, e.g., non translation invariant terms, or several types of orders. The total number of particles $N^{(\text{ph})}$ after the transformation (A1) is related to the total spin along the z direction $S_z = (N_\uparrow - N_\downarrow)/2$ in the original representation through the following equation:

$$N^{(\text{ph})} \equiv \sum_{I=1}^{2L} \widetilde{C}_I^\dagger\widetilde{C}_I = \sum_{i=1}^{L}(c_{i,\uparrow}^\dagger c_{i,\uparrow} + c_{i,\downarrow}c_{i,\downarrow}^\dagger) = L + 2S_z.$$

Since S_z is conserved in the original BCS Hamiltonian, the transformed Hamiltonian (A2) has a definite number $N^{(\text{ph})}$ of particles, as anticipated. With this particle-hole transformation, it is possible to study the spin excitations of the BCS Hamiltonian with $S_z \neq 0$, as well as the ground state which belongs to the singlet $S_z = 0$ sector. Therefore, in the following, we will consider the general case with unrestricted $N^{(\text{ph})}$.

By using an appropriate unitary transformation

$$\widetilde{C}_I = \sum_{\alpha=1}^{2L}(\bar{U})_{I\alpha}\hat{\gamma}_\alpha,$$

$$\hat{\gamma}_\alpha^\dagger = \sum_{i=I}^{2L}(\bar{U})_{I\alpha}\widetilde{C}_I^\dagger, \quad (A3)$$

$\widetilde{\mathcal{H}}_{\text{BCS}}$ is diagonalized with a new set of quasiparticle operators $\{\hat{\gamma}_\alpha^\dagger, \hat{\gamma}_\alpha\}$:

$$\widetilde{\mathcal{H}}_{\text{BCS}} = \sum_{\alpha=1}^{2L} \varepsilon_\alpha \hat{\gamma}_\alpha^\dagger \hat{\gamma}_\alpha, \quad (A4)$$

where, for convenience, the eigenvalues are sorted in ascending order $\varepsilon_1 \leq \varepsilon_2 \leq \cdots \leq \varepsilon_{2L}$.

A natural choice of the Slater determinant part $|\mathbf{\Phi}_0\rangle$ of the variational wave function is the ground state of $\widetilde{\mathcal{H}}_{\mathrm{BCS}}$ with $N^{(\mathrm{ph})}$ particles:

$$|\mathbf{\Phi}_0\rangle = \hat{\gamma}_1^\dagger \hat{\gamma}_2^\dagger \cdots \hat{\gamma}_{N^{(\mathrm{ph})}}^\dagger |\widetilde{0}\rangle, \qquad (A5)$$

where $|\widetilde{0}\rangle$ is the vacuum ($\widetilde{C}_I|\widetilde{0}\rangle=0$) of the Hilbert space after the particle-hole transformation. Thus the Slater determinant for a particle-hole transformed configuration $|x\rangle = \widetilde{C}_{I_1}^\dagger \widetilde{C}_{I_2}^\dagger \cdots \widetilde{C}_{I_{N^{(\mathrm{ph})}}}^\dagger |\widetilde{0}\rangle$ is

$$\langle x|\mathbf{\Phi}_0\rangle = \det[\bar{S}], \qquad (A6)$$

where $\bar{S}$ is a $N^{(\mathrm{ph})} \times N^{(\mathrm{ph})}$ matrix, whose elements are

$$(\bar{S})_{l,\alpha} = \langle \widetilde{0}|\widetilde{C}_{I_l}\hat{\gamma}_\alpha^\dagger|\widetilde{0}\rangle = (\bar{U})_{I_l\alpha}, \qquad (A7)$$

I_l's ($1 \le I_l \le 2L$) are the "positions" of the $N^{(\mathrm{ph})}$ particles ($l=1,2,\ldots,N^{(\mathrm{ph})}$) corresponding to the configuration $|x\rangle$, and $\alpha = \{1,2,\ldots,N^{(\mathrm{ph})}\}$.

Now let us consider small changes for $\alpha_k \to \alpha_k' = \alpha_k + \delta\alpha_k$. Since $\widetilde{\mathcal{H}}_{\mathrm{BCS}}$ depends linearly on $\{\alpha_k\}$, the perturbed system is described by

$$\widetilde{\mathcal{H}}_{\mathrm{BCS}}' = \widetilde{\mathcal{H}}_{\mathrm{BCS}} + \sum_{k=1}^p \delta\alpha_k \cdot \hat{V}_k, \qquad (A8)$$

where $\hat{V}_k = \Sigma_{I,J=1}^{2L}(\bar{V}^{(k)})_{IJ}\widetilde{C}_I^\dagger\widetilde{C}_J$ is a suitable operator proportional to the chosen variational parameter α_k. For instance, when the chemical potential is changed $\mu \to \mu + \delta\mu$, namely, a term $-\delta\mu\Sigma_{i=1}^L\Sigma_\sigma c_{i,\sigma}^\dagger c_{i,\sigma}$ is added to $\hat{H}_{\mathrm{BCS}}$, the corresponding matrix element $(\bar{V}^{(k)})_{IJ}$ is $-\delta_{I,J}$ for $I \le L$ and $\delta_{I,J}$ for $I > L$, due to the particle-hole transformation (A1). Here $\delta_{i,j}$ is the Kronecker δ function. When a small change in a pairing term $[\Delta_{i,j}c_{i,\uparrow}^\dagger c_{j,\downarrow}^\dagger + \mathrm{H.c.}]$ is considered, the corresponding matrix element $(\bar{V}^{(k)})_{IJ}$ is $(-1)^{j_1+j_2}[\delta_{I,i}\delta_{J,j+L} + \delta_{I,j+L}\delta_{J,i}]$ where $\vec{r}_j = j_1\vec{\tau}_1 + j_2\vec{\tau}_2$.

With the basis set formed by the quasiparticle operators $\{\hat{\gamma}_\alpha^\dagger, \hat{\gamma}_\alpha\}$, the matrix $\bar{V}^{(k)}$ is transformed as $\bar{V}^{(k)} \to \bar{U}^\dagger\bar{V}^{(k)}\bar{U}$, and thus the first order correction to the state $|\mathbf{\Phi}_0\rangle$ is easily computed as follows:

$$|\mathbf{\Phi}_0'\rangle = \left[1 + \sum_{k=1}^p \delta\alpha_k \sum_{\eta,\nu=1}^{2L} (\bar{Q}^{(k)})_{\eta\nu}\gamma_\eta^\dagger\gamma_\nu \right]|\mathbf{\Phi}_0\rangle + \mathcal{O}(\delta\alpha_k^2), \qquad (A9)$$

where

$$(\bar{Q}^{(k)})_{\eta\nu} = \begin{cases} \dfrac{[\bar{U}^\dagger\bar{V}^{(k)}\bar{U}]_{\eta\nu}}{\varepsilon_\nu - \varepsilon_\eta} & \text{for } \eta > N^{(\mathrm{ph})} \text{ and } \nu \le N^{(\mathrm{ph})}, \\ 0 & \text{otherwise}. \end{cases} \qquad (A10)$$

This expression is well defined as long as $|\mathbf{\Phi}_0\rangle$ is nondegenerate, so that the denominator in the definition of $\bar{Q}^{(k)}$ is always nonzero. This condition is rather generally satisfied

for the BCS Hamiltonian. We can now readily express the state $|\mathbf{\Phi}_0'\rangle$ in terms of the $\{\widetilde{C}^\dagger, \widetilde{C}\}$ basis set

$$|\mathbf{\Phi}_0'\rangle = \left[1 + \sum_{k=1}^p \delta\alpha_k \sum_{I,J=1}^{2L} (\bar{M}^{(k)})_{IJ}\widetilde{C}_I^\dagger\widetilde{C}_J \right]|\mathbf{\Phi}_0\rangle + \mathcal{O}(\delta\alpha_k^2), \qquad (A11)$$

where $\bar{M}^{(k)} = \bar{U}\bar{Q}^{(k)}\bar{U}^\dagger$. At each iteration of the SR minimization procedure described in Sec. II B, $\bar{M}^{(k)}$ has to be computed, because the operators $\{\hat{\gamma}_\alpha^\dagger, \hat{\gamma}_\alpha\}$ change every time a new set of $\{\alpha_k\}$ is calculated. This can be done using four matrix-matrix multiplications.

From Eq. (A11), it is now easy to evaluate the perturbed Slater determinant $\langle x|\mathbf{\Phi}_0'\rangle$, and thus an explicit expression for $O_k(x)$ defined by Eqs. (12) and (13):

$$O_k(x) = \sum_{I=1}^{2L}\sum_{J=1}^{2L}(\bar{M}^{(k)})_{IJ}\frac{\langle x|\widetilde{C}_I^\dagger\widetilde{C}_J|\mathbf{\Phi}_0\rangle}{\langle x|\mathbf{\Phi}_0\rangle} = \sum_{l=1}^{N^{(\mathrm{ph})}}\sum_{J=1}^{2L}(\bar{M}^{(k)})_{I_lJ}\mathcal{G}_{Jl}. \qquad (A12)$$

Here $\mathcal{G}_{Jl}$ is a local single-particle "Green's function"

$$\mathcal{G}_{Jl} \equiv \frac{\langle x|\widetilde{C}_{I_l}^\dagger\widetilde{C}_J|\mathbf{\Phi}_0\rangle}{\langle x|\mathbf{\Phi}_0\rangle} = \sum_{\alpha=1}^{N^{(\mathrm{ph})}}(\bar{U})_{J\alpha}(\bar{S}^{-1})_{\alpha l}, \qquad (A13)$$

which is computed and updated during the variational Monte Carlo iterations. Since the matrix $\bar{M}^{(k)}$ does not depend on the configuration $|x\rangle$ and $\mathcal{G}_{Jl}$ is always known, only about L^2 operations are required to evaluate $O_k(x)$ for each k and for each sampled configuration $|x\rangle$. Finally, we note that when the variational wave function $|\Psi_{\{\alpha_k\}}\rangle$ contains the spin Jastrow factor $\mathcal{J}_S = \exp[\Sigma_{i,j=1(i<j)}^L v_{ij}\hat{S}_i^z\hat{S}_j^z]$, i.e., $|\Psi_{\{\alpha_k\}}\rangle = \mathcal{P}_G\mathcal{J}_S|\mathbf{\Phi}_0\rangle$, the calculation of $O_k(x)$ corresponding to the variational parameter v_{ij} is much simpler and straightforward, because $O_k(x)$ is simply $\langle x|\hat{S}_i^z\hat{S}_j^z|x\rangle$ in this case.

APPENDIX B: MARSHALL SIGN RULE AND PROJECTED BCS WAVE FUNCTIONS

In this appendix, we will show that a BCS wave function projected onto the subspace of singly occupied sites satisfies the Marshall sign rule provided the corresponding BCS Hamiltonian

$$\hat{H}_{\mathrm{BCS}} = \sum_{j,l}\left[t_{j,l}\left(\sum_\sigma c_{j\sigma}^\dagger c_{l\sigma}\right) + (\Delta_{j,l}c_{j\uparrow}^\dagger c_{l\downarrow}^\dagger + \mathrm{H.c.}) \right] \qquad (B1)$$

satisfies the following conditions:

$$t_{j,l} = \Delta_{j,l} = 0: \text{ for } j \text{ and } l \text{ on the same sublattice.} \qquad (B2)$$

Here $c_{i\sigma}^\dagger$ ($c_{i\sigma}$) is an electron creation (annihilation) operator at site $\mathbf{r}_i = i_1\vec{\tau}_1 + i_2\vec{\tau}_2$ with spin $\sigma(=\uparrow,\downarrow)$, and $t_{j,k}$ and $\Delta_{j,k}$ are assumed symmetric under $j \leftrightarrow k$ interchange and real. It is also assumed that the ground state of the BCS Hamiltonian $|\mathrm{BCS}\rangle$ is unique, namely with a finite size gap to the first excitation, a condition which can be generally met for nontrivial values of $\Delta_{i,j}$ and $t_{i,j}$.

In what follows, we will show that the projected BCS wave function $|p\text{-BCS}\rangle = \mathcal{P}_G|\text{BCS}\rangle$ constructed from the BCS state above satisfies the Marshall sign rule, namely,

$$\text{sgn}[\langle x|\text{BCS}\rangle] = (-1)^{N_A}, \tag{B3}$$

where N_A is the number of down spins on one of the two sublattices, and $|x\rangle$ is an electron configuration with no doubly occupied sites, which can be written as

$$\langle x| = \langle 0|\prod_{i=1}^{L} c_{i\sigma_i}$$

with the $c_{i\sigma_i}$ factors being ordered from left to right according to the increasing index i (σ_i is the spin of the electron on site i). Here it is assumed that the number of sites (L) is even.

First, it is convenient to perform the following particle-hole transformation for the down spins only:

$$c_{l\uparrow} = d_{l\uparrow},$$

$$c_{l\downarrow} = (-1)^{l_1+l_2}d_{l\downarrow}^{\dagger}. \tag{B4}$$

With this transformation, the BCS Hamiltonian is transformed to a standard one-body Hamiltonian commuting with the total number of particles, i.e.,

$$\hat{H}_{\text{BCS}} = \sum_{j,l}\left[t_{j,l}\left(\sum_{\sigma}d_{j\sigma}^{\dagger}d_{l\sigma}\right) + \Delta_{j,l}(-1)^{l_1+l_2}\right.$$
$$\left. \times\left(\sum_{\sigma,\sigma'}d_{j\sigma}^{\dagger}d_{l\sigma'}2iS_{\sigma\sigma'}^{y}\right)\right], \tag{B5}$$

where "i" denotes the imaginary unit, S^y is the y component of the spin matrix, and condition (B2) is used. On the other hand, after this transformation (B4), the basis of no doubly occupied sites turns into

$$|\uparrow\rangle \rightarrow |\uparrow\downarrow\rangle,$$

$$|\downarrow\rangle \rightarrow |0\rangle,$$

namely, the sites are either doubly occupied or empty in the new representation, and all configurations $\{\hat{x}\}$ are now defined by the $L/2$ positions of the doubly occupied sites:

$$\langle\hat{x}| = \langle 0|d_{\mathbf{R}_1\downarrow}d_{\mathbf{R}_1\uparrow}d_{\mathbf{R}_2\downarrow}d_{\mathbf{R}_2\uparrow}\cdots d_{\mathbf{R}_{L/2}\downarrow}d_{\mathbf{R}_{L/2}\uparrow},$$

where $\mathbf{R}_l \in \{\mathbf{r}_1, \mathbf{r}_2, \ldots, \mathbf{r}_L\}$. Because of the additional phase in Eq. (B4), $\langle x|$ is related to $\langle\hat{x}|$ by $\langle x| = (-1)^{N_A}\langle\hat{x}|$. Therefore, using the definition of the Marshall sign (B3), a state with the Marshall sign rule in the original basis $\{x\}$ is equivalent to a bosonic state in the particle-hole transformed basis $\{\hat{x}\}$: for each configuration $|\hat{x}\rangle$, the wave function should be always positive (or always negative).

In order to show this bosonic rule for the projected BCS state considered, it should be noticed that the new basis $\{\hat{x}\}$ is invariant under a global rotation of the spins which transforms the spin matrix $S_{\sigma\sigma'}^{y}$ into $S_{\sigma\sigma'}^{z} = \sigma\delta_{\sigma\sigma'}/2$:

$$\begin{pmatrix} d_{j\uparrow} \\ d_{j\downarrow} \end{pmatrix} = \frac{1}{\sqrt{2}}\begin{pmatrix} 1 & i \\ -i & -1 \end{pmatrix}\begin{pmatrix} a_{j\uparrow} \\ a_{j\downarrow} \end{pmatrix}. \tag{B6}$$

Indeed, $d_{j\uparrow}d_{j\downarrow}$ is transformed into $a_{j\downarrow}a_{j\uparrow}$. It is also easily shown that this transformation (B6) factorizes the Hamiltonian (B5) as

$$\hat{H}_{\text{BCS}} = \sum_{\sigma}\left[\sum_{i,j}(\bar{H}_{\sigma})_{ij}a_{i\sigma}^{\dagger}a_{i\sigma}\right], \tag{B7}$$

where $\bar{H}_{\uparrow} = \bar{H}_{\downarrow}^{*}$, $\bar{H}_{\uparrow}$ and $\bar{H}_{\downarrow}$ being appropriate one-body Hamiltonian matrices whose eigenstates are $\phi_{\alpha}(\mathbf{r})$ and $\phi_{\alpha}^{*}(\mathbf{r})$, respectively ($\alpha = 1, 2, \ldots, L$). Therefore, the ground state $|\text{BCS}\rangle$ of $\hat{H}_{\text{BCS}}$ once computed in the basis of doubly occupied and empty sites $\{\hat{x}\}$ reads

$$\langle\hat{x}|\text{BCS}\rangle = |\text{Det}(\bar{S})|^2 > 0, \tag{B8}$$

where $\bar{S}$ is a ($L \times L$) matrix with $(\bar{S})_{l,\alpha} = \phi_{\alpha}(\mathbf{R}_l)$. This proves the statement given at the beginning of this Appendix.

Finally, we note that the condition (B2) is satisfied whenever the BCS Hamiltonian (B1) is invariant under a particle-hole transformation

$$c_{i\sigma}^{\dagger} \rightarrow (-1)^{i_1+i_2}c_{i\sigma}, \tag{B9}$$

provided $t_{j,k} = t_{k,j}$ and $\Delta_{j,k}$ is real. Equation (43) in Sec. III A follows readily from this particle-hole symmetric condition.

APPENDIX C: BCS WAVE FUNCTION WITH A BROKEN TRANSLATION SYMMETRY

In this Appendix, several important properties are discussed on the ground state $|\text{BCS}\rangle$ of the BCS Hamiltonian which breaks primitive lattice translation symmetry by extending the unit cell to (2×1). The resulting state $|\text{BCS}\rangle$ is used to build projected BCS states $|p\text{-BCS}\rangle = \mathcal{P}_G|\text{BCS}\rangle$ for the isotropic and nearly isotropic triangular systems discussed in Secs. III D and III E, respectively.

Let us start with defining the BCS Hamiltonian $\hat{H}_{\text{BCS}}$ introduced in Sec. II A in a slightly different way. A part of $\hat{H}_{\text{BCS}}$ which is invariant under any primitive lattice translations on the triangular lattice (Fig. 1) can be generally described by the following Hamiltonian:

$$\hat{H}_{\text{BCS}}^{(0)} = -\sum_{\vec{r},\sigma}\left[\sum_{\vec{t}_m}' t_{\vec{t}_m}(c_{\vec{r}\sigma}^{\dagger}c_{\vec{r}+\vec{t}_m\sigma} + c_{\vec{r}+\vec{t}_m\sigma}^{\dagger}c_{\vec{r}\sigma})\right]$$
$$+ \sum_{\vec{r}}\left[\sum_{\vec{t}_m}' \Delta_{\vec{t}_m}(c_{\vec{r}\uparrow}^{\dagger}c_{\vec{r}+\vec{t}_m\downarrow}^{\dagger} - c_{\vec{r}\downarrow}^{\dagger}c_{\vec{r}+\vec{t}_m\uparrow}^{\dagger}) + \text{H.c.}\right]$$
$$- \mu\sum_{\vec{r},\sigma}c_{\vec{r}\sigma}^{\dagger}c_{\vec{r}\sigma}, \tag{C1}$$

where the first sum $\Sigma_{\vec{r}}$ runs over all lattice vectors $\vec{r} = r_1\vec{\tau}_1 + r_2\vec{\tau}_2$ (r_1, r_2: integer), whereas the second sum $\Sigma_{\vec{t}_m}'$ is for $\vec{t}_m = m_1\vec{\tau}_1 + m_2\vec{\tau}_2$ (m_1, m_2: integer) with $m_2 > 0$ or with $m_1 > 0$ and $m_2 = 0$ as denoted by solid circles in Fig. 24(a). Now let us add to $\hat{H}_{\text{BCS}}^{(0)}$ an additional pairing term $\hat{V}_{\text{pair}}$ which breaks the underlying lattice translation symmetry
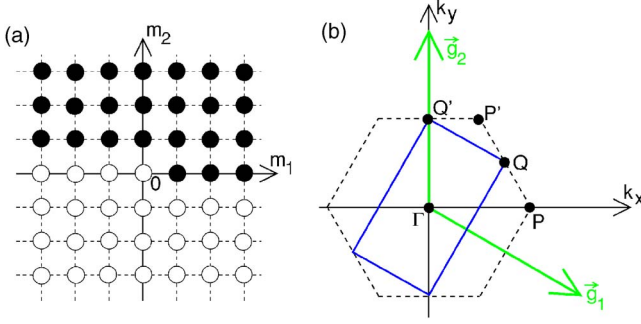
FIG. 24. (Color online) (a) Region of (m_1, m_2) (denoted by solid circles) considered for the sum over $\vec{t}_m = m_1 \vec{\tau}_1 + m_2 \vec{\tau}_2$. Each circle corresponds to a pair of integers (m_1, m_2). (b) The first Brillouin zone (hexagon drown by dashed lines) for the triangular lattice shown in Fig. 1. The corresponding reciprocal lattice vectors are $\vec{g}_1 = 2\pi(1, -\frac{1}{\sqrt{3}})$ and $\vec{g}_2 = 2\pi(0, \frac{2}{\sqrt{3}})$. The reduced Brillouin zone (tilted rectangle) is also given by solid lines. Several symmetric points are Γ: (0,0), P: $(\frac{4}{3}\pi, 0)$, Q: $(\pi, \frac{\pi}{\sqrt{3}})$, P′: $(\frac{2}{3}\pi, \frac{2}{\sqrt{3}}\pi)$, and Q′: $(0, \frac{2}{\sqrt{3}}\pi)$.

$$\hat{V}_{\text{pair}} = \sum_{\vec{r}} \left[\sum_{\vec{t}_m}' (-1)^{r_1} \bar{\Delta}_{\vec{t}_m} (c_{\vec{r}\uparrow}^\dagger c_{\vec{r}+\vec{t}_m\downarrow}^\dagger - c_{\vec{r}\downarrow}^\dagger c_{\vec{r}+\vec{t}_m\uparrow}^\dagger) + \text{H.c.} \right].$$

(C2)

Note that the unit cell of the total BCS Hamiltonian $\hat{H}_{\text{BCS}} = \hat{H}_{\text{BCS}}^{(0)} + \hat{V}_{\text{pair}}$ is now extended to (2×1). In the following, $t_{\vec{t}_m}$, $\Delta_{\vec{t}_m}$, $\bar{\Delta}_{\vec{t}_m}$, and μ are all assumed to be real.

Let us first explore the excitation spectrum of $\hat{H}_{\text{BCS}}$. For this purpose, it is convenient to Fourier transform the BCS Hamiltonian to the momentum space with the reciprocal lattice vectors $\vec{g}_1 = 2\pi(1, -\frac{1}{\sqrt{3}})$ and $\vec{g}_2 = 2\pi(0, \frac{2}{\sqrt{3}})$ [see Fig. 24(b)]. After the Fourier transformation with $c_{\vec{r}\sigma}^\dagger = \frac{1}{\sqrt{L}} \sum_{\vec{k}} e^{-i\vec{k}\cdot\vec{r}} c_{\vec{k}\sigma}^\dagger$, $\hat{H}_{\text{BCS}}$ can be conveniently described by the following (4×4) matrix form:

$$\hat{H}_{\text{BCS}} = \sum_{\vec{k}}' (c_{\vec{k}\uparrow}^\dagger, \ c_{\vec{k}+\vec{Q}\uparrow}^\dagger, \ c_{-\vec{k}\downarrow}, \ c_{-(\vec{k}+\vec{Q})\downarrow})$$

$$\times \begin{pmatrix} \xi_1(\vec{k}) & 0 & \Delta_{11}(\vec{k}) & \Delta_{12}(\vec{k}) \\ 0 & \xi_2(\vec{k}) & \Delta_{12}(\vec{k})^* & \Delta_{22}(\vec{k}) \\ \Delta_{11}(\vec{k}) & \Delta_{12}(\vec{k}) & -\xi_1(\vec{k}) & 0 \\ \Delta_{12}(\vec{k})^* & \Delta_{22}(\vec{k}) & 0 & -\xi_2(\vec{k}) \end{pmatrix} \begin{pmatrix} c_{\vec{k}\uparrow} \\ c_{\vec{k}+\vec{Q}\uparrow} \\ c_{-\vec{k}\downarrow}^\dagger \\ c_{-(\vec{k}+\vec{Q})\downarrow}^\dagger \end{pmatrix},$$

(C3)

where

$$\xi_1(\vec{k}) = -2\sum_{\vec{t}_m}' t_{\vec{t}_m} \cos(\vec{k} \cdot \vec{t}_m) - \mu,$$

$$\xi_2(\vec{k}) = -2\sum_{\vec{t}_m}' t_{\vec{t}_m} \cos[(\vec{k} + \vec{Q}) \cdot \vec{t}_m] - \mu$$

(C4)

and

$$\Delta_{11}(\vec{k}) = 2\sum_{\vec{t}_m}' \Delta_{\vec{t}_m} \cos(\vec{k} \cdot \vec{t}_m),$$

$$\Delta_{22}(\vec{k}) = 2\sum_{\vec{t}_m}' \Delta_{\vec{t}_m} \cos[(\vec{k} + \vec{Q}) \cdot \vec{t}_m],$$

$$\Delta_{12}(\vec{k}) = \sum_{\vec{t}_m}' \bar{\Delta}_{\vec{t}_m} (e^{i(\vec{k}+\vec{Q})\cdot\vec{t}_m} + e^{-i\vec{k}\cdot\vec{t}_m})$$

(C5)

with $\vec{Q} = \vec{g}_1/2$ so that $\vec{Q} \cdot \vec{r} = \pi r_1$. The primed sum $\sum_{\vec{k}}'$ runs over the reduced Brillouin zone shown in Fig. 24(b), or equivalently, e.g., for parallelogram lattice of $L = L_1 \times L_2$ (L_1, L_2: even) with $\vec{k} = \frac{k_1}{L_1}\vec{g}_1 + \frac{k_2}{L_2}\vec{g}_2$, the primed sum is taken over $k_1 = 0, 1, \ldots, L_1/2 - 1$ and $k_2 = 0, 1, \ldots, L_2 - 1$.

The excitation spectrum of the BCS Bogoliubov mode for this BCS Hamiltonian is now easily calculated by diagonalizing the (4×4) Hamiltonian matrix given in Eq. (C3). It turned out that the excitation spectrum $E_{\vec{k}}$ is doubly degenerate at each momentum $\vec{k}$ and is given by $E_{\vec{k}} = E_{\vec{k}}^{(\pm)}$, where

$$E_{\vec{k}}^{(\pm)} = [Q_0(\vec{k}) \pm Q_1(\vec{k})]^{1/2}$$

(C6)

and

$$Q_0(\vec{k}) = \frac{1}{2}[\xi_1(\vec{k})^2 + \xi_2(\vec{k})^2 + \Delta_{11}(\vec{k})^2 + \Delta_{22}(\vec{k})^2 + 2|\Delta_{12}(\vec{k})|^2],$$

$$Q_1(\vec{k}) = \frac{1}{2}([\xi_1(\vec{k})^2 - \xi_2(\vec{k})^2 + \Delta_{11}(\vec{k})^2 - \Delta_{22}(\vec{k})^2]^2 + 4|\Delta_{12}(\vec{k})|^2\{[\xi_1(\vec{k}) - \xi_2(\vec{k})]^2 + [\Delta_{11}(\vec{k}) + \Delta_{22}(\vec{k})]^2\})^{1/2}.$$

From this expression, it is clear that generally $E_{\vec{k}}^{(\pm)}$ has a finite excitation gap except for some special cases.

So far no assumption has been made for the values of real gap functions $\Delta_{\vec{t}_m}$ and $\bar{\Delta}_{\vec{t}_m}$. As will be discussed in Appendix D, in order to be consistent with the phase rule [Eqs. (D8) and (D9)] and for $\hat{H}_{\text{BCS}}$ to be invariant under the transformation $\mathcal{T}_1 \otimes \mathcal{U}$ (Sec. III D), the gap functions $\Delta_{\vec{t}_m}$ and $\bar{\Delta}_{\vec{t}_m}$ are subject to the following conditions:

$$\Delta_{\vec{t}_m} = 0 \quad \text{for } m_2 \text{ odd},$$

$$\bar{\Delta}_{\vec{t}_m} = 0 \quad \text{for } m_2 \text{ even}.$$

(C7)

With this condition, $\Delta(\vec{t}_m)$ given in Eq. (55) is equivalent to $\Delta_{\vec{t}_m}$ and $\bar{\Delta}_{\vec{t}_m}$ defined here.

Let us now consider one special but important case for which all hopping terms $t_{\vec{t}_m}$ are zero and $\Delta_{11}(\vec{k}) = -\Delta_{22}(\vec{k})$. In this case, $Q_1(\vec{k}) = 0$, and therefore the excitation spectrum for the Bogoliubov mode is simply

$$E_{\vec{k}} = [\mu^2 + \Delta_{11}(\vec{k})^2 + |\Delta_{12}(\vec{k})|^2]^{1/2}.$$

(C8)

After tedious but straightforward calculations, the ground state $|\text{BCS}\rangle$ of the BCS Hamiltonian $\hat{H}_{\text{BCS}}$ for this special case can be calculated analytically:

$$|\text{BCS}\rangle = \exp\left[\sum_{\vec{\tau}_m}' \{f_{11}(\vec{k})c^\dagger_{\vec{k}\uparrow}c^\dagger_{-\vec{k}\downarrow} + f_{22}(\vec{k})c^\dagger_{\vec{k}+\vec{Q}\uparrow}c^\dagger_{-(\vec{k}+\vec{Q})\downarrow} + f_{12}(\vec{k})\right.$$

$$\left. \times (c^\dagger_{\vec{k}\uparrow}c^\dagger_{-(\vec{k}+\vec{Q})\downarrow} - c^\dagger_{\vec{k}\downarrow}c^\dagger_{-(\vec{k}+\vec{Q})\uparrow})\}\right]|0\rangle, \tag{C9}$$

where

$$f_{11}(\vec{k}) = -f_{22}(\vec{k}) = -\frac{\Delta_{11}(\vec{k})}{E_{\vec{k}} - \mu},$$

$$f_{12}(\vec{k}) = -\frac{\Delta_{12}(\vec{k})}{E_{\vec{k}} - \mu}, \tag{C10}$$

and $\Delta_{12}(\vec{k})^* = \Delta_{12}(-\vec{k})$ is used. This state should be compared with the more conventional one given by Eq. (9) where there is only one site per unit cell. Finally, let us consider two more specific cases separately. Case (1): $\mu = 0$ and only nearest neighbor gap functions are finite, i.e., $\Delta_{\vec{\tau}_1} = \bar{\Delta}_{\vec{\tau}_2} = \bar{\Delta}_{\vec{\tau}_2 - \vec{\tau}_1} = \Delta$ (see Fig. 11). Because $\Delta_{11}(\vec{k}) = -\Delta_{22}(\vec{k}) = 2\Delta\cos(\vec{k}\cdot\vec{\tau}_1)$ and $\Delta_{12}(\vec{k}) = 2\Delta\{\cos(\vec{k}\cdot\vec{\tau}_2) - i\sin[\vec{k}\cdot(\vec{\tau}_2 - \vec{\tau}_1)]\}$, $E_{\vec{k}}$ has gapless excitations at $\vec{k} = \vec{g}_1/4 + \vec{g}_2/4$ and $-\vec{g}_1/4 \pm \vec{g}_2/4$. Case (2): $\mu \to -\infty$. Since $f_{11}(\vec{k}) \propto -\Delta_{11}(\vec{k})$ and $f_{12}(\vec{k}) \propto -\Delta_{12}(\vec{k})$ in this limit, i.e., a pairing function is proportional to a gap function, a projected BCS wave function $|p\text{-BCS}\rangle$ built from this BCS state becomes

$$\lim_{\mu \to -\infty} |p\text{-BCS}\rangle = \mathcal{P}_G\left[\sum_{\vec{r}}\left\{\sum_{\vec{\tau}_m}'[\Delta_{\vec{\tau}_m} + (-1)^{r_1}\bar{\Delta}_{\vec{\tau}_m}](c^\dagger_{\vec{r}\uparrow}c^\dagger_{\vec{r}+\vec{\tau}_m\downarrow} - c^\dagger_{\vec{r}\downarrow}c^\dagger_{\vec{r}+\vec{\tau}_m\uparrow})\right\}\right]^{L/2}|0\rangle. \tag{C11}$$

From this result, it it clear that the projected BCS state discussed here indeed includes a short range RVB wave function $|\psi_{\text{RVB}}\rangle$ since if $\Delta_{\vec{\tau}_1} = \bar{\Delta}_{\vec{\tau}_2} = \bar{\Delta}_{\vec{\tau}_2 - \vec{\tau}_1}$ (all other gap functions are zero) is chosen, the above wave function (C11) consists of the pairing functions with exactly the same phase as in Eqs. (D8) and (D9). More details of this relation will be found in the next Appendix.

APPENDIX D: PFAFFIAN AND PROJECTED BCS WAVE FUNCTIONS

We start from the definition of a Pfaffian in terms of an antisymmetric $2N \times 2N$ matrix $\bar{f}$ where $f_{i,j} = -f_{j,i}$. The Pfaffian of matrix $\bar{f}$ is

$$P[\bar{f}] = \sum_{\substack{(i_1<j_1),(i_2<j_2),\ldots,(i_N<j_N) \\ \text{and } i_1<i_2\cdots<i_N}} (-1)^p \prod_{k=1}^{N} f_{i_k,j_k}, \tag{D1}$$

where the sum runs over all possible covering of indices $\{(i_1,j_1),(i_2,j_2),\ldots,(i_N,j_N)\}$ such that $i_k < j_k$ and $i_1 < i_2 < i_3 < \cdots < i_N$, being p the parity of the permutation of the $2N$ indices

$$\begin{pmatrix} 1 & 2 & 3 & 4 & \cdots & 2N-1 & 2N \\ i_1 & j_1 & i_2 & j_2 & \cdots & i_N & j_N \end{pmatrix}.$$

The most important relation known for the Pfaffian is that $(P[\bar{f}])^2 = \text{Det}[\bar{f}]$, which, however, will not be used in the following.

Now let us suppose that the indices $1,2,3,\ldots,2N$ label the positions of a lattice (not necessarily one dimensional). Then each covering of the indices in the Pfaffian is interpreted as a particular dimer configuration in which, for example, a spin singlet pair located at sites (i_k,j_k) is assigned.

We can now define two spin wave functions in terms of these dimer coverings. The first wave function is expanded in the well known valence bond basis[78]

$$|\text{RVB}\rangle = \sum_{\substack{(i_1<j_1),(i_2<j_2),\ldots,(i_N<j_N) \\ \text{and } i_1<i_2\cdots<i_N}} (-1)^p\left[\prod_{k=1}^{N} f_{i_k,j_k}(S^-_{j_k} - S^-_{i_k})\right]|F\rangle, \tag{D2}$$

where S^-_i is the spin-1/2 lowering operator at site i, $|F\rangle$ is the ferromagnetic state defined by

$$|F\rangle = c^\dagger_{1,\uparrow}, c^\dagger_{2,\uparrow}, \ldots, c^\dagger_{2N,\uparrow}|0\rangle, \tag{D3}$$

and $|0\rangle$ is the electron vacuum. Notice that for convenience we have included in the definition of the wave function the same permutation sign $(-1)^p$ appearing in the Pfaffian (D1). The second wave function is the projected BCS state

$$|p - \text{BCS}\rangle = \mathcal{P}_G\exp\left[\sum_{\substack{i,j=1 \\ (i<j)}}^{2N} f_{i,j}(c^\dagger_{i,\uparrow}c^\dagger_{j,\downarrow} - c^\dagger_{i,\downarrow}c^\dagger_{j,\uparrow})\right]|0\rangle, \tag{D4}$$

where $\mathcal{P}_G$ is the Gutzwiller projection operator onto singly occupied sites. In both wave functions, we have used the upper triangular part of the antisymmetric matrix $\bar{f}$, whereas the tedious permutation sign $(-1)^p$ is present only in the wave function $|\text{RVB}\rangle$. We shall now show that the two wave functions $|p\text{-BCS}\rangle$ and $|\text{RVB}\rangle$ are actually the same for any $\bar{f}$ and on any lattice with all possible boundary conditions.

Proof. Because the projection $\mathcal{P}_G$ forbids double occupancy and thus singlet bonds sharing the common site, the projected BCS wave function $|p\text{-BCS}\rangle$ can be expanded for all dimer coverings as follows:

$$|p\text{-BCS}\rangle = \frac{1}{N!}\mathcal{P}_G\left[\sum_{\substack{i,j=1 \\ (i<j)}}^{2N} f_{i,j}(c^\dagger_{i,\uparrow}c^\dagger_{j,\downarrow} - c^\dagger_{i,\downarrow}c^\dagger_{j,\uparrow})\right]^N|0\rangle$$

$$= \sum_{\substack{(i_1<j_1),(i_2<j_2),\ldots,(i_N<j_N) \\ \text{and } i_1<i_2\cdots<i_N}} \prod_{k=1}^{N}[f_{i_k,j_k}(c^\dagger_{i_k,\uparrow}c^\dagger_{j_k,\downarrow} - c^\dagger_{i_k,\downarrow}c^\dagger_{j_k,\uparrow})]$$

$$\times |0\rangle, \tag{D5}$$

where in the last formula the constant $1/N!$ cancels out the

factor due to the ordering of the indices $i_1 < i_2, \ldots, < i_N$. On the other hand, by substituting the definition of the ferromagnetic state in the wave function $|\text{RVB}\rangle$ and making the necessary p^* fermion permutations for each dimer covering, we arrive at the following expression:

$$|\text{RVB}\rangle = \sum_{\substack{(i_1 < j_1),(i_2 < j_2),\ldots,(i_N < j_N) \\ \text{and } i_1 < i_2 \cdots < i_N}} (-1)^p (-1)^{p^*}$$
$$\times \left[\prod_{k=1}^{N} f_{i_k j_k} (S_{j_k}^- - S_{i_k}^-) c_{i_k,\uparrow}^\dagger c_{j_k,\uparrow}^\dagger \right] |0\rangle. \quad (D6)$$

By simple inspection, it is readily realized that the fermion sign $(-1)^{p^*}$ is exactly the one $(-1)^p$ defining the permutation sign of the covering of indices $\{(i_k, j_k)\}$, and that $(S_{j_k}^- - S_{i_k}^-) c_{i_k,\uparrow}^\dagger c_{j_k,\uparrow}^\dagger |0\rangle = c_{i_k,\uparrow}^\dagger c_{j_k,\downarrow}^\dagger - c_{i_k,\downarrow}^\dagger c_{j_k,\uparrow}^\dagger |0\rangle$. Thus it is proved that two wave functions $|\text{RVB}\rangle$ and $|p\text{-BCS}\rangle$ are exactly the same. In the remaining of this Appendix, we will show that even for the triangular lattice geometry, the so-called short range RVB wave function $|\psi_{\text{RVB}}\rangle$ [Eq. (51)] can be described by the projected BCS wave function (D4) with a particular choice of the matrix $\bar{f}$.

1. Consequences of the theorem: short range RVB wave function

The short range RVB wave function $|\psi_{\text{RVB}}\rangle$ [Eq. (51)] is defined with the same weight for all nearest neighbor valence bonds. Therefore, if we can find the matrix $\bar{f}$ in Eq. (D2) in such a way that the sign of the permutation for each dimer covering is exactly canceled, i.e.,

$$(-1)^p \prod_{k=1}^{N} f_{i_k j_k} = 1, \quad (D7)$$

then a relation is established between RVB wave functions and projected BCS wave functions. The condition (D7) is highly nontrivial and difficult to satisfy as the number of dimer coverings is exponentially large and the entries of the matrix are few in comparison. Nevertheless, this problem for the case of nearest neighbor dimer covering was solved in all planar graphs.[79]

By applying these old results,[79] we can generalize the Read-Chakraborty relation between the short range RVB and projected BCS wave functions on the square lattice[80] for the triangular lattice case. Namely, by using the known matrix $\bar{f}$ reported in Ref. 79, it is possible to satisfy the condition (D7) even for the triangular case.[7] Here we use open boundary conditions for a lattice of $l \times l$ sites (l being multiple of 6) where site i is ordered lexicographically: $i = lm_2 + m_1 + 1 = (m_1, m_2)$. The Cartesian coordinates of the triangular lattice (Fig. 1) are thus

$$\vec{r}_i = m_1 \vec{\tau}_1 + m_2 \vec{\tau}_2 = (m_1 + m_2/2, \sqrt{3}m_2/2).$$

The pairing functions $f_{k,j}$ which meet the condition (D7) reads

$$f_{k,j} = \begin{cases} 1 & \text{for } j = (1,0), \\ 1 & \text{for } j = (0,1), \\ 1 & \text{for } j = (-1,1) \end{cases} \quad (D8)$$

for $k = (0,0)$, whereas

$$f_{k,j} = \begin{cases} 1 & \text{for } j = (2,0), \\ -1 & \text{for } j = (1,1), \\ -1 & \text{for } j = (0,1) \end{cases} \quad (D9)$$

for $k = (1,0)$. All the other values of $f_{k,j}$ are obtained by translation of $2\vec{\tau}_1 = (2,0)$ and/or $\vec{\tau}_2 = (1,0)$. Therefore, the unit cell of $f_{k,j}$ is (2×1) on the triangular lattice (see Fig. 11).

2. Complex representation (Ref. 7)

We can multiply by the imaginary unit i all the $c_{j,\sigma}^\dagger$ for the odd $\vec{\tau}_1$ components of j since the resulting wave function is equivalent to the original one [Eq. (D4)] in the presence of the projection operator $\mathcal{P}_G$ (apart from an overall phase). The obtained new complex matrix $\bar{f}$ consists of

$$f_{k,j} = \begin{cases} i & \text{for } j = (1,0), \\ 1 & \text{for } j = (0,1), \\ i & \text{for } j = (-1,1), \text{ the diagonal bond} \end{cases}$$

for $k = (0,0)$, whereas

$$f_{k,j} = \begin{cases} i & \text{for } j = (2,0), \\ 1 & \text{for } j = (1,1), \\ -i & \text{for } j = (0,1), \text{ the other diagonal bond} \end{cases}$$

for $k = (1,0)$. All the other values of $f_{k,j}$ are obtained by translation of $2\vec{\tau}_1 = (2,0)$ and/or $\vec{\tau}_2 = (1,0)$. Notice that if the diagonal bonds are eliminated, we end up with again a (1×1) unit cell with $f_{\mathbf{k}} \propto \cos(k_x) - i \cos(k_y)$ in Fourier space, thus recovering the Read-Chakraborty result for the square lattice with $\vec{r}_i = (m_1, m_2)$.[80]

It is important to emphasize that for the triangular lattice geometry a (2×1) unit cell is inevitable even with the complex representation (as the diagonal bonds acquire different signs). Thus, we conclude that the translation symmetry in $f_{k,j}$ has to be broken for a good projected BCS wave function in the triangular case. It is interesting that two sites per a unit cell is enough, in contrast to the classical Néel order state with 120° of mutual spin orientations which contains instead three sites per unit cell.

3. Periodic boundary conditions

For the short range RVB state with periodic boundary

conditions, it is known that condition (D7) cannot be satisfied by a single $|p\text{-BCS}\rangle$, but by four, all obtained with the possible choices of periodic and antiperiodic boundary conditions in $\vec{\tau}_1$ and $\vec{\tau}_2$ directions.[79] The proof can be applied for

each of such $|p\text{-BCS}\rangle$, showing that these four projected BCS wave functions have to be used to exactly match the short range RVB wave function with periodic boundary conditions.

---

[1] P. W. Anderson, Mater. Res. Bull. **8**, 153 (1973); P. Fazekas and P. W. Anderson, Philos. Mag. **30**, 423 (1973).

[2] B. Bernu, C. Lhuillier, and L. Pierre, Phys. Rev. Lett. **69**, 2590 (1992); B. Bernu, P. Lecheminant, C. Lhuillier, and L. Pierre, Phys. Rev. B **50**, 10048 (1994).

[3] P. Sindzingre, P. Lecheminant, and C. Lhuillier Phys. Rev. B **50**, 3108 (1994).

[4] L. Capriotti, A. E. Trumper, and S. Sorella, Phys. Rev. Lett. **82**, 3899 (1999).

[5] Zheng Weihong, R. H. McKenzie, and R. P. Singh, Phys. Rev. B **59**, 14 367 (1999).

[6] S. Chakravarty, B. I. Halperin, and D. R. Nelson, Phys. Rev. B **39**, 2344 (1989).

[7] P. Fendley, R. Moessner, and S. L. Sondhi, Phys. Rev. B **66**, 214513 (2002).

[8] D. S. Rokhsar and S. A. Kivelson, Phys. Rev. Lett. **61**, 2376 (1988).

[9] E. Fradkin, D. A. Huse, R. Moessner, V. Oganesyan, and S. L. Sondhi, Phys. Rev. B **69**, 224415 (2004).

[10] M. Capone, L. Capriotti, F. Becca, and S. Caprara, Phys. Rev. B **63**, 085104 (2001).

[11] R. Coldea, D. A. Tennant, A. M. Tsvelik, and Z. Tylczynski, Phys. Rev. Lett. **86**, 1335 (2001); R. Coldea, D. A. Tennant, K. Habicht, P. Smeibidl, C. Wolters, and Z. Tylczynski, *ibid.* **88**, 137203 (2002); R. Coldea, D. A. Tennant, and Z. Tylczynski, Phys. Rev. B **68**, 134424 (2003).

[12] Y. Shimizu, K. Miyagawa, K. Kanoda, M. Maesato, and G. Saito, Phys. Rev. Lett. **91**, 107001 (2003).

[13] All results presented here in this paper are calculated with periodic boundary conditions (PBC) unless otherwise stated.

[14] L. D. Faddeev and L. A. Takhtajan, Phys. Lett. **85A**, 375 (1981).

[15] D. A. Tennant, T. G. Perring, R. A. Cowley, and S. E. Nagler, Phys. Rev. Lett. **70**, 4003 (1993); D. C. Dender, D. Davidovic, D. H. Reich, C. Broholm, K. Lefmann, and G. Aeppli, Phys. Rev. B **53**, 2583 (1996).

[16] D. M. Ceperley and B. J. Alder, Phys. Rev. Lett. **45**, 566 (1980); Science **231**, 555 (1986).

[17] S. Yunoki and S. Sorella, Phys. Rev. Lett. **92**, 157003 (2004).

[18] S. Sorella, G. B. Martins, F. Becca, C. Gazza, L. Capriotti, A. Parola, and E. Dagotto, Phys. Rev. Lett. **88**, 117002 (2002).

[19] M. Vojta and E. Dagotto, Phys. Rev. B **59**, R713 (1999).

[20] Q.-H. Wang, D.-H. Lee, and P. A. Lee, Phys. Rev. B **69**, 092504 (2004).

[21] L. Arrachea (private communication).

[22] M. Casula and S. Sorella, J. Chem. Phys. **119**, 6500 (2003).

[23] See, e.g., W. H. Press, S. A. Teukolsky, W. T. Vetterling, and B. P. Flannery, *Numerical Recipes* (Cambridge University Press, New York, 2002).

[24] C. J. Umrigar and C. Filippi, Phys. Rev. Lett. **94**, 150201 (2001).

[25] S. Sorella, Phys. Rev. B **71**, 241103(R) (2005).

[26] M. Casula, C. Attaccalite, and S. Sorella, J. Chem. Phys. **121**,

7110 (2004).

[27] J. D. Reger and A. P. Young, Phys. Rev. B **37**, R5978 (1988).

[28] A. W. Sandvik, S. Daul, R. R. P. Singh, and D. J. Scalapino, Phys. Rev. Lett. **89**, 247201 (2002).

[29] K. Harada, N. Kawashima, and M. Troyer, Phys. Rev. Lett. **90**, 117203 (2003).

[30] S. Liang, B. Doucot, and P. W. Anderson, Phys. Rev. Lett. **61**, 365 (1988).

[31] sgn[f] denotes the sign of f, i.e., $f/|f|$.

[32] G. Santoro, S. Sorella, L. Guidoni, A. Parola, and E. Tosatti, Phys. Rev. Lett. **83**, 3065 (1999).

[33] M. CalandraBuonaura and S. Sorella, Phys. Rev. B **57**, 11446 (1998).

[34] This condition can be checked for small size systems.

[35] H. J. M. vanBemmel, D. F. B. tenHaaf, W. van Saarloos, J. M. J. vanLeeuwen, and G. An, Phys. Rev. Lett. **72**, 2442 (1994): D. F. B. ten Haaf, J. M. J. van Leeuwen, W. van Saarloos, and D. M. Ceperley, Phys. Rev. B **51**, 13039 (1995).

[36] S. Sorella and S. Yunoki, in *The Monte Carlo Method in the Physical Sciences*, AIP Conf. Proc. No. 690, edited by J. Gubernatis (AIP, Melville, NY, 2003), p. 318.

[37] P. J. Reynolds, D. M. Ceperley, B. J. Alder, and W. A. Lester, J. Chem. Phys. **77**, 5593 (1982).

[38] E. H. Lieb, T. D. Schultz, and D. C. Mattis, Ann. Phys. (N.Y.) **16**, 407 (1961); I. Affleck and E. H. Lieb, Lett. Math. Phys. **12**, 57 (1986).

[39] S. Sorella, cond-mat/0201388 (unpublished).

[40] See, e.g., H. G. Evertz, Adv. Phys. **52**, 1 (2003); N. Kawashima and K. Harada, J. Phys. Soc. Jpn. **73**, 1379 (2004).

[41] S. Sorella and L. Capriotti, Phys. Rev. B **61**, 2599 (2000).

[42] See, e.g., B. Efron and R. J. Tibshirani, *An Introduction to the Bootstrap* (Chapman & Hall/CRC, Boca Raton, 1994).

[43] A. Parola, S. Sorella, F. Becca, and L. Capriotti, cond-mat/0502160 (unpublished).

[44] W. Marshall, Proc. R. Soc. London, Ser. A **232**, 48 (1955).

[45] C. Gros, Ann. Phys. (N.Y.) **189**, 53 (1989).

[46] See, e.g., J. R. Schrieffer, *Theory of Superconductivity* (Addison Wesley, New York, 1988).

[47] See, e.g., V. E. Korepin, in *Exactly Solvable Models of Strongly Correlated Electrons*, edited by V. E. Korepin and H. L. Essler (World Scientific, Singapore, 1994).

[48] X. G. Wen, Phys. Rev. B **65**, 165113 (2002).

[49] X. G. Wen, *Quantum Field Theory of Many-body Systems: From the Origin of Sound to an Origin of Light and Electrons* (Oxford University Press, Oxford, 2004).

[50] In Figs. 5 and 6, the variational parameters optimized for $L=18 \times 18$ (Table I) are used.

[51] S. R. White and I. Affleck, Phys. Rev. B **54**, 9862 (1996).

[52] S. Sorella, L. Capriotti, F. Becca, and A. Parola, Phys. Rev. Lett. **91**, 257005 (2003).

[53] L. Capriotti, F. Becca, A. Parola, and S. Sorella, Phys. Rev. B **67**,

212402 (2003).

[54] X. G. Wen and A. Zee, Phys. Rev. B **66**, 235110 (2002).

[55] Assuming that $|\Psi_{\text{RVB}}\rangle$ and $|\Psi_0\rangle$ here are properly normalized.

[56] P. W. Kasteleyn, J. Math. Phys. **4**, 287 (1963).

[57] T. Li (private communication).

[58] When $\xi_{\mathbf{k}}=0$, the off-diagonal pairing terms in Eq. (C3) are completely eliminated by the following unitary transformation:

$$\begin{pmatrix} c_{\vec{k}\uparrow} \\ c^{\dagger}_{-\vec{k}\downarrow} \end{pmatrix} \rightarrow \hat{\mathcal{U}}_y(\pi/2) \begin{pmatrix} c_{\vec{k}\uparrow} \\ c^{\dagger}_{-\vec{k}\downarrow} \end{pmatrix}.$$

Here $\hat{\mathcal{U}}_y(\alpha)=\exp(-i\alpha\sigma_y/2)$ and σ_y is the y component of the Pauli matrices.

[59] Also finite μ or $t_{i,j}$ in $|p\text{-BCS}\rangle$ generates long range singlet valence bonds in general.

[60] C. Weber, A. Laeuchil, F. Mila, and T. Giamarchi, Phys. Rev. B **73**, 014519 (2006).

[61] D. M. Ceperley and M. H. Kalos, in *Monte Carlo Methods in Statistical Physics*, 2nd ed., edited by K. Binder (Springer-Verlag, Berlin, 1986), p. 145.

[62] This property has been verified by numerically computing both diagonal and off diagonal spin-spin correlation functions. Namely, the mixed average estimate of the magnetic order parameter in the xy-plane was computed and found to remain negligibly small.

[63] FNE provides results similar to GFMCSR (Ref. 4), when the same guiding function is used. However, FNE is much more efficient, as far as the statistical errors are concerned, and provides a variational upper bound of the energy.

[64] Here we have not attempted to compare the spin liquid ansatz $|p\text{-BCS}\rangle$ with the exact ground state of the 6×6 lattice. However, we have found that the energy variance [Eq. (47)] calculated for $|p\text{-BCS}\rangle$ remains approximately independent of J'/J, suggesting that the quality of this spin liquid wave function does not degrade even away from the isotropic point.

[65] To estimate the lowest excitation gap in $E_{\mathbf{k}}$ in the thermodynamic limit, the variational parameters optimized for $L=18\times18$ (Table III) are used for larger systems.

[66] The way to open a finite spin excitation gap discussed here is similar to the one realized in the quantum dimer model on the triangular lattice (Ref. 7), where in order to treat the dimer covering of the lattice, an algebraic method based on the Pfaffian was introduced. The corresponding matrix is also defined in a (2×1) unit cell (see also Appendix D).

[67] The variational parameters are optimized for clusters up to $L=18\times18$, and the ones for $L=18\times18$ are used for the 30×30 cluster calculations.

[68] L. Arrachea, L. Capriotti, and S. Sorella, Phys. Rev. B **69**, 224414 (2004).

[69] M. Bocquet, F. H. L. Essler, A. M. Tsvelik, and A. O. Gogolin, Phys. Rev. B **64**, 094425 (2001).

[70] B. J. Powell and R. H. McKenzie, Phys. Rev. Lett. **94**, 047004 (2005).

[71] J. Liu, J. Schmalian, and N. Trivedi, Phys. Rev. Lett. **94**, 127003 (2005).

[72] Note, however, that the value of J'/J for this compound might not be determined accurately by the lowest order strong coupling expression of the corresponding Hubbard model. For more details, see, for example, O. I. Motrunich, Phys. Rev. B **72**, 045105 (2005).

[73] Y. Kurosaki, Y. Shimizu, K. Miyagawa, K. Kanoda, and G. Saito, Phys. Rev. Lett. **95**, 177001 (2005).

[74] F. Kagawa, K. Miyagawa, and K. Kanoda, Nature (London) **436**, 534 (2005).

[75] T. Hanaguri, C. Lupien, Y. Kohsaka, D. H. Lee, M. Azuma, M. Takano, H. Takagi, and J. C. Davis, Nature (London) **430**, 1001 (2004).

[76] T. Senthil, A. Vishwanath, L. Balents, S. Sachdev, and M. P. A. Fisher, Science **303**, 1490 (2004).

[77] H. Yokoyama and H. Shiba, J. Phys. Soc. Jpn. **57**, 2482 (1988).

[78] S. Liang, B. Doucot, and P. W. Anderson, Phys. Rev. Lett. **61**, 365 (1988).

[79] P. W. Kasteleyn, J. Math. Phys. **4**, 287 (1963).

[80] N. Read and B. Chakraborty, Phys. Rev. B **40**, 7133 (1989).